A Computational Study of Bubble Suspensions and Foamed Cement using Extended Stokesian Dynamics

Submitted in partial fulfillment of the requirements for
the degree of
Doctor of Philosophy
in
Computational Mechanics

Eilis Jill Rosenbaum

B.S., Chemical Engineering, Geneva College
B.S., Mechanical Engineering, Geneva College
M.S., Chemical and Petroleum Engineering, University of Pittsburgh

Carnegie Mellon University
Pittsburgh, PA

August, 2019

Acknowledgements

I first want to thank Anthony Cugini, who encouraged me to pursue my PhD. I found out about his passing right after my qualifying exam and it still brings tears to my eyes because I wish I could thank him face-to-face. Anthony was a wonderful and caring professor and you could see his love and passion for teaching in the way he taught his course.

I want to thank my wonderful advisors, Kaushik Dayal and Mehrdad Massoudi, for their support, teaching, and advice in conducting my research. Without their extensive knowledge and expertise, this would not have been possible. I also want to extend my thanks and gratitude to Barbara Kutchko and Glen Benge, who provided me with so much support, advice, and practical input. I want to thank David Dzombak for helping me to construct my proposal document and focus my research goals. I really appreciate his attention to detail. I could not have completed my research without the support of my committee members. And I am very grateful to have such an incredible support team.

I want to thank my supportive supervisors, Paul Turner and Dirk Link. They allowed me the time to both work and conduct my research to complete my degree. Paul Turner paved the way for me to start my degree and was so supportive in this pursuit. Dirk Link's efficiency as a supervisor provided me the time to be able to focus on completing my degree. I also want to thank the Department of Energy Academic Degree Program that provided funding for a portion of my degree.

I would not have been able to even start my degree or keep up with all the requirements and processes had it not been for Maxine Leffard. She not only is extremely knowledgeable about every process but she is so kind and supportive when she is helping you. Her shoes are really big to fill but David Vey has somehow managed to fill her shoes. Maxine takes care of all her Carnegie Mellon University (CMU) children and I know how fortunate I am to have had her help and support.

Both at the National Energy Technology Laboratory and at CMU, I have been fortunate to have worked with incredible research groups and I thank them for their patience as I worked on my degree.

I have also had wonderful mentees, who contributed programming skills that enhanced the data analysis and data inputs. Adrian Salguero aided in creating data inputs more efficiently and analyzed field data to confirm the data fit a lognormal distribution. I owe a great debt of gratitude to Brandon Mathis who designed a new segmentation method to properly characterize the bubble properties in the foamed cement. He also designed and wrote a highly comprehensive code to

perform the neighbor analysis.

I want to thank the National Science Foundation for support through the Extreme Science and Engineering Discovery Environment (XSEDE) resources. This work used the XSEDE Bridges Computing Resources provided at the Pittsburgh Supercomputing Center through TG-DMR160018.

I am grateful for being awarded the Bradford and Diane Smith Graduate Fellowship, which was created through the generosity of Bradford Smith, a 1969 graduate of the CMU College of Engineering, and his wife Diane, a 1971 CMU graduate of the Dietrich College of Humanities and Social Sciences to help support the graduate studies of highly deserving students in the College of Engineering at CMU.

I want to thank my countless friends and family members who encouraged me and were patient when I had to focus on my degree and miss events. I am grateful for all the people who helped me throughout this process.

Abstract

Foamed cement is created by injecting gas into a cement slurry to create a dispersion of bubbles in the cement. The cement is foamed to reduce the density of the cement slurry when a lightweight cement is needed. The gas bubbles influence the rheological properties of the cement base slurry. The goal of this work was to determine the influence of the bubble size and spatial arrangement on the potential for bubble clustering or structuring in a foamed cement slurry, as this could lead to connected bubbles once the foamed cement fully hydrates, or which could result in crack formation along a line of bubbles. Either condition would affect the cement's ability to properly isolate the well. A bubble interaction to simulate bubbles in a Newtonian fluid was developed in this research. The bubble interaction accounts for the nature of the bubbles by allowing for slip on the bubble surface, the deflection on the bubble surface, a bubble-bubble pairwise interaction that represents the surfactant properties, and was developed for polydisperse bubble sizes. The size distributions of bubbles determined from a real foamed cement sample were used as simulation inputs. It was possible to simulate a realistic bubble size distribution using the bubble interaction. This method can be used to simulate relevant volume fractions of bubbles that represent real foams. The LAMMPS simulation code is available publicly at `lammps.sandia.gov`. Our implementation within the LAMMPS framework of the interactions described in this paper are publicly available at `github.com/eilisjill/Pair_style_bubble`.

Keywords: Stokesian Dynamics, Fast Lubrication Dynamics, dense suspension, foamed cement, polydispersity, rheology

Contents

List of Tables

List of Figures

Notation

ρ	density
t	time
$_f$	subscript refers to fluid component
$_s$	subscript refers to solid component
$\boldsymbol{v}$	velocity
μ	viscosity
ϕ	volume fraction
$\boldsymbol{m}^i$	interaction forces
σ^i	partial stress tensor
m	mass
r	radial distance between particles/bubbles
h	separation between particle/bubble surfaces
$\boldsymbol{U}$	generalized velocity vector
$\boldsymbol{m}$	generalized moment of inertia matrix
$\boldsymbol{F}$	generalized force vector
$\boldsymbol{E}^\infty$	symmetric rate-of-strain tensor
$\boldsymbol{U}^\infty$	generalized far-field velocity
$\boldsymbol{S}^H$	Stresslet

$\mathcal{R}$	resistance matrix
$\mathcal{M}$	mobility matrix
$\mathcal{M}^{\infty}$	grand mobility matrix
$\mathcal{R}_{Iso}$	isotropic resistance tensor
$\mathcal{R}_{FLD}$	FLD resistance matrix
$\boldsymbol{f}_i$	lubrication force
$\boldsymbol{g}_i$	lubrication torque
$\boldsymbol{n}$	unit vector
$\boldsymbol{\omega}$	angular velocity
$_{sq}$	subscript refers to squeezing
$_{sh}$	subscript refers to shearing
$_{pu}$	subscript refers to pumping shear
$\boldsymbol{\sigma}_i$	symmetric stress tensor of particle/bubble i
V	volume
I	integral
γ_{Euler}	Euler's constant, 0.577216
δ	deflection of bubble surface
ϕ_{LJ}	Lennard-Jones (LJ) potential
ϵ	Lennard-Jones energy scale
σ	Lennard-Jones length scale
$\dot{\gamma}$	simulation box strain rate
Δt	simulation time step
α	relationship between bubble radii $\frac{ab}{a+b}$

Chapter 1

Introduction

In drilling and completing a well, cement is placed in the annulus between the well casing and the formation to prevent fluid migration and to support the casing. A successful cement job will provide complete "zonal isolation" (Dusterhoft, 2003; Economides, 1990; Nelson, 1990). The premise of this project is to examine the rheological properties of cements that have been foamed with an inert gas to form stable slurries with bubbles dispersed throughout. These lower density cements provide the unique properties needed for specific wellbore environments (Benge et al., 1996; Bour and Rickard, 2000; Frisch et al., 1999; O'Rourke and Crombie, 1999; White et al., 2000). The conditions under which foamed cements are produced and pumped into the well make them difficult to study experimentally, especially when establishing the effects of flow on the physical properties of the set cement. During flow, the bubbles will re-arrange and can cluster or structure relative to the direction of flow. An increased propensity of the bubbles to structure could cause channels to form, allowing fluid migration, or crack initiation in the cured cement sheath that provides support to the well casing. The bubbles found in foamed cements remain relatively stable and maintain a relatively spherical shape so the bubbles can be thought of as spherical particles in the cement fluid. The conditions (i.e. average bubble size, volume fraction of bubbles, distribution of bubble sizes, etc.) that tend to form structures were explored as well as the viscoelastic properties of different

bubble configurations.

We want to be able to correlate the properties of the foamed cements that are typically tested in the laboratory according to recommended American Petroleum Institute (API) standards API10B-42004 to the foamed cements typically used in the field. Laboratory tests designed to determine the foamed cement slurry stability and other physical benchmarks are done at bench scale and produced by foaming in a blender (API 10B-4, 2004) under atmospheric conditions. In field applications, the cement is typically foamed by high-pressure nitrogen gas injection through an atomizer at much higher shearing rates. The bubbles produced by these two processes are quite different in terms of size, the size distribution, and bubble configurations. Blender made cements produce bubbles that are significantly larger in size [when compared to field cements] and increase in size with foam quality (cementing industry term for volume fraction of bubbles added to the cement) (Kutchko et al., 2013). While field cements have similar sized bubbles across all qualities, they contain more bubbles as quality increases (Kutchko et al., 2015) and this is due to their two different production methods. The field cements are also subjected to changing pressures as they are being placed, so the quality is also changing.

The primary purpose of well cement is to provide zonal isolation and secondary to support the casing. Foamed cement permeability is affected by the amount of gas dispersed in the cement and the configuration of the bubbles. The U.S. Department of Energy Technology Laboratory (NETL) has produced laboratory samples that represent the typical blender samples produced according to recommended API practices as well as samples collected from several industry partners representing the foamed cement before it is pumped into the well. In order to maintain expected permeability and sealing capability during placement, the bubbles in the slurry should remain dispersed and not coalescence. Through different modeling scenarios, we can predict whether the bubbles in the foamed slurry are expected to cluster or structure, which is an indication of the foamed cements ability to provide zonal isolation. Bubble clustering could lead to bubble coalescence and bubble structuring could lead to channeling and cracking of the hydrated cement. Bubble sizes and posi-

tions from experimentally produced foamed cement samples will be used as initial conditions for simulations and simulation results will be compared with experimental samples that were collected directly in the flow circuit.

1.1 Cement

The book Well Cementing (Nelson et al., 1990; Nelson, 1990), particularly Chapter 2: Chemistry and Characterization of Portland Cement (Michaux et al., 1990; Nelson et al., 1990), was the primary reference consulted to write this summary. Cement is used in a plethora of industries and in construction worldwide and one would be hard pressed to go anywhere in the world and not find cement. We typically see cement used in building structures, which has added aggregates that are bound together by the cement and is referred to as concrete. The oil and gas industry uses cement to complete the well and prevent fluids from migrating as well as providing stability for the well casing. The cement used in the oil and gas industry for well completions is generally Portland cement. Well cement is a complex system of cement and additives that are included to attain certain properties of the cement and are designed specifically for the environment of the well.

Cement is created by the chemical reactions between the cement clinker and water. Hardening occurs upon hydration of the cement. Cement clinker is the powdery mix that we would call the cement. The clinker is a mix of materials that is dependent on the location of extraction but is primarily made of up lime, silica, alumina, and iron. Gypsum is also added to control the hydration reaction. The materials are heated in a kiln and pulverized to the required particle size and 3% to 5% gypsum is added.

The complicated chemical equations involved in cement hydration are simplified in their presentation by using shorthand notation to represent typical components found in cement. The oxides are all shortened to the first letter of the compound/s. The typical material composition used to manufacture the cement clinker is shown in Table 1.1.

Table 1.1: Major Material Compounds Used to Manufacture Cement Clinker

Compound	**Formula**	**Shorthand Notation**
Calcium oxide - 'lime'	CaO	C
Silicon dioxide - 'silica'	SiO_2	S
Aluminum oxide - 'alumina'	Al_2O_3	A
Iron oxide	Fe_2O_3	F
Gypsum	$CaSO_6 \cdot 2\,H_2O$	$C\underline{S}H_2$

Table 1.2: Chemical Composition of the Typical Cement Clinker

Compound	**Formula**	**Shorthand Notation**
Dicalcium Silicate or **Belite**	Ca_2CiO_4	C_2S
Tricalcium Silicate or **Alite**	Ca_3SiO_5	C_3S
Tricalcium **Aluminate**	$Ca_3Al_2O_6$	C_3A
Tetracalcium Alumino**ferrite**	$Ca_4Al_2Fe_2O_{10}$	C_4AF
Gypsum	$CaSO_6 \cdot 2\,H_2O$	$C\underline{S}H_2$

The major compounds found in the final clinker composition are listed in Table 1.1. The gypsum, as mentioned previously, is added to control the chemical reactions of the cement hydration to attain the proper properties to allow workability and placement.

Silicates make up the majority of the cement, with alite having the highest concentration. Alite and Belite are not pure compositions of calcium oxide and silicate like tricalcium silicate and dicalcium silicate, respectively. C_3S plays a dominant role in the hydration process. It hydrates quickly when it reacts with water and develops early strength in the cement. C_2S undergoes a hydration process similar to that of C_3S but hydrates and hardens slowly and contributes to the strength over a longer time frame. The aluminate and ferrite will react quickly with water and can cause the cement to set prematurely in what is called a flash set if the reaction is not controlled. To mitigate this issue, a suitable amount of gypsum is added to the clinker. Aluminate and ferrite do not contribute much to the cement strength but the ferrite serves as a fluxing agent and gives cement its color. The hydration process of cement is highly complex and has parallel reactions occurring with the silicate and the aluminate phases, though the reactions occur at different rates. The silicates reactions have been shown to have five nearly distinct phases in the hydration process: Preinduction, Induction,

Acceleration, Decelaration, and Diffusion. These phases generally are used to depict the overall hydration process of cement. Preinduction of the silicate hydration occurs almost immediately when the C_3S comes into contact with water and starts the pattern of dissolution and precipitation. During this phase, calcium silicate hydrate (C−S−H) is formed and supersaturates the solution. C−S−H gel then precipitates and deposits a thin layer on the surface of the C_3S. Soon after the preinduction phase, the silicate hydration reaction slows. The aluminates are highly reactive and would cause the cement to set quickly if the reactions were not controlled with the addition of gypsum. Because of their reactivity they can contribute to the strength of the cement early in the hydration process. Without gypsum, in a similar reaction to the protonation of the C_3S surface with water, hydroxylation of the C_3A surface leads to dissolution of the surface. Calcium aluminate hydrates will supersaturate the solution and then precipitate out. The calcium aluminate hydrates will eventually form a more stable form, C_3AH_6.

Aluminate Reactions in the Absence of Gypsum:

Tricalcium aluminate + water $\longrightarrow$ *calcium aluminate hydrates*

$$2\,\mathrm{C_3A} + 27\,\mathrm{H} \longrightarrow \mathrm{C_2AH_8} + \mathrm{C_4AH_{19}} \tag{1.1.0.1}$$

Calcium aluminate hydrates $\longrightarrow$ *cubic calcuium aluminate hydrate*

$$\mathrm{C_2AH_8} + \mathrm{C_4AH_{19}} \longrightarrow 2\,\mathrm{C_3AH_6} + 15\,\mathrm{H} \tag{1.1.0.2}$$

Initial Reactions of Portland Cement:

Tricalcium aluminate + gypsum + water -> ettringite

$$\mathrm{C_3} + 3\,\mathrm{C\underline{S}H_2} + 26\,\mathrm{H} \longrightarrow \mathrm{C_6A\underline{S}_3H_{32}} \tag{1.1.0.3}$$

Tricalcium silicate + water $\longrightarrow$ *calcium silicate hydrate + lime*

$$2\,C_3S + 6\,H \longrightarrow C_3S_2H_3 + 3\,CH \tag{1.1.0.4}$$

Ferrite + gypsum + water $\longrightarrow$ *ettringite + ferric aluminum hydroxide + lime*

$$C_4AF + 3\,C\underline{S}H_2 + 3\,H \longrightarrow C_6(A,F)\underline{S}_3H_{32} + (A,F)H_3 + CH \tag{1.1.0.5}$$

During induction, there is little hydration occurring. The C–S–H gel continues to slowly precipitate and Ca_2^+ and OH^- concentrations continue to rise in the solution. The mechanisms that control induction and the eventual re-initiation of hydration are not well understood and only theories have been suggested. Induction is like a pause in the hydration reaction and is generally thought to be caused by the C–S–H gel layer on the silicate grains, which eventually increases in permeability to continue the hydration process. The aluminates do not have an induction period, but the gypsum added to the cement clinker does slow the reactions of the aluminate phases to have a pseudo-induction. The dissolution of gypsum in water releases calcium and sulfate ions, which react with the aluminate and hydroxyl ions in the solution from the C_3A. Calcium trisulfoaluminate hydrate is formed which precipitates onto the surface of the C_3A and hinders further rapid hydration and creates a pseudo-induction period. Calcium trisulfoaluminate hydrate is better known as ettringite. As the gypsum is reacted, ettringite continues to precipitate until no more gypsum is available. At this point, the reaction of rapid C_3A hydration continues. After the permeability of the C–S–H gel increases and the hydration reaction progresses, a period of acceleration of the hydration reactions occurs. The calcium hydroxide crystalizes from the solution during this phase and the structure of the cement begins to emerge as the hydrates grow and interweave. Eventually the porosity decreases due to the growing hydrates. The available ionic species and water are restricted from migrating freely through the network of hydrating species so the reactions decelerate. Total hydration of the silicates is never attained but rather slows significantly due to the decreasing porosity in the system. Eventually the ettringite becomes unstable and converts to a platy calcium monosulfoaluminate hydrate from the tricalcium aluminate or hydrogarnets when ettringite reacts with ferrite.

Tricalcium aluminate + ettringite + water $\longrightarrow$ *calcium monosulfoaluminate hydrate*

$$2\,\mathrm{C_3A} + \mathrm{C_6A\underline{S}_3H_{32}} + 4\,\mathrm{H} \longrightarrow 3\,\mathrm{C_4A\underline{S}H_{12}} \tag{1.1.0.6}$$

Ferrite + ettringite + lime + water -> garnets

$$\mathrm{C_4AF} + \mathrm{C_6(A,F)\underline{S}_3H_{32}} + 2\,\mathrm{CH} + 23\,\mathrm{H} \longrightarrow 3\,\mathrm{C_4(A,F)\underline{S}H_{18}} + \mathrm{(A,F)H_3} \tag{1.1.0.7}$$

Cement placement is done during the induction phase when little hydration is occurring and the cement is workable and will flow. For well cementing, the setting time of the cement can be altered by using additives, which can cause early setting or retard the hydration process further.

1.2 Foams

Foams are systems of gas dispersed in a liquid medium (Bikerman, 1965; Pugh, 1996). The manner in which the foam is created influences the bubble sizes and dispersion. Foams can be formed by condensation (e.g. carbonated beverages), or by dispersion (Bikerman, 1965). Dispersion of the bubbles into the liquid phase can be accomplished by agitating the liquid in some manner to cause foaming, such as using a blender (improved with foaming and/or stabilizing agents). Gas can also be dispersed through an orifice. The later method allows more control over the foaming properties (e.g. adjusting orifice size, gas injection rate, etc.). After initial dispersion where the bubble sizes are fairly spherical, foam can separate into regions with liquid on the bottom, caused by fluid drainage through the bubbles, and non-spherical bubbles on top with bubble size and deformity increasing as the bubbles rise. As the foam ages the bubbles redistribute, the film between the bubbles thin, and eventually may rupture (Bikerman, 1965; Langevin, 2000; Pugh, 1996, 2005). These detrimental processes to the foam properties can be combated with the use of specialized stabilizers and surfactants. Unlike foamed aqueous solutions, where the bubbles tend to rise due to buoyancy, bubbles in cement tend to remain in place unless they reach a critical size. In laboratory

and field applications, the bubble sizes all remain below this critical size. Cement is a yield stress fluid, which means that for the cement to flow around any bubble, the yield stress must be overcome. This helps to keep the bubbles in place relative to each other. Another property of cement that helps with its stability are the cement slurry particles, which act as surface active foaming materials (Pugh, 1996).

1.3 Foamed Cement

In drilling and completing a well, cement is placed in the annulus between the well casing and the formation to prevent fluid migration and to support the casing. A successful cement job will provide complete zonal isolation (Dusterhoft, 2003; Economides, 1990; Nelson, 1990). The cement density is designed to keep the cement gradient between the fracture and pore pressures (Frisch et al., 1999; Rae, 1990) and current technologies allow the foamed cement density or quality (gas volume fraction) to be controlled and optimized during operations (American Petroleum Institute, 2010). Foamed cements offer an economically viable low-density option that still maintains compressive strength. Foaming the cement also offers other improved properties compared to conventional cement or alternative light-weight cement (Benge et al., 1996; Bour and Rickard, 2000; Frisch et al., 1999; O'Rourke and Crombie, 1999; White et al., 2000).

Foamed cement is typically used in wells with weak formations or anywhere a low density cement is required but it has been used successfully in other adverse environments where the foaming provides better performance, over conventional or unfoamed cements (Loeffler, 1984). It has been used for high-temperature/high-pressure wells where stress cracking is of concern due to the cycling pressures and temperatures (Benge et al., 1996; Griffith et al., 2004). Its higher ductility when compared to conventional cements makes it more resilient to stress cracking (Benge et al., 1996; Bour and Rickard, 2000; Frisch et al., 1999; White et al., 2000). With its ability to withstand cyclical conditions, foamed cement is well suited for geothermal wells (Bour and Rickard,

2000). Foamed cement reduces lost circulation (Bour and Rickard, 2000; Dusterhoft, 2003), where some of the cement flows into the formation, since foamed cement can be maintained below the formation fracture gradient during placement. Foamed cement offers improved mud displacement and controls gas migration better than conventional cements (Bour and Rickard, 2000; Frisch et al., 1999; White et al., 2000) due to the presence of the bubbles in the cement slurry. Even with the specialized foaming equipment, overall costs can be reduced by using foamed cement and, due in part to using less material, foamed cement has a lower environmental impact (Bour and Rickard, 2000).

Foamed cement is designed for the downhole conditions where it is to be placed in the well (Loeffler, 1984). In cementing jobs where methods other than foaming are used to control the cement density, the casing might be done in stages with different cement slurries to match the well conditions (Burdylo and Birch, 1990). Foaming the cement allows the quality to be controlled during the placement process and allows changes to the quality. Cement is generally foamed with nitrogen, as it should not alter the cement chemistry (American Petroleum Institute, 2010). Models and specialized software are used to design the optimal base slurry with consideration to stabilizers, surfactants, other additives, final density, cementing time, local geology, etc. Models are also used in the design of foamed cement and will determine the proper density of the foamed cement and/or the nitrogen injection rate for placement (American Petroleum Institute, 2010).

A basic cement job consists of a cement mixing unit where the base slurry is prepared, possibly a separate additive unit, the nitrogen system, and a foamed cement manifold. All flow/rate processes are generally controlled automatically (Benge et al., 1996). The foam is created when the base cement slurry flows into a tee met at a right angle by pressurized nitrogen, which is dispersed into the cement slurry via some form of atomizer. The basic equipment is similar across cementers but companies have proprietary means of dispersing the nitrogen and the nozzle design varies from company to company.

During placement of the foamed cement, at the surface of the well, either (1.) the nitrogen injection

rate is kept constant or, (2.) the foam density is kept constant (American Petroleum Institute, 2010; Loeffler, 1984). During the cement job, the nitrogen rate is controlled along with the mixing rate (in a flow process) or pumping rate (batch cement mixing) of the cement in order to maintain the required rate of nitrogen injection or density of the foam. Stabilizers and additives are generally pumped into the cement slurry prior to foaming (Benge et al., 1996). The design of the cement is based on the midpoint of cement placement depth so the changing hydrostatic pressure gradient and temperature changes occurring as the foamed cement is placed in the well must also be considered in the final cement design (American Petroleum Institute, 2010).

API recommends foam qualities below 35% for a stable foam that will maintain mechanical integrity and proper zonal isolation (American Petroleum Institute, 2010). Above 35% volume fraction of gas, the permeability may increase to unacceptable levels, and the compressive strength and ability to support the casing could be compromised. The foam should also have well dispersed bubbles that remain suspended during placement in the well without significant clustering, coalescence, or other undesirable configuration changes until the cement fully hardens (Loeffler, 1984). It is thought that the bubble sizes and extent to which the bubbles remain well dispersed affects the overall strength and performance of the cement. Coalescence or clustering of the bubbles could provide migration pathways for fluids and could reduce the compressive strength of the cement sheath.

1.4 Rheology of Cement

Cement slurry rheology is an important parameter for designing and implementing a cement job (Guillot, 1990). Cement slurries are a suspension of small particles undergoing chemical reactions and are known to have Non-Newtonian rheology, generally assumed to follow a Bingham model (Guillot, 1990; Roussel, 2005). Bingham fluids have a yield stress below which no flow occurs and after the yield stress is attained, the fluid maintains a constant viscosity. Cement slurry rheology,

however, can be time dependent and shear dependent and depend on shearing history and resting time (Guillot, 1990; Roussel, 2005). Other models that have been used to describe cement slurry rheology are the power law model, with limitations, and the Herschel-Bulkley model (Guillot, 1990). Both of these models account for the shear thinning behavior of cement and the Herschel-Bulkley model includes a yield stress. The time dependent behavior of rheology thixotropy: time-dependent shear thinning or rheoplexy: time-dependent shear thickening - is considered to be reversible. With cement, however, the hydration process will also change the rheology as time progresses (Guillot, 1990; Roussel, 2005) so it is not a truly reversible process. Cement slurry rheology is also dependent on shearing and resting history. When cements are at rest, particles within the suspension can cluster together due to random movements (Banfill, 2006; Guillot, 1990; Roussel, 2005). Shearing the suspension serves to break apart these particle clusters and is thought to lend to the shear thinning that occurs with time (Banfill, 2006; Guillot, 1990; Roussel, 2005). At low shear rates, cement slurries have been shown to be thixotropic, which means that as they are sheared, the viscosity decreases with time, though thickening can occur due to the hydration reaction. Foamed cement is a complex system and inherently dynamic, which makes it a challenge to study rheology with reliable results. Cement rheology is a function of several factors including the cement slurry design and the cement slurry production methods, and can be affected by the measurement techniques themselves (Guillot, 1990).

1.5 Rheology of Foamed Cement

Foamed cement rheology is further complicated by the addition of bubbles suspended in the cement. The changing downhole conditions in the well as the cement is pumped can affect the rheology as the quality changes. Few studies have actually been done to explore the rheological properties of foamed cement, even at ambient conditions. In the book Well Cementing (Nelson, 1990), Chapter 14: Foamed Cement (de Rozieres and Griffin, 1990) a comment is made about the lack of rheolog-

ical information and the importance of the data. At the time only one study had been referenced (Al-Mashat, 1977) and only two other studies (Ahmed et al., 2009; Olowolagba et al., 2010) have been done since the publishing of that book. Some of the conclusions of the studies contradict each other. The earlier study (Al-Mashat, 1977) uses two different capillary flow tubes (0.091 inch I.D. x 8 ft long, 0.130 inch I.D. x 8 ft long) to measure the rheology. A description of the cement, even the type used, was not included in this thesis. The cement mixer is not described fully and these specifics can influence the rheology. The cement was mixed with a "cement mixer" and injected into the system with a variable flow rate, positive displacement plunger pump, rated to 3000 psi. The foaming agent was injected into the base slurry with a variable flow rate positive displacement gear pump and mixed into the cement as the slurry flowed through a small tube coil. After air injection, the cement slurry was foamed by passing it through three stainless steel foam generator tubes (each 12 inch long x 0.33 inch I.D.) that were filled with stainless steel shavings to cause mixing and foaming.

Results span foamed cement qualities from 30% up to 65% and shear rate values from 1,000 1/s to 10,000 1/s (Al-Mashat, 1977). It was shown that the viscosity increased with increasing quality for a given shear rate and the viscosity decreased with increasing shear rate. At high shear rates (7000 1/s and higher) and qualities lower than 50%, the viscosity seems to become constant, however, typical shear rates during placement are below 1000 1/s (de Rozieres and Griffin, 1990). The viscosity as a function of quality varied between the two diameter flow tubes, with the larger tube having higher reported values. They conclude that the Power Law model or the Bingham plastic model describe the data. While a first of its kind study, pertinent details were left out of this thesis and the shear rates explored are well above those encountered during a cementing job.

The later study (Ahmed et al., 2009) uses an inline flow-through rotational viscometer to measure the rheology. The base slurry consists of Class G cement, water, and a few additives. The base slurry is made by first mixing the water, dispersant, and a fluid loss additive at 200 rpm for about 1 minute. Then the cement is added while mixing at 200 rpm for 50 s. The cement slurry (without

foamer) is agitated at 1500 rpm for 5 minutes. Rheology measurements were taken using a regular rotational bob and sleeve viscometer. The original base slurry was removed from the viscometer, placed back in the original mixing container, foamer was added and mixed gently without foaming it. To foam the cement, the cement mixture with foamer was injected into a mixing chamber where pressurized nitrogen was also injected. The cement, additives, and foamer were agitated at 1600 rpm for 5 minutes with the mixer. To measure viscosity, the foamed cement flowed through the inline viscometer at a constant rate and measured at various shear rates.

The study of Ahmed et al. (2009) is the first and only known attempt to assess the influence of pressure on the rheology. They also are the first to report viscosity values within relevant shear rates (1000 1/s or less). In conclusion, they find that a Power Law model provides the best fit to the data but at lower shear rates, the cement slurry has a yield stress, which is not captured with a Power Law model. They also show that the viscosity increases with quality for 10%, 20%, and 30% foam qualities. The discrepancy with previous reports/experience comes in their conclusion that the base slurry viscosity is higher than both the 10% and 20% foam qualities measured and, rather, is close to that of the 30% foam quality and is almost the same as the 30% foam quality for shear rates of 50 1/s and above. They question the claims that foamed cement displaces drilling muds better than neat cement as experience from industry suggests. It is unclear if these results are real or due to experimental issues. It is also possible that in measuring the foam viscosity, the foam was destabilized and the foamer reduced the slurry viscosity as compared to the base slurry, which had no foamer. The previous study from 1977 does not report data for qualities below 30% or for the neat cement. It is clear that further experimental studies are needed.

The most recent study, Olowolagba et al. (2010), uses a uniquely shaped paddle rather than a bob and sleeve viscometer to measure the viscosity and yield point. The paddle devise, a Fann Yield Stress Adapter (FYSA), was used to minimize wall slippage that can be an issue with bob and sleeve viscometers (Olowolagba et al., 2010). The FYSA is designed to minimize wall slippage, measures higher volumes of material, and keeps the bubbles and cement particles better dispersed.

The base slurry was prepared with Class H cement and water. After initial mixing at high speed in a blender, the foaming agent was added and stirred by hand without producing any foaming and then mixed in a blender to foam as recommended according to API Recommended Practices (API 10B-4, 2004). The viscosity measurements were then conducted in the viscometer unlike the former recorded measurements which were done with flow through methods. The results can be considered the most accurate viscosity measurements of foamed cement due to the advantages and reduction in errors due to the design of the FYSA. Measurements were reported for a range of volume fractions of gas: 10%, 20%, 30%, and 40%.

It is challenging to measure the rheology of a foamed cement as the methods used could affect the rheology (de Rozieres and Griffin, 1990). Foamed cements used in well cementing are pressurized and to replicate pressurized foamed cement in the laboratory requires specialized equipment to maintain the foam under pressure and perform the measurements under pressure. The methods to produce foamed cement vary among service providers and testing methods recommended in the laboratory use yet another method. So it is important to understand the foamed cement production methods to correlate rheological properties that have relevance to actual applications.

1.6 Objectives of the Work

The goal of this work is to determine the conditions that could lead to bubble clustering or structuring in a foamed cement slurry, which could lead to connected bubbles once the foamed cement cures, or which could result in crack formation along a line of bubbles. Either condition would affect the cement's ability to properly isolate the well. The following are the specific objectives of this work:

1. To understand the conditions where clustering of bubbles could occur.

2. To understand the effects of polydispersity and the bubble size distribution (BSD) on viscos-

ity and structuring during flow.

3. We have the ability to study bubble size distributions before flow [through CT imaging of experimental samples] $\longrightarrow$ We want a predictive method to determine the influence of those features.

1.7 Organization of the Thesis

The following chapters describe the development of the model and the simulation methods used to simulate bubbles in a suspension to study foamed cement. Chapter 2 describes hard spherical particle suspensions and the influence of the polydispersity in the particle sizes on the particles' rearrangements. The linear resistance terms for the polydisperse interactions were derived to match monodisperse terms that Ball and Melrose developed. The content of Chapter 2 was published in the American Society of Mechanical Engineers Journal of Applied Mechanics. Chapter 3 describes the development of a pair interaction to describe a fluid-filled sphere with bubble surface properties that include the slip on the bubble surface, the ability of the surface to deflect, and a direct force that represents the properties of the surfactant. The contents of Chapter 3 has been accepted for publication in the Mathematics and Mechanics of Solids Journal. In Chapter 4 the methods of modeling relevant bubble size distributions is described. Chapter 5 provides a summary of the results and a description of some future direction for the research.

Chapter 2: Effects of Polydispersity on Structuring and Rheology in Flowing Suspensions[1]

The size and distribution of particles suspended within a fluid influence the rheology of the suspension, as well as strength and other mechanical properties if the fluid eventually solidifies. An important motivating example of current interest is foamed cements used for carbon storage and oil and gas wellbore completion. In these applications, it is desired that the suspended particles

[1]This paper has been published. Reference: Rosenbaum, E., Massoudi, M., & Dayal, K., Effects of Polydispersity on Structuring and Rheology in Flowing Suspensions. Journal of Applied Mechanics, 2019, doi:10.1115/1.4043094.

maintain dispersion during flow and do not coalesce or cluster. This paper compares the role of mono- against poly- dispersity in the particle clustering process. The propensity of hard spherical particles in a suspension to transition from a random configuration to an ordered configuration, or to form localized structures of particles, due to flow is investigated by comparing simulations of monodisperse and polydisperse suspensions using Stokesian Dynamics. The calculations examine the role of the polydispersity on particle rearrangements and structuring of particles due to flow, and the effects of the particle size distribution on the suspension viscosity. A key finding of this work is that a small level of polydispersity in the particle sizes helps to reduce localized structuring of the particles in the suspension. A suspension of monodisperse hard spheres forms structures at a particle volume fraction of approximately 47% under shear but a 47% volume fraction of polydisperse particles in suspension does not form these structures.

Chapter 3: Surfactant Stabilized Bubbles Flowing in a Newtonian Fluid[2]

Bubbles suspended in a fluid cause the suspension to have different rheological properties than the base fluid. Generally, the viscosity of the suspension increases as the volume fraction of the bubbles is increased. A current application, and motivation for this study, is in wellbore cements used for hydrocarbon extraction and carbon sequestration. In these settings, the gas bubbles are dispersed into the cement to reduce the density as well as improve the properties for specific conditions or wellbore issues. In this paper, we use Stokesian dynamics to numerically simulate the behavior of a large number of bubbles suspended in a Newtonian fluid. Going beyond prior work on simulating particles in suspension, we account for the nature of bubbles by allowing for slip on the bubble surface, the deflection on the bubble surface, and a bubble-bubble pairwise interaction that represents the surfactant physics; we do not account for bubble compressibility. We incorporate these interactions and simulate bubble suspensions of monodisperse size at several volume fractions. We find that the bubbles remain better dispersed compared to hard spherical particles that show a greater

[2]This paper has been accepted for publication and is in press with the Mathematics and Mechanics of Solids Journal. Reference: Rosenbaum, E., Massoudi, M., & Dayal, K., Surfactant Stabilized Bubbles Flowing in a Newtonian Fluid, Mathematics and Mechanics of Solids, 2019.

tendency to structure or cluster.

Chapter 4: Suspensions of Bubbles with a Lognormal Size Distribution

Foamed cement is created by injecting gas into a cement slurry to create a dispersion of bubbles in the cement. The cement is foamed to reduce the density of the cement when a lightweight cement is needed. The size distribution of bubbles from a real foamed cement sample can be determined from analysis of computer tomography images. A pair interaction to simulate bubbles, which accounts for the nature of bubbles by allowing for slip on the bubble surface, the deflection on the bubble surface, and a bubble-bubble pairwise interaction that represents the surfactant physics, was used to simulate the size distribution matching the real foamed cement. It was possible to simulate a realistic bubble size distribution using the bubble interaction. This method can be used to simulate relevant volume fractions of bubbles that represent real foams.

1.8 Codes Used In This Work

The LAMMPS simulation code is available publicly at `lammps.sandia.gov`. Our implementation within the LAMMPS framework of the interactions described in this paper are publicly available at `github.com/eilisjill/Pair_style_bubble`.

1.9 Chapter 1 References

Bibliography

Ahmed, R. M., Takach, N. E., Khan, U. M., Taoutaou, S., James, S., Saasen, a., and Godø y, R. (2009). Rheology of foamed cement. *Cement and Concrete Research*, 39(4):353–361.

Al-Mashat, A. M. (1977). *Rheology of Foam Cement*. Doctor of philosophy, Colorado School of Mines.

American Petroleum Institute (2010). Isolating Potential Flow Zones During Well Construction - API Standard 65 Part 2.

API 10B-4 (2004). Recommended Practice on Preparation and Testing of Foamed Cement Slurries at Atmospheric Pressure ANSI / API Recommended Practice 10B-4. Technical Report July.

Banfill, P. F. G. (2006). Rheology of Fresh Cement and Concrete. *Rheology Reviews 2006*, 2006:61–130.

Benge, O. G., McDermott, J. R., Langlinais, J. C., and Griffith, J. E. (1996). Foamed cement job successful in deep HTHP offshore well. *Oil and Gas Journal*, 94.

Bikerman, J. J. (1965). Foams and Emulsions. *Industrial & Engineering Chemistry . . .* , 57(1):56–62.

Bour, D. and Rickard, B. (2000). Application of Foamed Cement on Hawaiian Geothermal Well. *Geothermal Resources Council Transactions*, 24.

Burdylo, L. and Birch, G. (1990). Primary Cementing Techniques. In Nelson, E. B., editor, *Well Cementing*, chapter 12, pages 12–1–12–27.

de Rozieres, J. and Griffin, T. J. (1990). Chapter 14 Foamed Cements. In Nelson, E. B., editor, *Well Cementing*, pages 14.1 – 14.19. Schlumberger Educational Services, 300 Schlumberger Drive, Sugar Land, Texas 77478.

Dusterhoft, D. M. (2003). Foamed & Lightweight Cements. pages 1–12.

Economides, M. J. (1990). 1. Implications of Cementing on Well Performance. In Nelson, E. B., editor, *Well Cementing*, chapter 1, pages 1.1 – 1.6. Schlumberger Educational Services, Sugar Land, Texas.

Frisch, G. J., Services, H. E., and Graham, W. L. (1999). SPE 55649 Assessment of Foamed - Cement Slurries Using Conventional Cement Evaluation Logs and Improved Interpretation Methods. *SPE Rocky Mountain Regional Meeting*.

Griffith, J. E., Lende, G., Ravi, K., Saasen, A., Nø dland, N. E., and Jordal, O. H. (2004). Foam Cement Engineering and Implementation for Cement Sheath Integrity at High Temperature and High Pressure. *IADC/SPE Drilling Conference*, (SPE 87194).

Guillot, D. (1990). Rheology of Well Cement Slurries. *Developments in Petroleum Science*, 28(C):4–1–4–37.

Kutchko, B., Crandall, D., Gill, M., McIntyre, D., Spaulding, R., Strazisar, B., Rosenbaum, E., Haljasmaa, I., Benge, G., Cunningham, E., DeBruijn, G., and Gardner, C. (2013). Computed Tomography and Statistical Analysis of Bubble Size Distributions in Atmospheric-Generated Foamed Cement. Technical Report August.

Kutchko, B., Crandall, D., Moore, J., Gill, M., McIntyre, D., Rosenbaum, E., Haljasmaa, I., Strazisar, B., Spaulding, R., Harbert, W., Benge, G., Cunningham, E., Lawrence, D. W., DeBruijn, G., and Gardner, C. (2015). Field-Generated Foamed Cement : Initial Collection , Computed Tomography , and Analysis. Technical Report July, U.S. Department of Energy, National Energy Technology Laboratory.

Langevin, D. (2000). Influence of interfacial rheology on foam and emulsion properties. *Advances in colloid and interface science*, 88(1-2):209–222.

Loeffler, N. (1984). Foamed Cement: A Second Generation. In *Permian Basin Oil and Gas Recovery Conference*.

Michaux, M., Nelson, E. B., and Vidick, B. (1990). 2. Chemistry and Characterization of Portland Cement. In Nelson, E. B., editor, *Well Cementing*, pages 2.1 – 2.17. Schlumberger Educational Services.

Nelson, E., Baret, J.-F., and Michaux, M. (1990). 3. Cement additives and mechanism of action. In Nelson, E. B., editor, *Well Cementing*, pages 3.1 – 3.37. Schlumberger Educational Services.

Nelson, E. B. (1990). *Well cementing*, volume 28. Newnes.

Olowolagba, K. O., Brenneis, C., et al. (2010). Techniques for the study of foamed cement rheology. In *SPE Production and Operations Conference and Exhibition*. Society of Petroleum Engineers.

O'Rourke, T. J. N. S. C. and Crombie, D. N. S. C. (1999). A Unique Solution to Zonal Isolation Utilizing Foam-Cement and Coiled-Tubing Technologies. *Society of Petroleum Engineers*, (SPE 54473).

Pugh, R. J. (1996). Foaming, foam films, antifoaming and defoaming. *Advances in Colloid and Interface Science*, 64(95):67–142.

Pugh, R. J. (2005). Experimental techniques for studying the structure of foams and froths. *Advances in colloid and interface science*, 114-115:239–251.

Rae, P. (1990). Cement Job Design. In Nelson, E. B., editor, *Well Cementing*, chapter 11, pages 11.1 – 11.17. Schlumberger Educational Services, Sugar Land, Texas.

Roussel, N. (2005). Steady and transient flow behaviour of fresh cement pastes. *Cement and Concrete Research*, 35:1656–1664.

White, J., Moore, S., Miller, M., Faul, R., and Services, H. E. (2000). IADC / SPE 59136 Foaming Cement as a Deterrent to Compaction Damage in Deepwater Production. *2000 IADC/SPE Drilling Conference*.

Chapter 2

Effects of Polydispersity on Structuring and Rheology in Flowing Suspensions[1]

2.1 Abstract

The size and distribution of particles suspended within a fluid influence the rheology of the suspension, as well as strength and other mechanical properties if the fluid eventually solidifies. An important motivating example of current interest is foamed cements used for carbon storage and oil and gas wellbore completion. In these applications, it is desired that the suspended particles maintain dispersion during flow and do not coalesce or cluster. This paper compares the role of mono- against poly- dispersity in the particle clustering process. The propensity of hard spherical particles in a suspension to transition from a random configuration to an ordered configuration, or to form localized structures of particles, due to flow is investigated by comparing simulations of monodisperse and polydisperse suspensions using Stokesian Dynamics. The calculations examine the role of the polydispersity on particle rearrangements and structuring of particles due to flow, and

[1]This paper has been published. Reference: Rosenbaum, E., Massoudi, M., & Dayal, K., Effects of Polydispersity on Structuring and Rheology in Flowing Suspensions. Journal of Applied Mechanics, 2019, doi:10.1115/1.4043094.

the effects of the particle size distribution on the suspension viscosity. A key finding of this work is that a small level of polydispersity in the particle sizes helps to reduce localized structuring of the particles in the suspension. A suspension of monodisperse hard spheres forms structures at a particle volume fraction of approximately 47% under shear but a 47% volume fraction of polydisperse particles in suspension does not form these structures.

2.2 Introduction

The motivation for this study is to better understand the viscoelastic properties of foamed well cement, due to the addition of bubbles to the cement slurry. Foamed cement is created by dispersing gas, usually an inert gas like nitrogen, into cement slurry to create a suspension composed of bubbles and solid particles. Foamed cement is used in wellbores requiring a lower density cement, such as wells drilled into weak or fractured formations (Loeffler, 1984). In the wellbore, cement is placed between the steel casing at the center of the well and the formation. Cement is used to isolate and seal wells in carbon storage and hydrocarbon extraction and to support the casing. The process of foaming the cement slurry lowers the density of the cement as necessary for the application, without changing the cement chemistry and while maintaining its compressive strength.

Cement is a highly complex material with properties that change over time. The cement slurry is made up of the cement clinker (a powdery mix of materials - primarily lime, silica, alumina, and iron) that when mixed with water begins the chemical reaction in the form of a hydration process (de Rozieres and Griffin, 1990). During the hydration process the chemical and the physical properties of the cement slurry are changing. However, during the induction period when the cement is placed in the wellbore, little hydration occurs and the slurry properties remain fairly constant. We are interested in the foamed cement properties during its placement in the wellbore.

The bubble sizes and their distribution play a key role in the properties of foamed cement, including stability (de Rozieres and Griffin, 1990). The American Petroleum Institute (API) recommends

foamed cement slurries be designed to have an added gas volume fraction below 35% at the placement depth for a stable foam that will maintain the mechanical integrity and the proper zonal isolation (American Petroleum Institute, 2010). Above 35% volume fraction of gas, the permeability may increase to unacceptable levels, and the compressive strength and the ability to support the casing could be compromised. Pressures vary throughout the cement process due to different depths in the well; we, therefore, study a range of volume fractions (10% to 50%). The foam should also have well dispersed bubbles that remain suspended during placement in the well without significant clustering, coalescence, or other undesirable configuration changes until the cement fully hardens (Loeffler, 1984). Clusters of bubbles in foamed cement could increase the permeability once cured because the bubbles can become interconnected. If the bubbles become ordered and form structures of closely configured bubbles in the set cement, they weaken the effectiveness of the cement by forming weak points for crack formation, which creates pathways for fluid to flow and compromises the strength of the cement (Tan et al., 2007a,b). Cracks can also increase the permeability beyond the acceptable levels to provide proper zonal isolation.

Foamed cement samples produced in the laboratory that have come to a steady flow condition show bubble rearrangement due to flow and subsequent clustering of the bubbles (NETL, 2019). Comparable foamed cement samples that were captured before attaining a steady flow, show no clustering of the bubbles which remained in a random configuration. It is therefore evident that the flow influences the properties of the foamed cement.

Our aim here is to study the influence of size distributions on the final arrangement of the particles under flow using numerical simulations. We use the Stokesian Dynamics method (Brady, 1988), in the more efficient recent Fast Lubrication Dynamics (FLD) approximation (Bybee, 2009; Kumar, 2010; Kumar and Higdon, 2010). This method enables us to track the location of all the particles during the simulation, and thereby obtain insights into smaller scale phenomena such as the detailed particle spatial distribution and structuring. Particles can arrange into structures, where the particles become closer together. Higher levels of structuring will show the particles arrange in a single line

of particles. Structuring of any kind could result in weakness along the line of particles.

2.3 Approach to Mathematical Modeling of Suspensions

2.3.1 Background

In this section, we will provide a brief discussion of various approaches to mathematically model a complex fluid which is composed of particles suspended in a fluid. In general, we can talk about non-flowing multicomponent systems, such as composite materials (the different components can undergo elastic or plastic deformations without involving any motion), or flowing multicomponent materials such as coal or cement slurries, fluidization, etc. We will limit our discussion to a two-component flowing system, composed of particles and a host fluid. The fluid can be either a gas or a liquid and the particles can be rigid (such as sand) or deformable (such as drops or bubbles). It is possible to study (model) these flows using continuum theories, statistical theories or numerical simulations.

From a continuum mechanics perspective, there are a few ways to study a two-component (sometimes called a two-phase) system (see (Soo, 1967; Wallis, 1969)). The first approach is used when the two components interact with each and each component influences the motion and the behavior of the other component. This is usually known as the Dense Phase approach, or the Eulerian (two-fluid) approach. This method can be used to study fluidization, gas-solid flows, pneumatic conveying, and suspensions, etc. These ideas can be traced back to the pioneering work of Truesdell in 1957 (see (Truesdell, 1984)) and in the context of continuum theories, they are named mixture theories (see the review articles in references (Atkin and Craine, 1976; Bowen, 1976) and the book (Rajagopal and Tao, 1995)). For a recent review and discussion of the relevant issues, see the two articles: (Massoudi, 2008) and (Massoudi, 2010). The basic assumption is that at any instant of time, every point in space is occupied by one particle from each constituent. The theory

provides a means for studying the motions of bodies composed of several constituents by generalizing the equations for the mechanics of a single continuum . This method is probably the most comprehensive and the most difficult method to use, since in general, it would involve solving partial differential equations and requires many constitutive relations. When thermal, chemical, and electromagnetic effects are ignored, and assuming no inter-conversion of mass between the two components, the governing equations are the conservation equations for mass, linear momentum and angular momentum for each component. These are given for the two constituents:

$$\frac{\partial \rho^i}{\partial t} + \operatorname{div}(\rho^i \boldsymbol{v}^i) = 0, \text{ where } i = s, f \tag{2.3.1.1}$$

Where s and f refer to the solid and fluid components, respectively, div is the divergence operator, $\boldsymbol{v}^i$ is the velocity vector, and ρ^i designates the density. The densities in the current and reference configuration are related through the kinematical field $\phi(x,t)$, called volume fraction (sometimes referred to as porosity), such that:

$$\rho_s = (1-\phi)\rho_R^s \tag{2.3.1.2}$$

$$\rho_f = \phi \rho_R^f \tag{2.3.1.3}$$

Where $0 \leq \phi(\boldsymbol{x},t) \leq \phi_{max} < 1$. Thus when $\phi = 1$, there are no particles and the suspension is simply a pure fluid. Note that Equations (2.3.1.2) and (2.3.1.3) imply that the mixture is saturated. Otherwise, the porosities are constrained by $\phi_s + \phi_f \leq 1$. The balance of linear momentum for the two components is given by

$$\rho^i \frac{(d^i \boldsymbol{v}^i)}{dt} = \operatorname{div} \boldsymbol{\sigma}^i + \rho^i \boldsymbol{b}^i + \boldsymbol{m}^i, \text{ where } i = s, f \tag{2.3.1.4}$$

Where $\boldsymbol{b}^i$ is the external body force, $\boldsymbol{m}^i$ is the interaction forces, $\boldsymbol{\sigma}^i$ designate the partial stress tensor and $\frac{d^i(.)}{dt} = \frac{\partial(.)}{\partial t} + [\boldsymbol{v}^i \mathrm{grad}(.)]$. In the absence of couple stresses, the balance of angular momentum indicates that the total stress tensor for the mixture is symmetric. To solve these equations, at least three constitutive relations are needed: two (tensor) equations for the two stress tensors and one (vector) equation for the interaction forces, which could include terms such as drag, lift, relative acceleration (virtual mass), history effects, etc. (see (Massoudi, 2002, 2003)). A point to notice is that in any of these continuum-based theories, a new kinematical field, namely the volume fraction (concentration, porosity) has been added to the list of the parameters of interests, namely, velocity, density, and pressure. For problems involving heat transfer, temperature also need to be added. Similarly, for problems dealing with chemical reactions or electro-magnetic effects additional fields will have to be introduced. Furthermore, in these mixtures-based theories, the distinct characteristics of particles, such as size, shape, surface roughness, etc., do not enter the equations in a direct manner; at best, some of the information can be included in some of the coefficients which appear in the constitutive relations such as the drag force. There are, however, micro-continuum theories, where a length scale can be introduced (see (Eringen, 2007)).

In the second approach, the amount of the dispersed particles is so small that their motion does not affect the motion of the host fluid. This occurs in applications such as atomization, sprays, pollution, etc. This approach is known as the Dilute Phase or the Lagrangian approach. In this case, there is a one-way coupling, namely the motion of the fluid affects the motion of the particles but not the other way around. The equations which need to be solved simultaneously are the force equation for the particles (which will include a source term due to the motion of the fluid, usually in the form of interaction forces such as drag, which depends on the relative velocity) and the conservation of mass and linear momentum equations for the fluid (see (Clift, 1978; Crowe et al., 1998; Sadhal et al., 1997)). The constitutive parameters which are needed are the stress tensor for the fluid component and the interaction forces. To obtain the basic equation governing the motion of a particle suspended or entrained in a fluid, most researchers start with the equation of motion of a single (spherical) particle in a fluid. Tchen (Tchen, 1947) synthesized the work of Basset,

Boussinesq, Stokes, and Oseen on the motion of a sphere settling under the force of gravity in a fluid at rest. The resulting equation is usually called the BassetBoussinesqOseen (BBO) equation. This equation went through a series of revisions and updates; it is generally accepted that a three-dimensional form of the BBO equation in a nonuniform flow is given by Maxey and Riley (1983) (Maxey and Riley, 1983):

$$\begin{aligned} m_s \frac{d\boldsymbol{v}_s}{dt} &= m_f \frac{\mathrm{D}\boldsymbol{v}_f}{\mathrm{D}t} \\ &- \frac{1}{2} m_f \frac{d}{dt}\Big\{\boldsymbol{v}_s(t) - \boldsymbol{v}_f(t) - \frac{1}{10}a^2\nabla^2\boldsymbol{v}_f\Big\} \\ &- 6\pi a\mu_f\Big\{\boldsymbol{v}_s(t) - \boldsymbol{v}_f(t) - \frac{1}{6}a^2\nabla^2\boldsymbol{v}_f\Big\} \\ &+ 6\pi a^2\mu_f \int_0^t \mathrm{d}\tau \frac{\frac{d}{dt}\Big\{\boldsymbol{v}_s(\tau) - \boldsymbol{v}_f(\tau) - \frac{1}{6}a^2\nabla^2 v_f\Big\}}{\sqrt{\pi\nu_f(t-\tau)}} \\ &+ (m_s - m_f)\boldsymbol{g} \end{aligned} \tag{2.3.1.5}$$

where $\boldsymbol{v}_s$ is the velocity of the particle, $\boldsymbol{v}_f$ is the velocity of the fluid, a is the particle radius, g is the acceleration of gravity, μ_f and ν_f are the dynamic viscosity and the kinematic viscosity of the fluid, respectively. The second term on the right-hand side (RHS) of Equation (2.3.1.5) reflects the presence of the virtual mass, the third term is the Stokes drag, the fourth term is the Basset history effects, and the last term is the buoyancy. The inclusion of velocity gradients (the first term on the RHS) results in modifications to the virtual mass, the Stokes drag, and the Basset history terms to account for the effect of a nonuniform flow field. These velocity gradients correspond to the physical effect known as Faxen forces (Happel and Brenner, 1973).

In certain engineering applications, where we are interested in global or macroscopic behavior of these suspensions, we model them as a single component fluid, usually represented by a single non-linear constitutive relation (for the stress tensor) where the material properties are functions of volume fraction of the particles. In these cases, we are not concerned about the amount of

particles (whether dilute or dense) in the suspension and usually we are interested in the (total) flow rate, pressure drop, etc.; these can be obtained by solving the basic equations of motion. Also, there is only one constitutive relation which is needed for the stress tensor of the suspension. This approach, often called suspension rheology, in general cannot provide us with particle distributions, deposition, etc., unless certain convection-diffusion type equations are also used (see (Wu et al., 2017)).

From the statistical mechanics point of view, sometimes a particle dynamics approach (simulation) is used and sometimes a modified form of the kinetic theory of gases, as applied to rigid particles are used. These two techniques, especially with faster and more efficient computers have become more popular in the last few decade (see review articles dealing with the statistical theories by Herrmann (Herrmann, 1999; Herrmann and Luding, 1998) and kinetic theories application to granular materials by Goldhirsh (Goldhirsch, 2003), or numerical simulation by Walton (Walton and Braun, 1986)).

In the next section, we will discuss and use the Stokesian Dynamics approach (a molecular dynamics-like method) and how it can be used to study the flow of a suspension.

2.3.2 Model Assumptions

We make several assumptions about the system of interest.

First, *the bubbles are assumed to be hard sphere particles*. Laboratory experiments show that the surfactants and stabilizers added to the base fluid maintain fairly spherical, stable, discrete bubbles in the flow regime typically encountered in the well (Dalton et al., 2018). The surfactants also cause the bubbles to typically have minimal direct contact. It should be noted that treating bubbles as deformable elastic objects is an area of active research, e.g., (Rahimian et al., 2015), and infeasible for the large systems required here.

Second, *the suspending fluid (cement slurry) is considered Newtonian*. It is generally accepted that cement slurry has a yield stress and can behave in highly nonlinear manner (Guillot, 1990; Roussel, 2005). However, we emphasize that there exists no feasible way to simulate large collections of particles in non-Newtonian fluids while accounting for all particle positions. Therefore, while our simulations provide useful insights into some of the properties of the bubbles that control the real system behavior, particularly the clustering and structuring of bubbles, it is important to note that one should expect qualitative and quantitative differences compared to experiments.

Third, *the buoyancy of the bubbles is neglected*. Unlike aqueous foam solutions where the bubbles tend to rise due to buoyancy, bubbles in cement tend to remain in place unless they reach a critical size. This has been observed experimentally (Kutchko et al., 2013, 2015): in laboratory and field applications, the bubble sizes are kept below this critical size and were observed to remain where placed during curing (Kutchko et al., 2015). This is reasonable considering that cement is a yield-stress fluid, and the yield stress must be overcome for the cement to flow around a bubble. In addition, the cement slurry particles, which act as surface active foaming materials, help keep the bubbles entrained (Pugh, 1996).

2.3.3 Stokesian Dynamics

In a suspension of particles, the motion of each particle is transmitted through the suspending fluid. In the quasi-static (creeping flow) limit, this is felt immediately throughout the entire system by all the other particles. Therefore long-range effects should be carefully considered. For a dilute suspension of particles where the particles are far apart, the detailed shape and structure of the particles does not matter to leading-order. The velocity disturbance of one particle decays like a point force as $1/r^2$, where r is the radial distance from the particle (Brady, 1988). When the particles are close together, the interaction of each particle pair is dominated by a pairwise force which comes from lubrication theory (Kim and Karrila, 2005). This force is on the order of $1/h$ for

rigid particles with no-slip surfaces, where h is the gap between the particle surfaces. As the gap between the particles gets smaller, the force between them increases rapidly and the approaching particles cannot contact in finite time. In the setting of interest, both the far-field and the near-field interactions must be considered in hydrodynamic interactions. The Stokesian Dynamics method account for the far-field interaction through multipole expansions and for the near-field interactions through pairwise interactions (Brady, 1988). This was later made more computationally efficient through the use of lubrication theory for the near-field interactions (Ball and Melrose, 1997). The FLD method further increased the efficiency by using fast approximate methods for the far-field interaction (Bybee, 2009; Kumar, 2010). The broader idea of developing multiscale methods for long-range interactions by decomposing into far- and near- field and then using multipole expansions for the far-field has been studied theoretically and numerically in the context of bubbly fluids (Sangani and Acrivos, 1983) and electromagnetic interactions (James and Müller, 1994; Marshall and Dayal, 2014; Xiao, 2005).

In a Newtonian fluid when the inertial term is neglected, we obtain the Stokes flow regime. The governing equation is a linear biharmonic equation, thereby allowing superposition. Given a flow with multiple particles, the flow due to each particle is given by a fundamental solution denoted by a Stokeslet, and the interaction between particles can be obtained by superposing appropriately the Stokeslets solutions. This enables an *effective* pairwise interaction between particles where the influence of the mediating fluid is accounted through the Stokeslet. Bossis and Brady were the first to develop this idea and put this into the framework of pairwise molecular dynamics to enable the efficient simulation of suspensions (Bossis and Brady, 1984; Brady, 1988). This method is denoted "Stokesian Dynamics".

For the Stokes flow regime, the viscous forces dominate and the inertial forces have negligible effects. The movement of a particle is governed by the equation (Bossis and Brady, 1984; Kumar and Higdon, 2010):

$$\boldsymbol{m} \cdot \frac{d\boldsymbol{U}}{dt} = \boldsymbol{F}^{H} \tag{2.3.3.1}$$

Here, $\boldsymbol{U}$ is the generalized velocity vector of the particles with entries corresponding to both linear and angular velocities. The velocity vector therefore has 6 components, corresponding to linear and angular velocities along the Cartesian directions, for each particle. Correspondingly, $\boldsymbol{m}$ is the generalized moment of inertia matrix containing entries for mass as well as the rotational inertia and, $\boldsymbol{F}^H$ is the generalized force vector with entries for both force as well as moment. Contained in this hydrodynamic force vector are then the 6 Cartesian components of the force and torque for each particle.

Note that the hydrodynamic force $\boldsymbol{F}^H$ accounts for the flow-induced forces as well as forces due to other particles that are mediated through the fluid. Direct inter-particle forces, such as in charged systems or when they come directly in contact, and forces due to Brownian motion are not considered. In this study, there are no direct inter-particle forces, and Brownian forces are neglected because the particles are much bigger than the scale at which these are significant.

Consider a macroscopically uniform (i.e., affine) flow field $\boldsymbol{v}(\boldsymbol{x}) = \boldsymbol{A}\cdot\boldsymbol{x} + \boldsymbol{B}$, where $\boldsymbol{A}$ is the velocity gradient tensor and $\boldsymbol{B}$ is the mean velocity. The symmetric rate-of-strain tensor is defined $\boldsymbol{E}^\infty = \frac{1}{2}(\boldsymbol{A} + \boldsymbol{A}^T)$. The spin tensor is defined by $\boldsymbol{W} = \frac{1}{2}(\boldsymbol{A} - \boldsymbol{A}^T)$ and the axial vector corresponding to this skew-symmetric tensor is $\boldsymbol{w}$. The generalized far-field velocity $\boldsymbol{U}^\infty$ is defined by $\boldsymbol{B}$ and $\boldsymbol{w}$.

The hydrodynamic forces can be determined by the relationship between the particle velocities and forces due to the suspending fluid by:

$$\begin{pmatrix} \boldsymbol{F}^H \\ \boldsymbol{S}^H \end{pmatrix} = \mathcal{R} \cdot \begin{pmatrix} \boldsymbol{U}^\infty - \boldsymbol{U} \\ \boldsymbol{E}^\infty \end{pmatrix} \tag{2.3.3.2}$$

The symmetric first moment of the force, $\boldsymbol{S}^H$, is called the Stresslet. $\mathcal{R}$ is the resistance matrix, and contains the particle positions. The main outcome of Stokesian Dynamics and FLD is to more efficiently compute $\mathcal{R}$ so that large numbers of particles in a suspension can be simulated.

Both (Bossis and Brady, 1984) and (Brady, 1988) compared two methods of adding particle interactions for a suspension: first, by constructing the mobility matrix $\mathcal{M}$ or by constructing the resistance matrix $\mathcal{R}$[2]. The computation time to construct $\mathcal{R}$ is significantly greater than for $\mathcal{M}$, but the particles overlap in using the mobility matrix, and the physics are not preserved. The reason for this issue with the $\mathcal{M}$ matrix is that it does not accurately capture the lubrication forces that prevent the particles from overlapping, and therefore $\mathcal{M}$ does not preserve the physics of the problem.

Brady and Bossis first construct the grand mobility matrix, $\mathcal{M}^{\infty}$, and invert it for an approximation to the resistance matrix to determine the far-field interactions. Inverting $\mathcal{M}^{\infty}$ approximates the far-field many-body interactions efficiently. However, $\mathcal{M}^{\infty}$ does not include the exact lubrication forces. To account for the exact near-field lubrication interactions, a resistance matrix can be used that has the exact two-body lubrication interactions, represented by $\mathcal{R}_{2B}$. However, this leads to double counting of some lubrication terms which must be subtracted; this is represented by the matrix $\mathcal{R}^{\infty}_{2B}$. This process can be represented by (Brady, 1988):

$$\mathcal{R} = (\mathcal{M}^{\infty})^{-1} + \mathcal{R}_{2B} - \mathcal{R}^{\infty}_{2B} \tag{2.3.3.3}$$

Stokesian Dynamics preserves all the relevant physics of the problem but is computationally intense for systems with a large number of particles. To allow for larger systems while still maintaining the physics of the problem in accounting properly for far-field and near-field interactions, *Fast Lubrication Dynamics* (FLD) was developed (Bybee, 2009; Kumar, 2010).

2.3.4 Fast Lubrication Dynamics (FLD)

The Fast Lubrication Dynamics (Bybee, 2009; Kumar, 2010) explicitly incorporates the lubrication interactions, following (Ball and Melrose, 1997), but modifies the Stokesian Dynamics (Brady, 1988) to reduce the computation time. In FLD, the grand resistance matrix, denoted $\mathcal{R}_{FLD}$, is

[2] $\mathcal{R}$ and $\mathcal{M}$ are not precisely inverses of each other but are closely related (Kim and Karrila, 2005).

the sum of the near-field pairwise lubrication interactions and the far-field interactions from the diagonal components of an isotropic resistance tensor, $\mathcal{R}_{Iso}$. The lubrication terms come directly from (Ball and Melrose, 1997).

The matrix $\mathcal{R}_{Iso}$ aims to approximate $(\mathcal{M}^{\infty})^{-1}$ in an efficient manner. To achieve this, $\mathcal{R}_{Iso}$ is assumed to have the form of a multiple of the identity matrix. The multiplicative factor – assumed to be a function of the volume fraction – is obtained by curve-fitting the short-time self-diffusivity results from FLD to those obtained from full Stokesian Dynamics. In this way, FLD aims to preserve the physics of the accurate Stokesian Dynamics approach while making the computation more efficient. The resistance matrix used in FLD is described by:

$$\mathcal{R}_{FLD} = \mathcal{R}_{Iso} + \mathcal{R}_{2B} - \mathcal{R}_{2B}^{\infty} \tag{2.3.4.1}$$

The full expressions of the lubrication force and torque were derived by (Jeffrey and Onishi, 1984), see also (Kim and Karrila, 2005). (Ball and Melrose, 1997) derive expressions from the lubrication solutions to describe the modes of motion of both particles in the particle pair interaction.

We note below an important though subtle issue regarding the implementation of FLD in the molecular dynamics code LAMMPS (described further below). (Ball and Melrose, 1997) give the expressions for the lubrication forces and torques of each particle in the pair interaction. Using these full expressions, including all the $\log$ terms, is important to accurately simulate monodisperse hard spherical particles with no-slip on their boundaries that are only interacting through hydrodynamic forces.

However, LAMMPS uses truncated expressions that leave out some terms. The truncated expressions in LAMMPS are generally used with other forces such as Brownian, colloidal, electrostatic, and so on. The error due to the missing terms can be negligible if other interactions dominate. However, we find that it is important to use the full expressions when computing the relative viscosity. For instance, Figure 2.4 shows the relative viscosity as a function of volume fraction computed

by Stokesian Dynamics (Bossis and Brady, 1984; Brady, 1988), FLD with truncated expressions (Bybee, 2009), Ball and Melrose (Ball and Melrose, 1997), and our FLD calculations. We notice, particularly as the volume fraction increases, that Stokesian Dynamics, our FLD calculations, and (Ball and Melrose, 1997) all have good agreement. In contrast, the FLD calculations with the truncated expressions show increasingly significant deviations with the volume fraction.

2.3.5 Near-Field Lubrication Interactions for Particles of Different Sizes

Given a pair of particles 1 and 2, both with the radius a and a separation h between the particle surfaces, we can then write the lubrication forces $\boldsymbol{f}_i$ and torques $\boldsymbol{g}_i$ on each of the particles following (Ball and Melrose, 1997):

$$\boldsymbol{f}_1 = -\boldsymbol{f}_2 = -a_{sq}\mathbb{N}\cdot(\boldsymbol{v}_1-\boldsymbol{v}_2) - a_{sh}\left(\frac{2}{r}\right)^2\mathbb{P}\cdot(\boldsymbol{v}_1-\boldsymbol{v}_2) + \left(\frac{2}{r}\right)a_{sh}\boldsymbol{n}\times\mathbb{P}\cdot(\boldsymbol{\omega}_1+\boldsymbol{\omega}_2)$$

(2.3.5.1a)

$$\boldsymbol{g}_1 = -\left(\frac{2}{r}\right)a_{sh}\boldsymbol{n}\times\mathbb{P}\cdot(\boldsymbol{v}_1-\boldsymbol{v}_2) - a_{sh}\mathbb{P}\cdot(\boldsymbol{\omega}_1+\boldsymbol{\omega}_2) - a_{pu}\mathbb{P}\cdot(\boldsymbol{\omega}_1-\boldsymbol{\omega}_2) - a_{tw}\mathbb{N}\cdot(\boldsymbol{\omega}_1-\boldsymbol{\omega}_2)$$

(2.3.5.1b)

$$\boldsymbol{g}_2 = -\left(\frac{2}{r}\right)a_{sh}\boldsymbol{n}\times\mathbb{P}\cdot(\boldsymbol{v}_1-\boldsymbol{v}_2) - a_{sh}\mathbb{P}\cdot(\boldsymbol{\omega}_1+\boldsymbol{\omega}_2) + a_{pu}\mathbb{P}\cdot(\boldsymbol{\omega}_1-\boldsymbol{\omega}_2) + a_{tw}\mathbb{N}\cdot(\boldsymbol{\omega}_1-\boldsymbol{\omega}_2)$$

(2.3.5.1c)

$\boldsymbol{n}$ is the unit vector directed along the line connecting the center of particle 1 pointing toward particle 2, $\mathbb{N} := \boldsymbol{n}\otimes\boldsymbol{n}$, and $\mathbb{P} := \boldsymbol{I} - \mathbb{N}$. $\boldsymbol{v}$ and $\boldsymbol{\omega}$ are the velocity and the angular velocity, respectively, of the particles. The expressions in (3.4.1.1) provide the components of $\mathcal{R}_{2B}$. Noting that the left side – $\boldsymbol{f}, \boldsymbol{g}$ – in (3.4.1.1) corresponds to the generalized force $\boldsymbol{F}^H$, and is linearly related to $\boldsymbol{v}, \boldsymbol{\omega}$ that correspond to the generalized velocity $\boldsymbol{U}$.

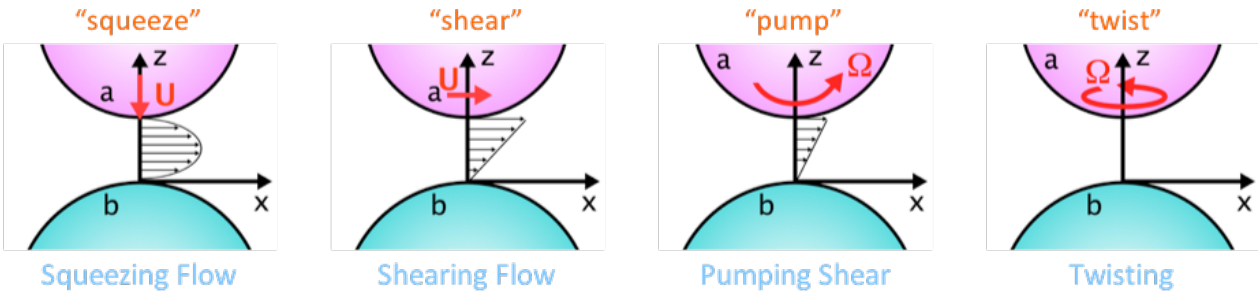

Figure 2.1: Particle pair interactions are shown for four motions of particle a relative to particle b.

Particle pairs have four modes of interaction that have been termed *squeeze* (sq), *shear* (sh), *pump* (pu), and *twist* (tw). These are shown schematically in Figure 2.1.

For two particles that have the same radius a, (Ball and Melrose, 1997) derived the dominant pair interactions by first defining:

$$a_{sq} = 6\pi\mu a \left[\frac{1}{4h} + \frac{9}{40}\log\frac{1}{h} + \frac{3}{112}h\log\frac{1}{h}\right] \tag{2.3.5.2a}$$

$$a_{sh} = \pi\mu a^3 \left[\frac{(2+h)^2}{4}\log\frac{1}{h}\right] \tag{2.3.5.2b}$$

$$a_{pu} = 8\pi\mu a^3 \left[\frac{3}{160}\log\frac{1}{h} + \frac{63}{4000}h\log\frac{1}{h}\right] \tag{2.3.5.2c}$$

μ is the suspending fluid viscosity without the particles. The twist term from (Ball and Melrose, 1997) was not included for our simulations as the contribution is negligible, i.e. $a_{tw} = 0$.

For two particles with unequal radii a and b, the linear resistance depends on the ratio $\beta = \frac{b}{a}$. (Kim and Karrila, 2005) give the equations for the force and torque on particle a, which is moving as shown in Figure 2.1, and particle b which is stationary. To determine the shearing terms, it is important to combine properly the shearing and shearing pump motion, following the description in (Ball and Melrose, 1997). To obtain the a_{sh} term, the force on particle a due to pure shearing motion must be multiplied by $\frac{(2+h)^2}{4}$ to include the Lorentz relationships as (Ball and Melrose, 1997) have included in the Equations of 3.4.1.1. To obtain a_{pu}, g_{11} and g_{12} (from (Jeffrey and

Onishi, 1984)) were combined (i.e. $g_{11} + g_{12}$) as done in (Ball and Melrose, 1997).

The equations for a_{sq}, a_{sh}, a_{pu}, generated from the solutions shown in (Kim and Karrila, 2005), and following (Ball and Melrose, 1997) are now:

$$a_{sq} = 6\pi\mu a \left[\frac{\beta^2}{(1+\beta)^2} \frac{1}{h} + \frac{1+7\beta+\beta^2}{5(1+\beta)^3} \log\frac{1}{h} + \left(\frac{1+18\beta-29\beta^2+18\beta^3+\beta^4}{21\,(1+\beta)^4} \right) h \log\frac{1}{h} \right] \tag{2.3.5.3a}$$

$$a_{sh} = 6\pi\mu a^3 \left(1 + h + \frac{1}{4}h^2\right) \left[\frac{4\beta\,(2+\beta+2\beta^2)}{15\,(1+\beta)^3} \log\frac{1}{h} + \frac{4\,(16-45\beta+58\beta^2-45\beta^3+16\beta^4)}{375\,(1+\beta)^4} h \log\frac{1}{h} \right] \tag{2.3.5.3b}$$

$$a_{pu} = 8\pi\mu a^3 \left[\frac{4-\frac{1}{\beta^2}}{80\left(1+\frac{1}{\beta}\right)} \log\frac{1}{h} + \frac{132+24\frac{1}{\beta}-11\frac{1}{\beta^2}+24\frac{1}{\beta^3}-43\frac{1}{\beta^4}}{2000\left(1+\frac{1}{\beta}\right)^2} h \log\frac{1}{h} \right] \tag{2.3.5.3c}$$

We use these expressions in (3.4.1.1) to obtain $\mathcal{R}_{2B}$ for the case of two non-identical particles.

2.4 Numerical Simulations and Results

LAMMPS[3] – the Large-scale Atomic/Molecular Massively Parallel Simulator – is an open-source classical (non-quantum) molecular dynamics code developed and maintained at Sandia National Labs (Plimpton, 1995). We use LAMMPS with the FLD method[4].

2.4.1 Implementation of the Shearing Flow

Three dimensional simulations were performed using the Lees-Edwards periodic boundary conditions (Lees and Edwards, 1972). The velocity of each particle is a function of its position in the

[3] `lammps.sandia.gov`

[4] As noted previously, we have extended LAMMPS to include the full expression for lubrication terms from (2.3.5.3).

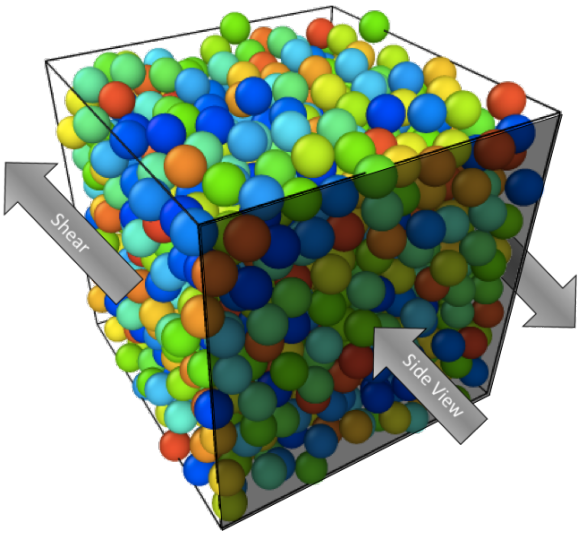

Figure 2.2: The particles are sheared in the direction shown and the images below are shown from the side view and looking through the whole sample.

y-direction for strains imposed in the xy-direction. When a particle crosses the simulation boundary, the velocity is remapped to correspond to the new position in the simulation box[5]. The different suspensions were sheared as shown in Figure 3.9 until the stress had reached a constant value and a strain of 200 was reached. It was shown through testing different time steps, Δt (time units) that the dimensionless time step should be kept below 0.002 for the FLD simulations. An explicit time integration was used.

For the quasi-static setting, the only physical parameter is the total strain or the product of strain rate and timestep, $\dot{\gamma}$ (1/time units) $\times \Delta t$. For a given value of $\dot{\gamma} \times \Delta t$, the time-history of the stress and viscosity should be the same when time is appropriately re-scaled.

The stress in the system is calculated by summing the stresses computed for each particle. Ignoring the kinetic energy contributions that are negligible here, the stress on a particle is defined by (LAM, 2003; Tadmor and Miller, 2011):

$$\sigma_{i,\alpha\theta} = \frac{1}{V_i}[-\frac{1}{2}\sum_{n=1}^{N_p}(r_{1_\alpha}F_{1_\theta} + r_{2_\alpha}F_{2_\theta})] \tag{2.4.1.1}$$

[5]See e.g. (Dayal and James, 2010) for a discussion of this and (LAM, 2003) for the implementation.

Where α and θ run over the coordinate directions to compute the 6 components of the symmetric stress tensor. The sum runs over the N_p neighbors of the particle under consideration. $\boldsymbol{r}_1$ and $\boldsymbol{r}_2$ are the positions of every particle pair that has pairwise interactions, and $\boldsymbol{F}_1$ and $\boldsymbol{F}_2$ are the corresponding forces.

For a simulation box with volume, V, the stress from each particle is summed to determine the total stress of the system of particles and is used to calculate the viscosity. With Lees-Edwards boundary conditions imposed, the relative viscosity, or more accurately, the viscosity ratio, is then calculated from the average total stress once the system has reached equilibrium:

$$\mu_{\text{relative}} = \frac{\mu_{\text{effective}}}{\mu} = \frac{\sum_i \sigma_{xy}}{\dot{\gamma}\mu V} \tag{2.4.1.2}$$

2.4.2 Generation of Initial Configurations of Particles

Particle systems were generated by randomly placing particles with a diameter of 1 in a $10 \times 10 \times 10$ box to create different volume fractions ($10\%, 20\%, 30\%, 40\%, 45\%, 50\%$) of particles all having the same system volume. Once the particles are randomly placed, a soft potential is used with an energy minimization to remove overlaps in the initial configuration that are unphysical[6]. The energy of the soft potential is (LAM, 2003):

$$E = A\left(1 + \cos\left(\frac{\pi r}{r_{cut}}\right)\right), \quad r < r_{cut} \tag{2.4.2.1}$$

where r is the distance between particles, A is the pre-factor in energy units that was initially set low and ramped up, and r_{cut} is the cut off distance.

To avoid effects from the system size, testing was done to determine the appropriate system size that shows no further size dependence. The system sizes were progressively doubled in all coordinate

[6]We emphasize that the soft potential is used only in generating a physical initial configuration, and plays no role once the simulation begins.

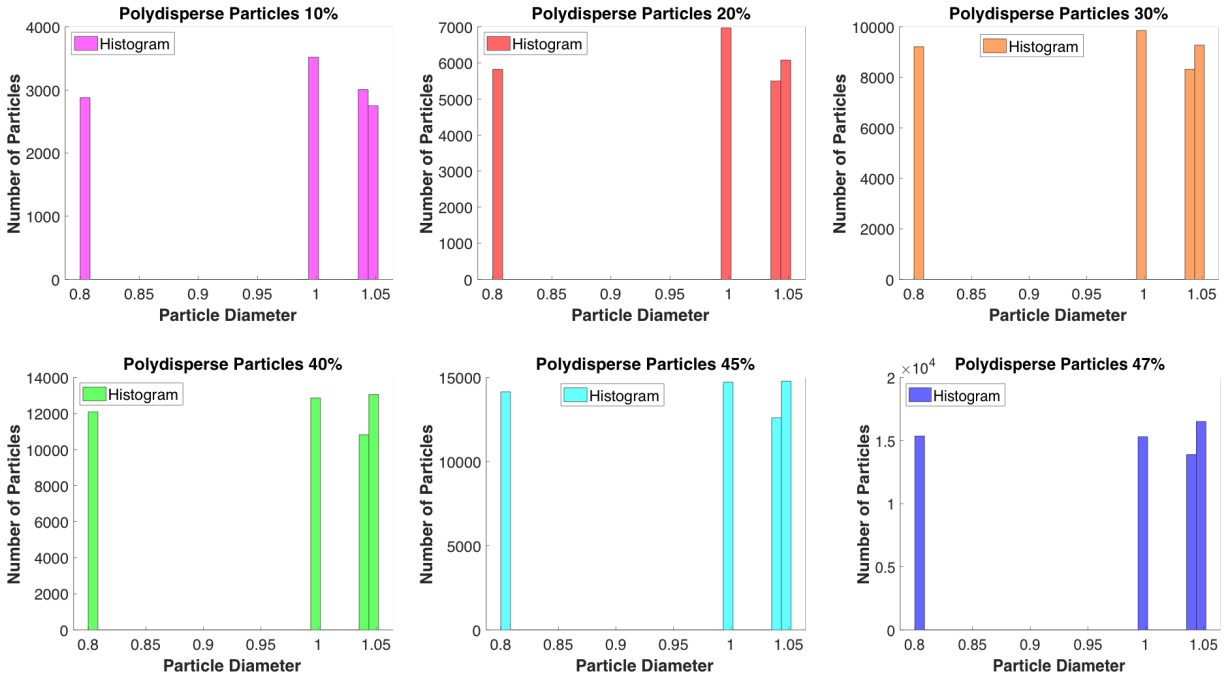

Figure 2.3: Particle size distribution of the slightly polydisperse particles.

directions until an appropriate size without size-dependence was achieved. It was determined that replicating the original system size four times in each direction eliminated system size effects. Once this configuration was replicated, the particles were then moved around using the random Brownian pair interaction in LAMMPS to make the particle arrangements random again. This step was not part of the dynamics but was simply to create a random placement of the particles after replicating the same arrangment of particles.

To create polydisperse particle systems, the monodisperse particle positions were used and the particle size was increased and decreased randomly on the monodisperse particles to add slight polydispersity to the particle sizes. Figure 2.3 shows the size distributions of the polydisperse particles. The system of polydisperse particles were then replicated and the positions randomized as described above.

2.4.3 Relative Viscosity/Viscosity Ratio

The relative viscosity or viscosity ratio was calculated with Equation (3.5.2.2). Simulations are run until an equilibrium is reached. The values of $\sum_i \sigma_{xy}$ are an average over the time period where the average stress is constant with time. The relative viscosity of monodisperse hard sphere particle suspensions as a function of volume fraction is shown in Figure 2.4. The values of (Ball and Melrose, 1997), the more accurate Stokesian Dynamics of (Bossis and Brady, 1984; Brady, 1988), and the FLD with truncated expressions of (Bybee, 2009) are shown in black. Ball and Melrose simulated hard sphere suspensions using just the squeeze term so only volume fractions as low as 20% could be simulated. The squeezing force dominates in close-range interactions but Ball and Melrose were able to simulate hard sphere suspensions at 20% and higher and the results compare well to higher accuracy simulation methods, such as Stokesian Dynamics (Bossis and Brady, 1984; Brady, 1988). To avoid particle overlaps, they utilize a smaller and smaller time step allowing particles to approach close to each other without overlap during the simulations, and so preserve the physics of the problem. Stokesian Dynamics should give the most accurate results but the computation time of Stokesian Dynamics limits the number of particles that can be used. To reduce computation time, the FLD method was then developed. The original FLD method implemented into the current distribution of LAMMPS includes truncated versions of Equations (2.3.5.2a), (2.3.5.2b), and (2.3.5.2c) to only include up to the first $\log$ term in each Equation. The truncated FLD pair interactions – that are the current implementation in LAMMPS (Original FLD) – resulted in higher values and match those reported in (Bybee, 2009). The relative viscosity calculated from simulations performed with the truncated resistance terms deviate from the results of Ball and Melrose and Stokesian Dynamics, especially at higher volume fractions. However, when we implemented the correct full expressions for the resistance terms into LAMMPS, the match between our results and Stokesian Dynamics was closer, even at the higher volume fractions.

Three different simulation box strain rates were tested to determine the influence of the shear rate. The same time step was used in all three cases. The same input configurations of particles was used

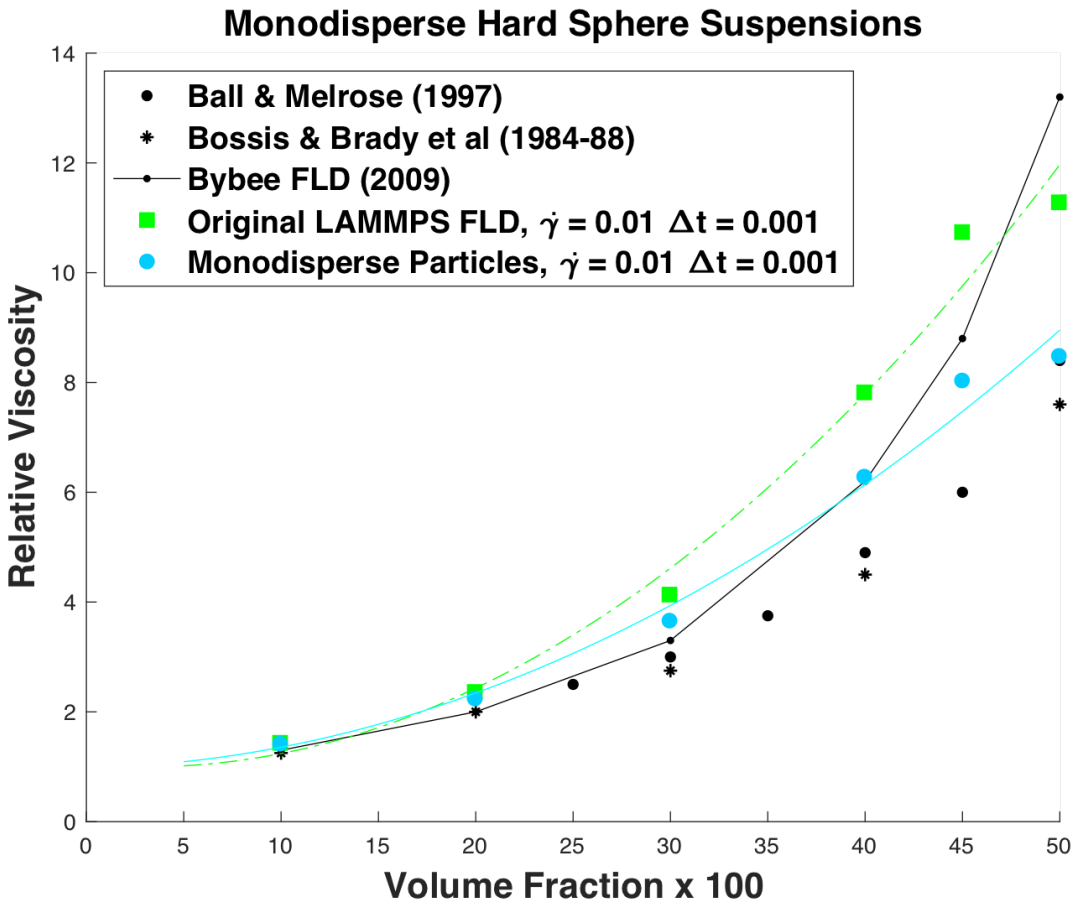

Figure 2.4: The results reported previously are shown in black. The results of the simulations reported here are shown in color. When we implemented the correct full expressions for the resistance terms into LAMMPS, the match between our results and those of Ball and Melrose (1997) and Brady and Bossis (1984) was closer, even at higher volume fractions, unlike Bybee (2009) and the original LAMMPS FLD implementation. The $-\cdot$ (Original FLD implementation in LAMMPS) and $-$ lines (Simulations with full correct expressions) are second order polynomial fits through the simulation data. Both simulation sets were run with the same initial particle data sets.

for all three simulation sets. The simulations run with $\dot{\gamma} \times \Delta t$ values of 1×10^{-5} and 1×10^{-6} were all run until the strain reached 200 for all volume fractions shown. Due to time limitations on the computing resource, the simulation sets run with $\dot{\gamma} \times \Delta t$ of 1×10^{-7} were only strained to a value of 20, which corresponds to the same length of simulation time as the $\dot{\gamma} \times \Delta t = 1 \times 10^{-6}$. However, the values of stress used to calculate the viscosity is an average of those values once the total stress have come to equilibrium, which occurs early on in the simulations. So even if the simulations

were not strained the same amount, the viscosity should not be affected in an appreciable way. The results show that the variation of shear rates did not significantly impact the relative viscosity for the cases tested and shown in Figure 2.5. In these simulations, we assume that the particles maintain their spherical shape. Elongation of the particles due to shearing can influence the viscosity. Particle surface properties also can impact the effects of shearing on the viscosity. In cement slurry systems, for example, the rheology is dependent on shearing and resting history. When cements are at rest, particles within the suspension can flocculate together due to random movements (Banfill, 2006; Guillot, 1990; Roussel, 2005). Shearing the suspension serves to break apart these particle clusters and is thought to lend to the shear thinning that occurs with time (Banfill, 2006; Guillot, 1990; Roussel, 2005). In the simulations shown herein, these properties are not included, which could be why the shear rates shown do not have an impact on the relative viscosity.

Figure 2.6 compares the relative viscosity of the monodisperse particles to the slightly polydisperse particles. To create the particle inputs of the polydisperse particle sets, the monodisperse particle inputs were used but random particle sizes were decreased to a diameter of 0.802 and other particle sizes were randomly increased to a diameter of either 1.0495 or 1.0396, and the remaining particles kept a diameter of 1.0. The change in the particle sizes from the monodisperse particles with a diameter of 1.0, was a slight change to explore the effects that the particle size distribution has on the particle suspension properties. For the simulations explored here, the relative viscosity was not significantly impacted by the polydispersity added. The stress per particle that is used to calculate the relative viscosity is a function of the force between the particle pairs and the distance between their centers. The difference in the particle sizes is considered in calculating the force (Equations 2.3.5.3) but there is not a lot of disparity in the particle sizes. The center to center distances between particles may also average out so that the same overall average stress that is calculated is not very different between the polydisperse and monodisperse particles.

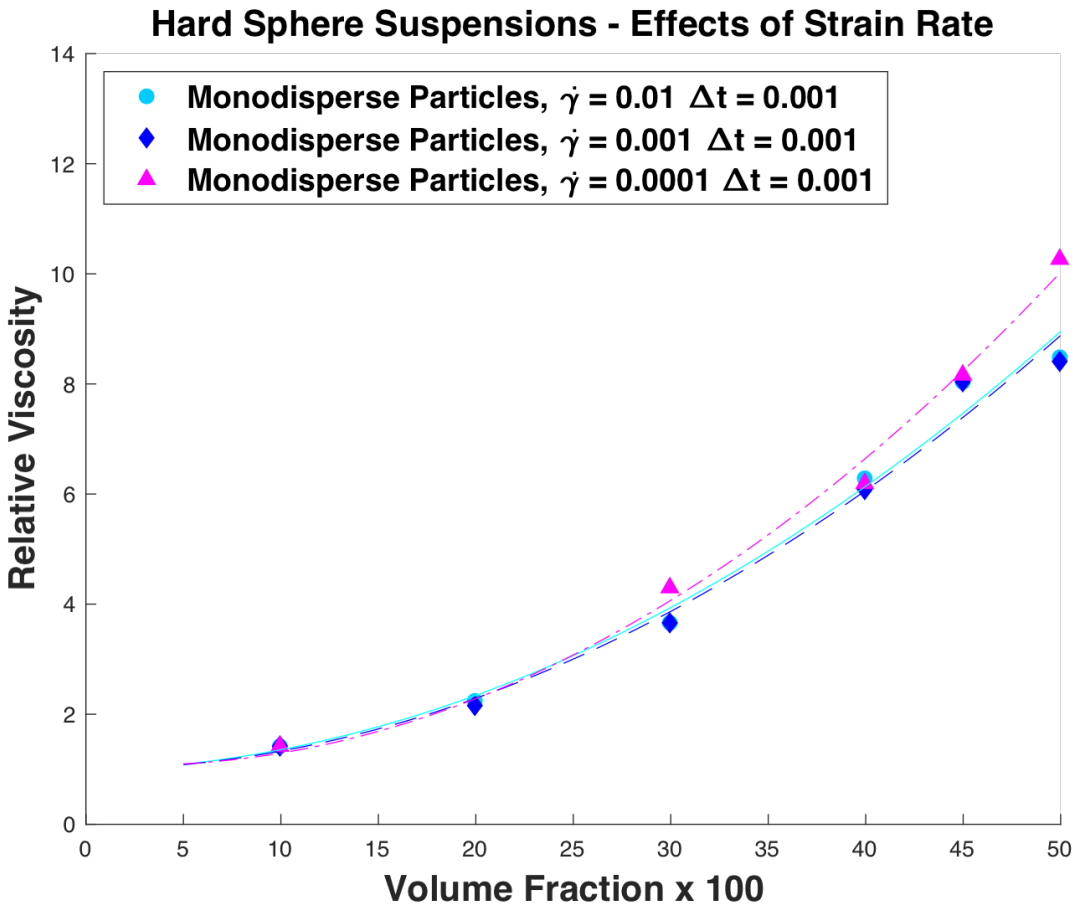

Figure 2.5: Results are shown for three different strain rates. The simulation sets were run with the same initial particle configurations.

2.4.4 Dependence of Structuring on Monodisperse vs. Polydisperse

To explore the effects of the particle volume fraction on particle rearrangement and structuring, the monodisperse particle placements from the 50% volume fraction, having a diameter of 1.0, was used to create lower volume fractions of particles by reducing the particle diameter of all particles. The volume fractions created correspond to 46%, 47%, and 48%, with diameters of 0.973, 0.980, and 0.99, respectively, to determine at what volume fraction the structuring is significant. Simulations of the monodisperse particles show structuring of the particles at a particle volume fraction of around 47% as shown in Figure 2.7. These results are consistent with (Ball and Melrose, 1997). A 48% volume fraction of particles had even more structuring. The relative levels of structuring

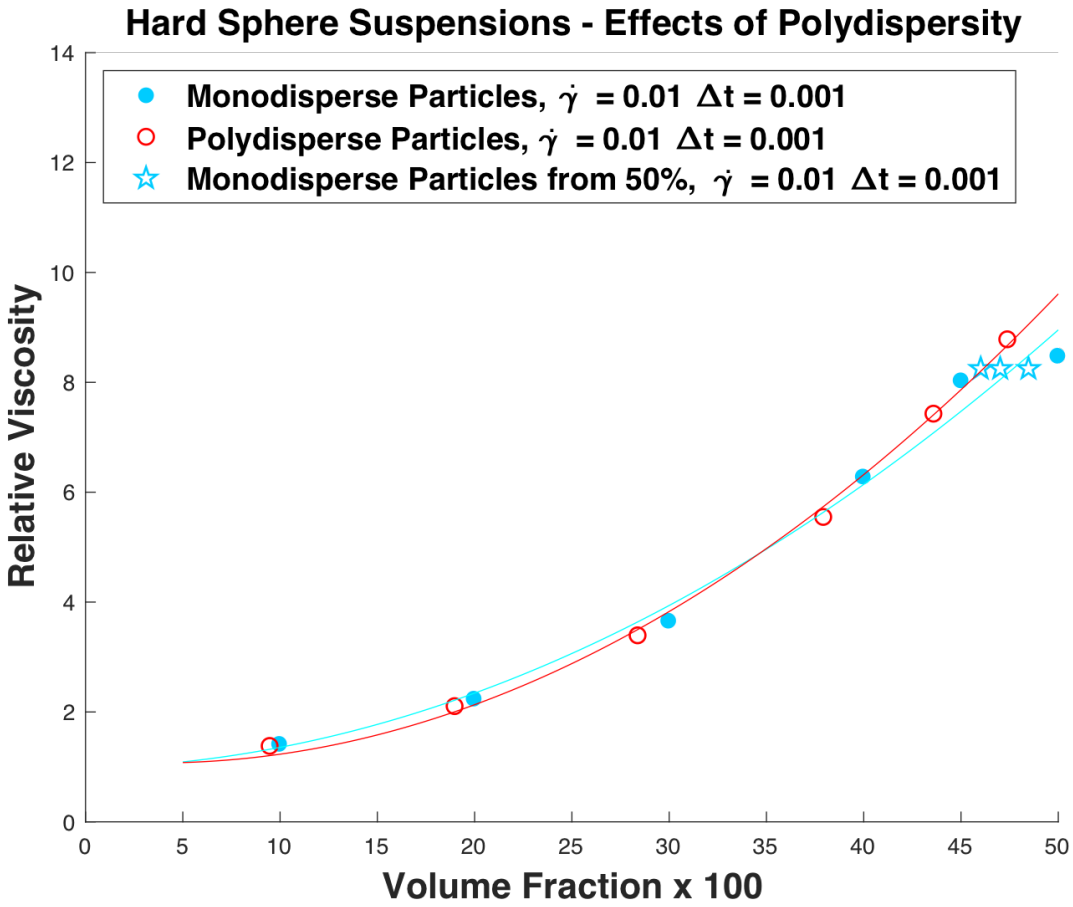

Figure 2.6: Results are shown for hard sphere suspensions of monodisperse (solid circles) and polydisperse (open circles) particles.

between these volume fractions can be seen in Figure 2.7 and Figure 2.8. Figure 2.7 shows the final particle configurations at the last timestep. All particles are shown in the figures and the perspective is a view from the side as indicated in Figure 3.9. The particles are shown at half their size so that the structures in the systems can be visualized. The colors of the particles show how many other particles are near by and are an indication of the particle structuring in a local region. The red particles show a higher coordination and level of structuring and the blue particles indicate no or little coordination with that particular particle's neighbors. In larger particle systems, the structuring may not be qualitatively or visually evident so the coordination number can be used to identify local regions of structuring. The coordination number is the sum of neighbors located within a dis-

tance of 1.5 from particle center. The coordination number for each particle was calculated using OVITO's[7] (Stukowski, 2010) computation of the coordination number and corresponding radial distribution function for each system of particles. Figure 2.8 shows the evolution of structuring over time. Three timesteps are shown in the figure for the initial and the final configurations and at the midpoint. The color corresponds to the level of coordination, where the red particles show a higher level of structuring and blue indicates less coordination. The radial distribution function is also shown for each time step and corresponds to the level of structuring of the whole system. The thinner, taller peak is indicative of more overall system structuring.

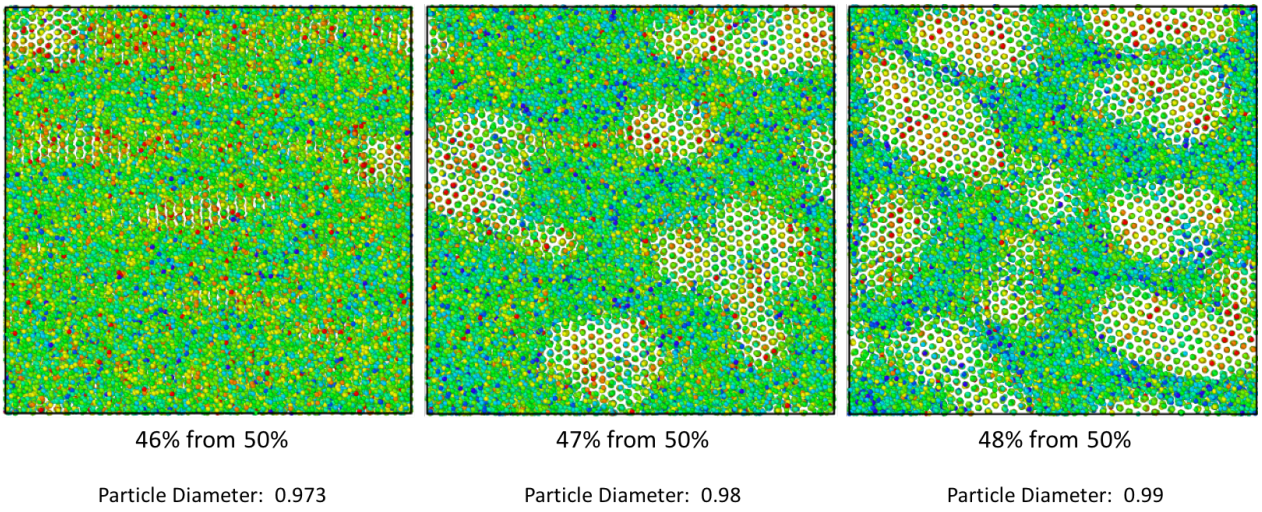

Figure 2.7: Comparison of structuring of monodisperse particles at three different volume fractions. The structuring is indicated by particles aligning along a single line and are seen as a single particle from the view point. The structuring increases with volume fraction. The particle configurations were made by reducing the monodisperse particle size from a 50% volume fraction of particles so that all particles are starting from the same configuration. The final configuration is shown. Particles are shown at half size.

By adding a small level of variation in the particle sizes to the same particle positions as the monodisperse particles, a comparison can be made between the monodisperse particles and the polydisperse. Because the monodisperse particles show structuring to begin and become noticeable at a volume fraction of 47%, a 47% volume fraction was used for comparison between the monodisperse and polydisperse particles. The polydisperse 47% by volume fraction of particles

[7] http://ovito.org/

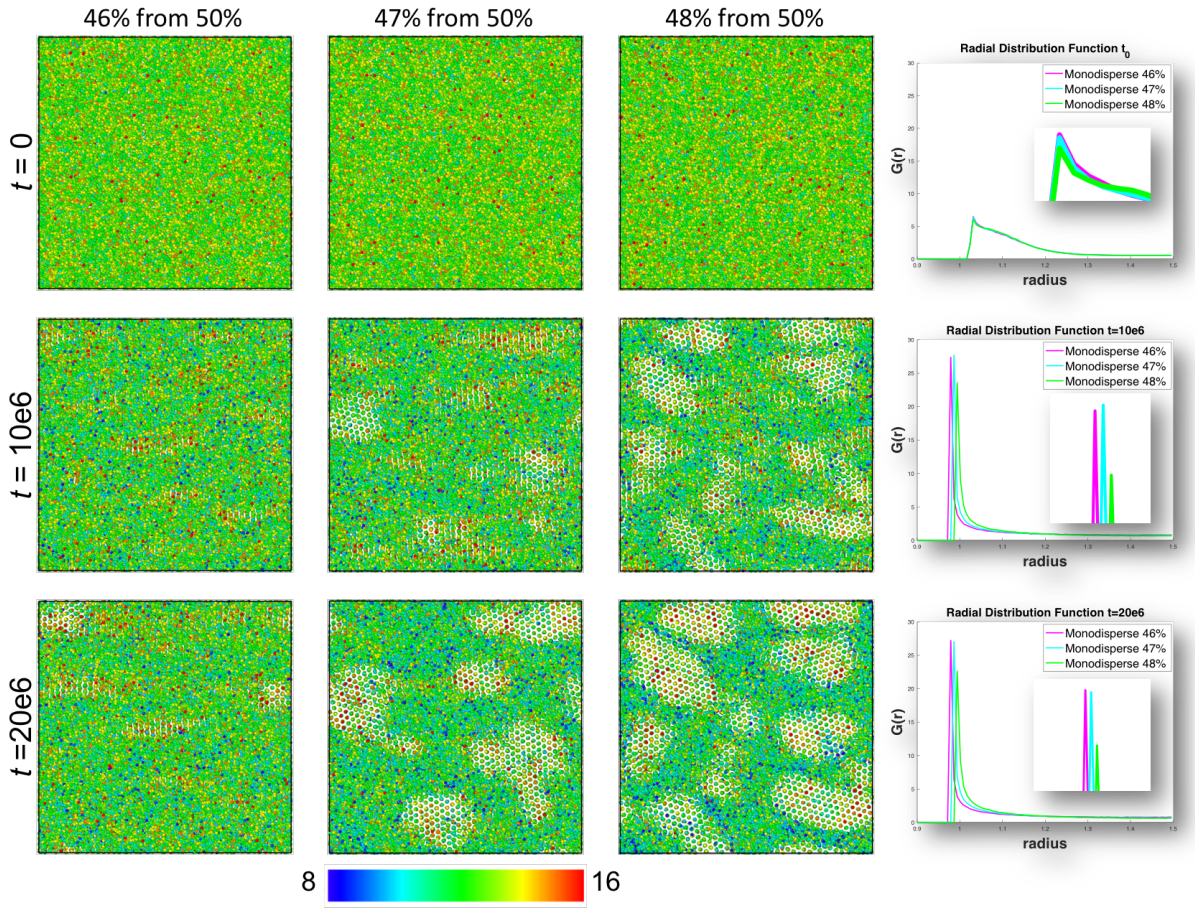

Figure 2.8: The Radial Distribution Function is shown at three different times, representing the initial configuration, the configuration at the mid-point and the configuration at the end of the simulation. The color corresponds to the particle coordination number. The side shown is the view indicated in figure 3.9.

system, did not show particle clustering or structuring after shearing. Figure 2.9 shows the three-dimensional simulation box and the particles at 47% by volume fraction of the monodisperse and polydisperse systems. The initial, random configuration of particles is shown with the final configuration at the end of the simulations. The direction of shear is indicated in the figure and particle alignment relative to the direction of shearing can be seen in the monodisperse system. The particles begin to align and form chains of particles. This can also be observed from the side view of the simulation box shown in Figure 2.10. From this perspective, the particles can be seen to align in a structured pattern similar to a crystal. One region of structuring is indicated with an ellipse. The particles are shown at half size in the inlaid image, where it is evident that the alignment extends

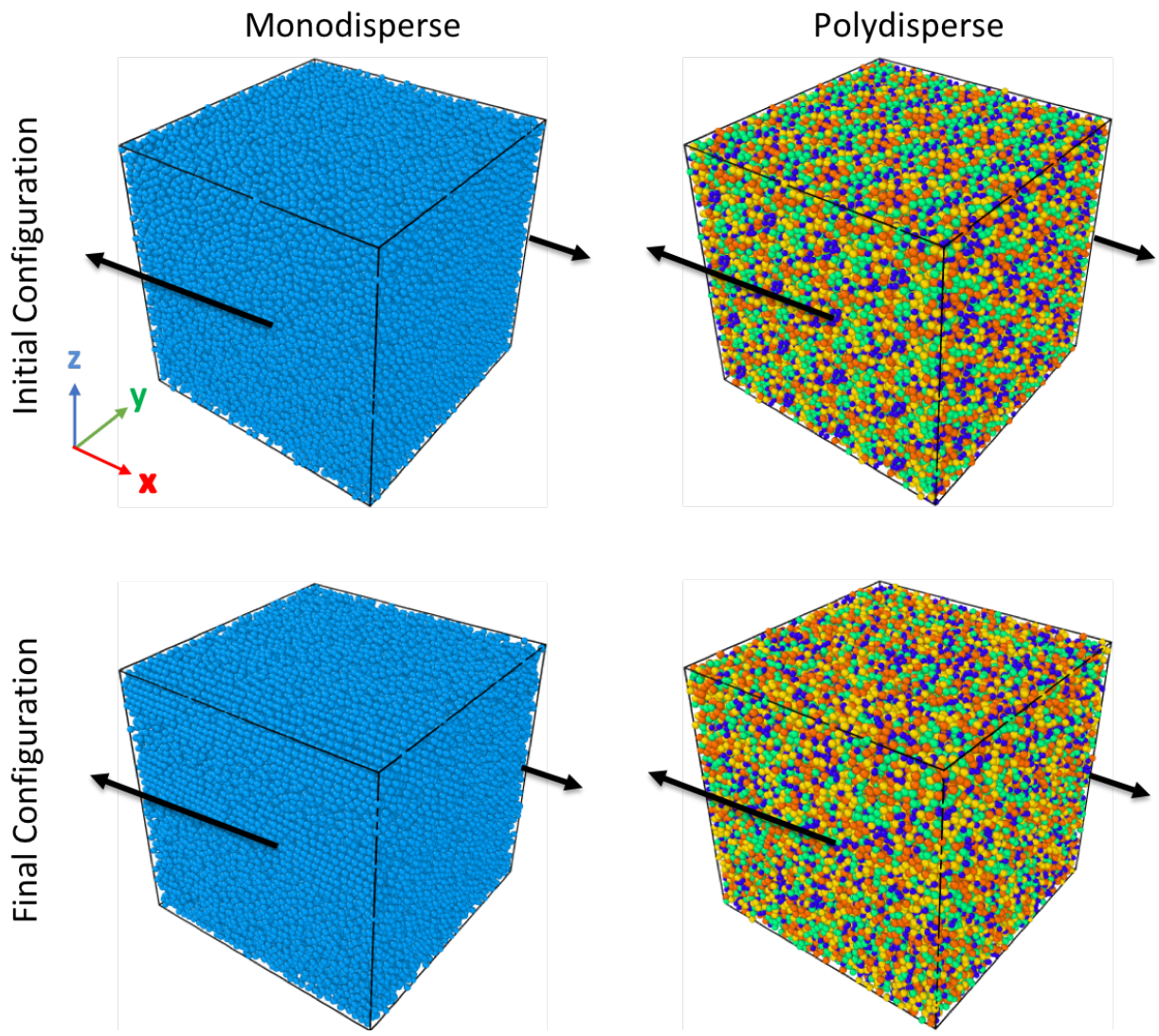

Figure 2.9: The initial and the final configurations of two 47% by volume fraction of particles systems. Monodisperse and polydisperse particle configurations are compared. The color corresponds to the particle size.

throughout the length of the simulation box. In contrast, the polydisperse particles remain in a random configuration after shearing to the same strain value. In Figures 2.9 and 2.10 the color is only indicative of the particle size to emphasize the level of polydispersity relative to the monodisperse particles. As discussed in the previous section, the slight polydispersity did not have an appreciable effect on the relative viscosity, but there is a clear difference in the propensity to form structuring under imposed shearing between the monodisperse and polydisperse particles.

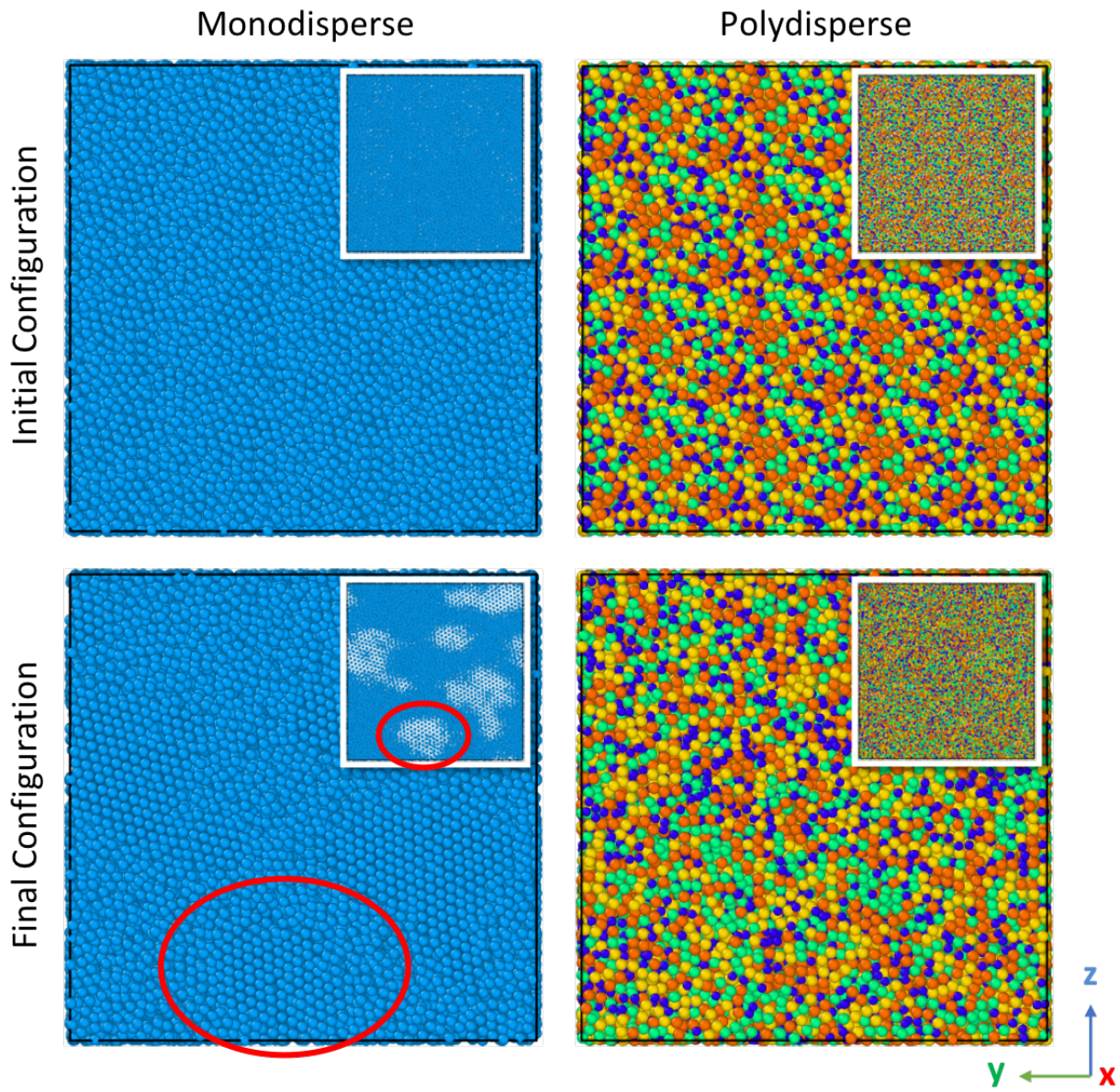

Figure 2.10: The initial and the final configurations of two 47% by volume fraction of particles systems. Monodisperse and polydisperse particle configurations are compared. The color corresponds to the particle size. The side shown is the view indicated in figure 3.9. The insert shows the particles at half size, where the structuring is more apparent. The circled region indicates one of the regions where structuring occurred in the particles. The particles form a line of particles in the x-direction.

2.5 Discussion

A key finding of this paper is that even a small amount of polydispersity in the particle size distribution reduces structuring of the particles during a shearing Couette flow. Real systems, including foamed cements, have natural polydispersity. The goal is to keep particles dispersed after the flow has started and it seems that the polydispersity helps to maintain the dispersion. We also find that the relative viscosity was minimally affected by adding the small amount of polydispersity. The effect of adding bubbles or particles to fluids is an increase in the viscosity, and therefore it is beneficial that the relative viscosity is not dependent on this level of polydispersity.

A key assumption that we have made here is that the fluid is Newtonian. This assumption is essential for the Stokesian Dynamics method. In essence, the Newtonian assumption leads – in the Stokes' flow limit – to a linear problem. The linearity enables the use of superposition techniques – using fundamental solutions such as Stokeslets – that are specific to linear problems.

Cement slurry, on the other hand, is well known to behave as a non-Newtonian fluid (Guillot, 1990; Roussel, 2005). However, there exists no method analogous to Stokesian Dynamics for the non-Newtonian setting since superposition cannot be used. Instead, one must solve, at a given time, the continuum mechanical balance of linear momentum[8]with a nonlinear constitutive response, $\boldsymbol{\sigma}(\boldsymbol{x}, t) = \hat{\boldsymbol{\sigma}}(\phi, \boldsymbol{E})$, and with a large number of bubbles / particles embedded in the solution domain. Further, one must compute – at every time – the net force on all the bubbles / particles, and move them appropriately. Then the balance of momentum equation must be solved again, and so on. This is clearly a completely unfeasible problem.

A potential alternate approach for the future is to use homogenization methods, e.g. (Avazmohammadi and Castañeda, 2016; Gao et al., 2011, 2012; Lipton and Avellaneda, 1990; Lipton and Vernescu, 1994) that have also been used to similar ends. While these have the important advantage that non-Newtonian systems can tractably be solved numerically, they do not track individual bub-

[8]Here, $\boldsymbol{\sigma}$ is the stress field and $\boldsymbol{v}$ is the velocity field.

bles / particles. Therefore, detailed insights into the structuring process cannot easily be resolved using these methods. An important goal for the future is to develop mixture theory-based models that include additional continuum scale fields (or internal variables) that track the structuring, possibly following ideas from (Christoffersen et al., 1981).

We have focused our attention here on Couette flows using the Lees-Edwards method. Future work will look at a more general class of flows that generalize the Lees-Edwards method (Dayal and James, 2010, 2012). Like the Lees-Edwards method, this general class of flows are also exact solutions of particle dynamics.

Ongoing experimental efforts have the ability to study the bubble sizes and their typical distribution of sizes in the well, by producing foamed cement samples and then using Computed Tomography scanning to quantify bubble sizes, their size distribution, and their initial distribution within the sample relative to other bubbles (Kutchko et al., 2013, 2015). Future work will continue to compare the particle dynamics simulations with experimental observations.

It would be very interesting to investigate higher volume fractions. However, it is difficult to create initial conditions of monodisperse particle systems of randomly placed particles above 50% volume fraction in the approach used here. The maximum packing fraction of ordered spheres is roughly $\sim 34\%$ to $\sim 74\%$ – depending on sphere packing pattern (Gauss, 1876) – and these packings are uniform. A random arrangement of sphere packing when compressed has a maximum packing fraction of $\sim 64\%$ (Song et al., 2008). Therefore, an initial condition with not too much polydispersity that approaches these volume fractions, tends to become more ordered. Our current efforts involve the use of methods to create lognormal particle size distributions of randomly placed particles that do not overlap, but there are a number of unsolved challenges in achieving this.

2.6 Chapter 2 References

Bibliography

(2003). *LAMMPS Users Manual*. Sandia National Laboratories.

American Petroleum Institute (2010). Isolating Potential Flow Zones During Well Construction - API Standard 65 Part 2.

Atkin, R. and Craine, R. (1976). Continuum theories of mixtures: basic theory and historical development. *The Quarterly Journal of Mechanics and Applied Mathematics*, 29(2):209–244.

Avazmohammadi, R. and Castañeda, P. P. (2016). Macroscopic rheological behavior of suspensions of soft solid particles in yield stress fluids. *Journal of Non-Newtonian Fluid Mechanics*, 234:139–161.

Ball, R. C. and Melrose, J. R. (1997). A simulation technique for many spheres in quasi-static motion under frame-invariant pair drag and Brownian forces. *Physica A: Statistical Mechanics and its Applications*, 247(1-4):444–472.

Banfill, P. F. G. (2006). Rheology of Fresh Cement and Concrete. *Rheology Reviews 2006*, 2006:61–130.

Bossis, G. and Brady, J. F. (1984). Dynamic simulations of sheared suspensions. {I.} General method. *J. Chem. Phys.*, 80(10):5141–5154.

Bowen, R. (1976). Theory of mixtures. In Eringen, A., editor, *Continuum physics (Vol. III)*, page 1. Waltham: Academic Press, New York.

Brady, J. (1988). Stokesian Dynamics. *Annual Review of Fluid Mechanics*, 20(1):111–157.

Bybee, M. D. (2009). *HYDRODYNAMIC SIMULATIONS OF COLLOIDAL GELS: MICROSTRUCTURE, DYNAMICS, AND RHEOLOGY*. PhD thesis, University of Illinois at Urbana-Champaign.

Christoffersen, J., Mehrabadi, M., and Nemat-Nasser, S. (1981). A micromechanical description of granular material behavior. *Journal of applied mechanics*, 48(2):339–344.

Clift, R. (1978). Bubbles. *Drops and Particles*.

Crowe, C., Sommerfeld, M., Tsuji, Y., et al. (1998). Multiphase flows with.

Dalton, L. E., Brown, S., Moore, J., Crandall, D., and Gill, M. (2018). Evolution Using CT Scanning : Insights From Elevated-Pressure Generation. (January):1–11.

Dayal, K. and James, R. D. (2010). Nonequilibrium molecular dynamics for bulk materials and nanostructures. *Journal of the Mechanics and Physics of Solids*, 58(2):145–163.

Dayal, K. and James, R. D. (2012). Design of viscometers corresponding to a universal molecular simulation method. *Journal of Fluid Mechanics*, 691:461–486.

de Rozieres, J. and Griffin, T. J. (1990). Chapter 14 Foamed Cements. In Nelson, E. B., editor, *Well Cementing*, pages 14.1 – 14.19. Schlumberger Educational Services, 300 Schlumberger Drive, Sugar Land, Texas 77478.

Eringen, A. C. (2007). *Nonlocal Continuum Field Theories*. Springer Science & Business Media.

Gao, T., Hu, H. H., and Castañeda, P. P. (2011). Rheology of a suspension of elastic particles in a viscous shear flow. *Journal of Fluid Mechanics*, 687:209–237.

Gao, T., Hu, H. H., and Castañeda, P. P. (2012). Shape dynamics and rheology of soft elastic particles in a shear flow. *Physical review letters*, 108(5):058302.

Gauss, C. F. (1876). Besprechung des buchs von la seeber: Untersuchungen uber die eigenschaften der positiven ternaren quadratischen formen usw. *Gottingensche Gelehrte Anzeigen*, 2:188–196.

Goldhirsch, I. (2003). Rapid granular flows. *Annual review of fluid mechanics*, 35(1):267–293.

Guillot, D. (1990). Rheology of Well Cement Slurries. *Developments in Petroleum Science*, 28(C):4–1–4–37.

Happel, J. and Brenner, H. (1973). Low reynolds number hydrodynamics, noordhoff int. *Publishing, Leyden, Netherland*, 235.

Herrmann, H. (1999). Statistical models for granular materials. *Physica A: Statistical Mechanics and its Applications*, 263(1-4):51–62.

Herrmann, H. and Luding, S. (1998). Modeling granular media on the computer. *Continuum Mechanics and Thermodynamics*, 10(4):189–231.

James, R. D. and Müller, S. (1994). Internal variables and fine-scale oscillations in micromagnetics. *Continuum Mechanics and Thermodynamics*, 6(4):291–336.

Jeffrey, D. J. and Onishi, Y. (1984). Calculation of the resistance and mobility functions for two unequal rigid spheres in low-Reynolds-number flow. *Journal of Fluid Mechanics*, 139(-1):261.

Kim, S. and Karrila, S. J. (2005). *Microhydrodynamics: Principles and Selected Applications*. Dover Publications, Inc., Mineola, NY, 2nd editio edition.

Kumar, A. (2010). *Microscale Dynamics in Suspensions of Non-Spherical Particles*. Doctor of philosophy, University of Illinois at Urbana-Champaign.

Kumar, A. and Higdon, J. J. L. (2010). Origins of the anomalous stress behavior in charged colloidal suspensions under shear. *Physical Review E - Statistical, Nonlinear, and Soft Matter Physics*, 82(September):1–7.

Kutchko, B., Crandall, D., Gill, M., McIntyre, D., Spaulding, R., Strazisar, B., Rosenbaum, E., Haljasmaa, I., Benge, G., Cunningham, E., DeBruijn, G., and Gardner, C. (2013). Computed Tomography and Statistical Analysis of Bubble Size Distributions in Atmospheric-Generated Foamed Cement. Technical Report August.

Kutchko, B., Crandall, D., Moore, J., Gill, M., McIntyre, D., Rosenbaum, E., Haljasmaa, I., Strazisar, B., Spaulding, R., Harbert, W., Benge, G., Cunningham, E., Lawrence, D. W., DeBruijn, G., and Gardner, C. (2015). Field-Generated Foamed Cement : Initial Collection , Computed Tomography , and Analysis. Technical Report July, U.S. Department of Energy, National Energy Technology Laboratory.

Lees, A. and Edwards, S. (1972). The computer study of transport processes under extreme conditions. *Journal of Physics C: Solid State Physics*, 5(15):1921.

Lipton, R. and Avellaneda, M. (1990). Darcy's law for slow viscous flow past a stationary array of bubbles. *Proceedings of the Royal Society of Edinburgh Section A: Mathematics*, 114(1-2):71–79.

Lipton, R. and Vernescu, B. (1994). Homogenisation of two-phase emulsions. *Proceedings of the Royal Society of Edinburgh Section A: Mathematics*, 124(6):1119–1134.

Loeffler, N. (1984). Foamed Cement: A Second Generation. In *Permian Basin Oil and Gas Recovery Conference*.

Marshall, J. and Dayal, K. (2014). Atomistic-to-continuum multiscale modeling with long-range electrostatic interactions in ionic solids. *Journal of the Mechanics and Physics of Solids*, 62:137–162.

Massoudi, M. (2002). On the importance of material frame-indifference and lift forces in multiphase flows. *Chemical Engineering Science*, 57(17):3687–3701.

Massoudi, M. (2003). Constitutive relations for the interaction force in multicomponent particulate flows. *International Journal of Non-Linear Mechanics*, 38(3):313–336.

Massoudi, M. (2008). A note on the meaning of mixture viscosity using the classical continuum theories of mixtures. *International Journal of Engineering Science*, 46(7):677–689.

Massoudi, M. (2010). A mixture theory formulation for hydraulic or pneumatic transport of solid particles. *International Journal of Engineering Science*, 48(11):1440–1461.

Maxey, M. R. and Riley, J. J. (1983). Equation of motion for a small rigid sphere in a nonuniform flow. *The Physics of Fluids*, 26(4):883–889.

NETL (2019). Tbd. Internal Research to be published.

Plimpton, S. (1995). Fast Parallel Algorithms for Short Range Molecular Dynamics. *Journal of Computational Physics*, 117(June 1994):1–19.

Pugh, R. J. (1996). Foaming, foam films, antifoaming and defoaming. *Advances in Colloid and Interface Science*, 64(95):67–142.

Rahimian, A., Veerapaneni, S. K., Zorin, D., and Biros, G. (2015). Boundary integral method for the flow of vesicles with viscosity contrast in three dimensions. *Journal of Computational Physics*, 298:766–786.

Rajagopal, K. R. and Tao, L. (1995). *Mechanics of mixtures*, volume 35. World scientific.

Roussel, N. (2005). Steady and transient flow behaviour of fresh cement pastes. *Cement and Concrete Research*, 35:1656–1664.

Sadhal, S., Ayyaswamy, P., and Chung, J. (1997). Transport phenomena with bubbles and drops.

Sangani, A. and Acrivos, A. (1983). The effective conductivity of a periodic array of spheres. *Proc. R. Soc. Lond. A*, 386(1791):263–275.

Song, C., Wang, P., and Makse, H. A. (2008). A phase diagram for jammed matter. *Nature*, 453(7195):629.

Soo, S.-l. (1967). Fluid dynamics of multiphase systems. *WALTHAM, MASS, BLAISDELL PUBLISHING CO, 1967. 524 P, 206 FIG, 8 TAB, 886 REF.*

Stukowski, A. (2010). Visualization and analysis of atomistic simulation data with OVITOthe Open Visualization Tool. *Modelling and Simulation in Materials Science and Engineering*, 18(1):15012.

Tadmor, E. B. and Miller, R. E. (2011). *Modeling materials: continuum, atomistic and multiscale techniques*. Cambridge University Press.

Tan, L., Ye, G., Schlangen, E., and Van Breugel, K. (2007a). Coupling of hydration and fracture models: Failure mechanisms in hydrating cement particle systems. *Particle and Continuum Aspects of Mesomechanics*, pages 563–571.

Tan, L. K., Schlangen, E., and Ye, G. (2007b). Simulation of failure in hydrating cement particles systems. 348:737–740.

Tchen, C. (1947). Mean value and correlation problems connected with the motion of small particles suspended in a turbulent fluid.

Truesdell, C. (1984). Rational thermodynamics.

Wallis, G. B. (1969). One-dimensional two-phase flow.

Walton, i. O. and Braun, R. (1986). Stress calculations for assemblies of inelastic speres in uniform shear. *Acta mechanica*, 63(1-4):73–86.

Wu, W.-T., Aubry, N., Antaki, J. F., McKoy, M. L., and Massoudi, M. (2017). Heat transfer in a drilling fluid with geothermal applications. *Energies*, 10(9):1349.

Xiao, Y. (2005). *The influence of oxygen vacancies on domain patterns in ferroelectric perovskites*. PhD thesis, California Institute of Technology.

Chapter 3

Surfactant Stabilized Bubbles Flowing in a Newtonian Fluid[1]

3.1 Abstract

Bubbles suspended in a fluid cause the suspension to have different rheological properties than the base fluid. Generally, the viscosity of the suspension increases as the volume fraction of the bubbles is increased. A current application, and motivation for this study, is in wellbore cements used for hydrocarbon extraction and carbon sequestration. In these settings, the gas bubbles are dispersed into the cement to reduce the density as well as improve the properties for specific conditions or wellbore issues. In this paper, we use Stokesian dynamics to numerically simulate the behavior of a large number of bubbles suspended in a Newtonian fluid. Going beyond prior work on simulating particles in suspension, we account for the nature of bubbles by allowing for slip on the bubble surface, the deflection on the bubble surface, and a bubble-bubble pairwise interaction that represents the surfactant physics; we do not account for bubble compressibility. We incorporate these interac-

[1]This paper has been accepted for publication and is in press with the Mathematics and Mechanics of Solids Journal. Reference: Rosenbaum, E., Massoudi, M., & Dayal, K., Surfactant Stabilized Bubbles Flowing in a Newtonian Fluid, Mathematics and Mechanics of Solids, 2019.

tions and simulate bubble suspensions of monodisperse size at several volume fractions. We find that the bubbles remain better dispersed compared to hard spherical particles that show a greater tendency to structure or cluster.

3.2 Introduction

The motivation for this study is to better understand the rheology of well cement that has been foamed with an inert gas. Foaming the cement lowers the density, and is used in wells drilled into weak or fractured rock formations (Loeffler, 1984). Foamed cement is created by dispersing gas, typically nitrogen, into the cement slurry to create a suspension, which contains suspended cement particles, and dispersed bubbles. To ensure a stable foam that keeps the bubbles entrained, surfactants and sometimes other additives are included in the slurry base prior to injecting the gas to form the bubbles. In the wellbore, cement is placed between the steel casing at the center of the well and the rock formation to isolate and seal wells in carbon storage and hydrocarbon extraction. It also supports the casing placed in the center of the well. The process of foaming the cement slurry lowers the density of the cement as required for the conditions of the wellbore. Foaming the cement is advantageous because it lowers the density and increases the viscosity of the cement, while not significantly lowering the compressive strength nor changing the cement chemistry. To maintain isolation of the well, however, the bubbles should remain suspended in the cement and maintain dispersion. Structuring or clustering can lead to weak mechanical regions for crack propagation or pathways for gas migration.

Cement slurry is a highly complex material with properties that change over time due to the curing process. The cement slurry (base fluid) is made from water that is mixed with the cement clinker, a powdery mix of materials with primarily lime, silica, alumina, and iron. Upon mixing with water, the chemical reaction processes begin in the form of a hydration process (de Rozieres and Griffin, 1990). During the hydration process the chemical and the physical properties of the cement slurry

are changing. However, the cement does have a period when little hydration occurs and this is when the cement is placed in the wellbore. During this *induction* period, the slurry properties remain fairly constant and the effect of chemical reactions can be neglected. The behavior is dominated by fluid mechanics. A key focus of this paper is the effect of the flow on the overall ordering of the bubbles that are added through foaming. There is a vast literature on the effective properties of suspensions, e.g. going back to Taylor, 1932 (Taylor, 1932); for more information see (Massoudi, 2008). There is much less work on the structuring of the suspended bubbles.

The bubbles' distribution within the cement play a key role in the properties of the cement slurry (de Rozières and Ferrière, 1991). The foam should have well-dispersed bubbles, that remain in the suspension during placement without clustering, coalescing, or other configurations where the bubbles are arranged closely together (Loeffler, 1984). If the bubbles are close to each other, upon curing the bubbles can become interconnected and lead to failure of zonal isolation or even fracture of the cement (Tan et al., 2007a,b). The American Petroleum Institute (API) recommended practices prescribes that the foamed cement slurries be designed to have an added gas volume fraction below 35% at the placement depth of the cement for the foam to remain stable and maintain the mechanical integrity for proper zonal isolation (American Petroleum Institute, 2010). Pressures vary throughout the cement process due to different depths in the well; we, therefore, study a range of volume fractions (10% to 50%).

In (Rosenbaum et al., 2019), we studied the influence of the bubbles represented as hard no-slip spheres using the framework of Stokesian Dynamics (Brady, 1988) in the more efficient Fast Lubrication Dynamics (FLD) approximation (Bybee, 2009; Kumar, 2010; Kumar and Higdon, 2010). This method enables us to track the location of all the suspended objects during the simulation, and thereby obtain insights into smaller scale phenomena such as the detailed spatial distribution. An important assumption that is required for Stokesian Dynamics is that the base fluid is Newtonian. Our aim in this paper is to develop better representations of the bubbles while working within this overall framework to include far- and near-range bubble interactions. In particular, we account for

the nature of bubbles by allowing for slip on the bubble surface, the deflection on the bubble surface at the region where bubble pairs interact, and a bubble-bubble pairwise interaction that represents the surfactant physics, which can be attractive or repulsive in nature (Tabakova and Danov, 2009). For simplicity, in this paper *particles* shall refer to hard spherical particles that have no-slip boundary conditions on their surface; and *bubbles* shall refer to fluid-filled spheres with surface properties that allow slip and surface deflection in the interacting region, and a repulsive/attractive quality to represent the surfactant properties, but however are not compressible.

The paper is organized as follows: in Section 3.3, we outline our assumptions and briefly describe the well-established Stokesian Dynamics framework and the FLD approximation; in Section 3.4, we provide the details of the bubble interaction modeling; in Section 3.5, we describe the molecular dynamics simulation method; in Section 3.6, we present the results of the numerical calculations on the relative viscosity of the bubble suspension; and in Section 3.7, we present the results of the numerical calculations comparing bubble suspensions to the rigid no-slip particle suspensions studied in (Rosenbaum et al., 2019) and examine several volume fractions with monodisperse size distributions.

3.3 Model Assumptions and the Stokesian Dynamics Method

3.3.1 Model Assumptions

We make several assumptions about the bubbles and the system of interest.

The bubbles are assumed to be spherical and discrete. Surfactants are an essential part of the cement slurry design and the surfactant provides stability to the bubbles so that they remain suspended in the cement until is sets (de Rozières and Ferrière, 1991). Bubbles stabilized by surfactants have a high surface tension and maintain a relatively spherical shape. It is assumed that the bubbles have and maintain a spherical shape during flow and are not distorted or become ellipsoid-like during

shearing. Foamed cements made in the laboratory to the API testing standards and foamed under pressure show that the surfactants and stabilizers added to the base fluid maintain fairly spherical, stable, discrete bubbles in the flow regime typically encountered in the well (Dalton et al., 2018; Kutchko et al., 2013). However, the bubble surface is allowed to deflect locally on the surface a small amount in the region directly interacting with neighboring bubbles.

The bubbles are considered to be neutrally buoyant. In an aqueous solution, bubbles will rise due to buoyancy. However, in a stable foamed cement slurry, bubbles in cement tend to remain in place unless they reach a critical size (Dalton et al., 2018). This has been observed experimentally (Dalton et al., 2018; Kutchko et al., 2013, 2015): in laboratory and field applications, the bubble sizes are kept below this critical size (typically around $10 - 100\ \mu m$) and were observed to remain where placed during curing (Dalton et al., 2018). In addition, the cement particles in the slurry, which act as surface active foaming materials, help keep the bubbles entrained (Pugh, 1996).

The suspending fluid (cement slurry) is considered Newtonian. The cement slurry has cement particles suspended in it, and therefore it is generally observed that cement slurry has a yield stress and can behave as a nonlinear fluid (Guillot, 1990; Roussel, 2005), or even behave as a solid (Beltempo et al., 2018). However, it would not be feasible to numerically simulate a non-Newtonian suspension that tracks individual bubbles. We therefore expect that the simulation results reported here will have qualitative and quantitative differences compared to experiments. Even so, these simulations can provide useful insights into the overall features that dictate the behavior of the real system, specifically the clustering of bubbles or rearrangement into more ordered placements which can potentially lead to bubble coalescence or bubble inter-connectivity upon cement curing. For simulations involving one or a small number of bubbles, sophisticated nonlinear models of the suspending medium can be applied (Gaudron et al., 2015). However, for a large number of suspended objects as is our interest here, the methods depend in an essential way on the superposition principle and hence require linearity.

3.3.2 Stokesian Dynamics

In a suspension, the motion of each suspended object (particles or bubbles) is transmitted through the base fluid. In the quasi-static (creeping flow) limit, this is felt immediately throughout the entire system by all the other suspended objects. Therefore long-range effects should be carefully considered. For a dilute suspension where the suspended objects are far apart, the detailed shape and structure of the suspended objects does not matter to leading-order. The velocity disturbance of a suspended object decays like a point force as $1/r^2$, where r is the radial distance from the object (Brady, 1988). When the suspended objects are close together, the interaction of each pair is dominated by a pairwise force which comes from lubrication theory (Kim and Karrila, 2005). The Stokesian Dynamics method accounts for the far-field interaction through multipole expansions and for the near-field interactions through pairwise interactions (Brady, 1988). The Fast Lubrication Dynamics (FLD) method further increases the efficiency by using fast approximate methods for the far-field interaction (Bybee, 2009; Kumar, 2010). The broader idea of developing multiscale methods for long-range interactions by decomposing into far- and near- fields and then using multipole expansions for the far-field has been studied theoretically and numerically in the context of bubbly fluids (Sangani and Acrivos, 1983) and electromagnetic interactions (James and Müller, 1994; Marshall and Dayal, 2014; Xiao, 2005).

For the flow of a Newtonian fluid when the inertial term is neglected in the balance of linear momentum, we can obtain the Stokes flow regime. The governing equation is a linear biharmonic equation, thereby allowing superposition. Given a flow with multiple objects, the flow due to each is given by a fundamental solution denoted by a Stokeslet, and the interaction between them can be obtained by superposing appropriately the Stokeslets solutions. This enables an *effective* pairwise interaction where the influence of the mediating fluid is accounted through the Stokeslet. Bossis and Brady were the first to develop this idea and put this into the framework of pairwise molecular dynamics to enable the efficient simulation of suspensions (Bossis and Brady, 1984; Brady, 1988). This method is denoted “Stokesian Dynamics”.

Consider a general macroscopically-uniform flow $\boldsymbol{v}(\boldsymbol{x}) = \boldsymbol{A}\cdot\boldsymbol{x}+\boldsymbol{B}$, where $\boldsymbol{x}$ is the spatial location. The symmetric rate-of-strain tensor is defined $\boldsymbol{E}^{\infty} := \frac{1}{2}(\boldsymbol{A}+\boldsymbol{A}^T)$, where $\boldsymbol{A}$ is the velocity gradient. The spin tensor is defined by $\boldsymbol{W} := \frac{1}{2}(\boldsymbol{A} - \boldsymbol{A}^T)$ and the corresponding axial vector is $\boldsymbol{w}$. The generalized far-field velocity $\boldsymbol{U}^{\infty}$ is defined by $\boldsymbol{B}$ and $\boldsymbol{w}$. The forces can be determined by the relationship between the object velocities and the forces due to the base fluid by:

$$\begin{pmatrix} \boldsymbol{F}^H \\ \boldsymbol{S}^H \end{pmatrix} = \mathcal{R} \cdot \begin{pmatrix} \boldsymbol{U}^{\infty} - \boldsymbol{U} \\ \boldsymbol{E}^{\infty} \end{pmatrix} \tag{3.3.2.1}$$

The symmetric first moment of the force, $\boldsymbol{S}^H$, is called the Stresslet. $\mathcal{R}$ is the resistance matrix, and contains the object positions. The main outcome of Stokesian Dynamics is to efficiently compute $\mathcal{R}$ so that large numbers of objects in a suspension can be simulated. This is described in numerous sources in the literature cited in this manusript, and therefore, we do not go into the details here.

Stokesian Dynamics preserves all the relevant physics of the problem but is computationally intense for systems with a large number of suspended objects. To allow for larger systems while still maintaining the physics of the problem in accounting properly for far-field and near-field interactions, *Fast Lubrication Dynamics* (FLD) was developed (Bybee, 2009; Kumar, 2010).

FLD (Bybee, 2009; Kumar, 2010) explicitly incorporates the lubrication interactions, following (Ball and Melrose, 1997), but modifies the Stokesian Dynamics (Brady, 1988) to reduce the computation time. In FLD, the resistance matrix, denoted $\mathcal{R}_{FLD}$, is the sum of the near-field pairwise lubrication interactions and the far-field interactions from the diagonal components of an isotropic resistance tensor, $\mathcal{R}_{Iso}$. $\mathcal{R}_{Iso}$ is assumed to be a multiple of the identity matrix. The multiplicative factor is assumed to be a function of the volume fraction, and is obtained by curve-fitting the short-time self-diffusivity results from FLD to those obtained from full Stokesian Dynamics. In this way, FLD aims to preserve the physics of the accurate Stokesian Dynamics approach while making the computation more efficient. The lubrication terms come from (Ball and Melrose, 1997; Jeffrey and Onishi, 1984; Kim and Karrila, 2005).

We note an issue regarding the implementation of FLD in the molecular dynamics code LAMMPS. (Ball and Melrose, 1997) give the expressions for the lubrication forces and torques of each suspended object in the pair interaction. However, LAMMPS uses truncated expressions that leave out some terms. FLD in LAMMPS has typically been applied in combination with other forces such as Brownian, colloidal, electrostatic, and so on. The error due to the missing terms can be negligible if other interactions dominate. However, for the calculations here, we find that it is important to use the longer expressions, and therefore we have corrected LAMMPS.

3.4 Bubble Interaction Modeling

Our approach is to simulate fluid-filled spheres of the same diameter with bubble surface properties and an elastic-like quality. For the purposes of this study, we consider that the bubbles have hydrodynamic interactions and some interaction due to the properties of a surfactant to keep bubbles from overlapping in the simulation. The attractive and repulsive qualities of the surfactant are also considered with this interaction. The bubbles' surfaces are allowed to deform locally in an elastic way when approaching very close to each other (see Figure 3.5), and then the bubble surface shape is restored when the gap between the bubble pair increases, so that the spherical bubble shape is maintained during the simulation.

The hydrodynamic interaction for a pair of bubbles, with the same size diameter, has been derived by (Kim and Karrila, 2005) for the case of two bubbles of the same size approaching each other. The interaction due to the surfactant and elastic properties are determined and added here. For approaching hard spheres with no slip on the particle surface, the force between the particles goes as the inverse of the gap between them, so that as the particles approach each other, the force increases so much so that the particles will not touch in finite time. The force on approaching bubbles is weaker and will allow bubbles to touch in finite time. In simulations, without an additional direct force, bubble overlap will occur. However, the surfactant of real bubbles will provide an extra force

that resists bubble coalescence. The force between the bubbles should be such that it does not allow bubbles to overlap but does allow them to approach very close to each other.

Bubbles have a mobile interface and, in theory, can have any level of slip and no shear traction on their surface boundaries. In a shearing interaction between bubble pairs, the bubbles should just slip past each other (Bechinger et al., 2013; Kim and Karrila, 2005). To simulate surfactant stabilized bubbles, we need to have a mobile surface boundary and an additional realistic normal direct force to prevent bubble overlap as the surfactant does in real bubble suspensions.

Bubble surface properties more representative of real bubbles stabilized by a surfactant has been developed here as an extension to the current capabilities of LAMMPS pair interactions.

3.4.1 Summary of Near-Field Lubrication Interactions for Particles

We briefly summarize the near-field interactions between particles to later compare to bubble interactions.

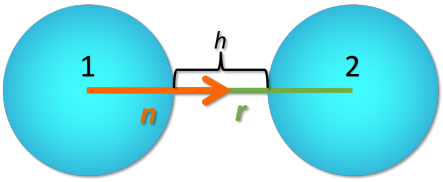

Figure 3.1: Two particles are separated by a center-to-center vector, $\boldsymbol{r}$, and $\boldsymbol{n} := \boldsymbol{r}/|\boldsymbol{r}|$. The gap between the particles is h.

Following Fig. 3.1, we consider a pair of particles 1 and 2, with equal radius, a, and a separation h between the particle surfaces. The expressions for the lubrication forces $\boldsymbol{f}_i$ and torques $\boldsymbol{g}_i$ on the

particles $i = 1, 2$ follows (Ball and Melrose, 1997):

$$\boldsymbol{f}_1 = -\boldsymbol{f}_2 = -a_{sq}\mathbb{N}\cdot(\boldsymbol{v}_1 - \boldsymbol{v}_2) - a_{sh}\left(\frac{2}{r}\right)^2 \mathbb{P}\cdot(\boldsymbol{v}_1 - \boldsymbol{v}_2) + \left(\frac{2}{r}\right) a_{sh}\boldsymbol{n}\times\mathbb{P}\cdot(\boldsymbol{\omega}_1 + \boldsymbol{\omega}_2) \tag{3.4.1.1a}$$

$$\boldsymbol{g}_1 = -\left(\frac{2}{r}\right) a_{sh}\boldsymbol{n}\times\mathbb{P}\cdot(\boldsymbol{v}_1 - \boldsymbol{v}_2) - a_{sh}\mathbb{P}\cdot(\boldsymbol{\omega}_1 + \boldsymbol{\omega}_2) - a_{pu}\mathbb{P}\cdot(\boldsymbol{\omega}_1 - \boldsymbol{\omega}_2) - a_{tw}\mathbb{N}\cdot(\boldsymbol{\omega}_1 - \boldsymbol{\omega}_2) \tag{3.4.1.1b}$$

$$\boldsymbol{g}_2 = -\left(\frac{2}{r}\right) a_{sh}\boldsymbol{n}\times\mathbb{P}\cdot(\boldsymbol{v}_1 - \boldsymbol{v}_2) - a_{sh}\mathbb{P}\cdot(\boldsymbol{\omega}_1 + \boldsymbol{\omega}_2) + a_{pu}\mathbb{P}\cdot(\boldsymbol{\omega}_1 - \boldsymbol{\omega}_2) + a_{tw}\mathbb{N}\cdot(\boldsymbol{\omega}_1 - \boldsymbol{\omega}_2) \tag{3.4.1.1c}$$

$\boldsymbol{n}$ is the unit vector directed along the line connecting the center of particle 1 pointing toward particle 2, $\mathbb{N} := \boldsymbol{n}\otimes\boldsymbol{n}$, and $\mathbb{P} := \boldsymbol{I} - \mathbb{N}$. $\boldsymbol{v}$ and $\boldsymbol{\omega}$ are the velocity and the angular velocity, respectively, of the particles. The forces $\boldsymbol{f}$ and torques $\boldsymbol{g}$ in (3.4.1.1) correspond to the generalized force and are linearly related to $\boldsymbol{v}$ and $\boldsymbol{\omega}$, and these latter quantities in turn correspond to the generalized velocity $\boldsymbol{U}$. The linear resistance terms for hard spheres of differnt sizes with no-slip surfaces, a_{sq}, a_{sh}, a_{pu}, and a_{tw}, are defined in (Rosenbaum et al., 2019).

For bubbles, there is a squeezing resistance, a_{sq}, but it is assumed that there are no shearing resistances (i.e. $a_{sh} = 0$ and $a_{pu} = 0$). The hydrodynamic forces for a bubble are still linearly related to the velocity and the force is calculated in a similar way as the lubrication solution for hard sphere(Rosenbaum et al., 2019) (Equations (3.4.1.1)). The force between bubbles includes additional forces to account for the elastic nature of a bubble and the forces due to the surfactant.

3.4.2 Near-Field Bubble Interactions: Interaction Force Between Approaching Bubbles

The interaction force between approaching hard spheres with no-slip surfaces is sufficient to keep the particles from touching in finite time. But for two approaching bubbles, they will touch in

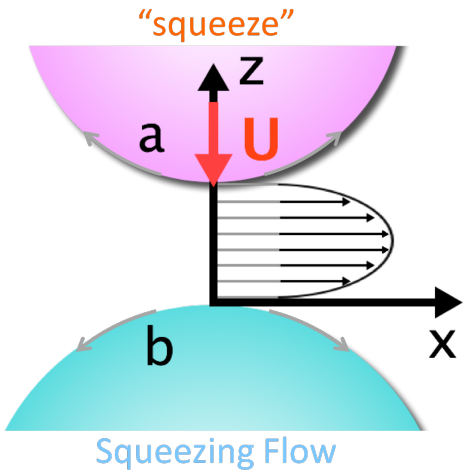

Figure 3.2: The surface of bubbles have slip and therefore the velocity profile contains an additional slip velocity (shown in gray).

finite time and can overlap. Figure 3.4 compares the gap as a function of time for particles and bubbles, without accounting for surface deflection of the latter. The velocity profile of a Newtonian fluid being squeezed from between the hard spheres has a parabolic shape. However, a bubble surface boundary has an extra slip velocity as depicted in Figure 3.2. The velocity profile of the fluid between the interacting bubbles is the sum of the parabolic velocity, u_p, and the additional slip velocity, u_t, due to the bubble surface (Davis et al., 1989; Kim and Karrila, 2005):

$$v(x,z) = u_t(x) + u_p(x,z) \tag{3.4.2.1}$$

The parabolic velocity profile of the fluid that is squeezed out from between hard spheres with no-slip boundaries is given by the expression (Kim and Karrila, 2005):

$$u_p(x,z) = \frac{1}{2\mu}\frac{\partial p}{\partial x}(z - z_a)(z - z_b) \tag{3.4.2.2}$$

Where z_a and z_b are the surfaces of the two spheres a and b, respectively, μ is the viscosity of the base fluid, and $\frac{\partial p}{\partial x}$ is the pressure gradient in the x direction. When the distance between the bubble surfaces is small compared to the bubble radii, the surfaces can be approximated as flat disks and

the surface traction is then given by (Kim and Karrila, 2005):

$$f_t = -(z_a - z_b)\frac{\partial p}{\partial x} \tag{3.4.2.3}$$

If μ is the viscosity of the base fluid, then by convention $\lambda\mu$ is defined as the viscosity of the bubble. For a bubble, $\lambda = 0$. The traction boundary condition at the base fluid - bubble interface is (Kim and Karrila, 2005):

$$\mu\frac{\partial u_p}{\partial z} = \lambda\mu\frac{\partial v}{\partial z} \tag{3.4.2.4}$$

The solution for two bubbles with equal diameters has been derived in bispherical coordinates by (Kim and Karrila, 2005).

The relationship between the force and velocity for approaching bubbles and squeezing flow is (Kim and Karrila, 2005):

$$\frac{F_i}{6\pi\mu a U_i} = \frac{1}{3}\log\frac{a}{h} + \frac{2}{3}(\gamma_{Euler} + \log 2) + O(1) \tag{3.4.2.5}$$

where γ_{Euler} is Eulers constant (γ_{Euler} = 0.577216), a is the radius of the bubble, and h is the gap between the bubbles. This can then be rearranged to solve for the force, F_i, as a function of velocity, U_i, so that the remaining terms on the right become the resistance "squeeze" coefficient for a bubble, which is used instead of the a_{sq} coefficient derived by Ball and Melrose (Ball and Melrose, 1997). The force of bubble i is then:

$$F_i^{Bubble} = 6\pi\mu a U_i\left(\frac{1}{3}\log\frac{a}{h} + \frac{2}{3}\left(\gamma_{Euler} + \log 2\right)\right) \tag{3.4.2.6}$$

Equation (4.5.1.6) describes the normal force acting on bubble i, and therefore a_{sq}^{Bubble} is given by:

$$a_{sq}^{Bubble} = \pi\mu a\left(2\log\frac{a}{h} + 4\left(\gamma_{Euler} + \log 2\right)\right) \tag{3.4.2.7}$$

Using this squeeze coefficient, for two bubbles being pushed together with an equal and opposite external force, the gap between their surfaces can be described as a function of time (Fig. 3.4).

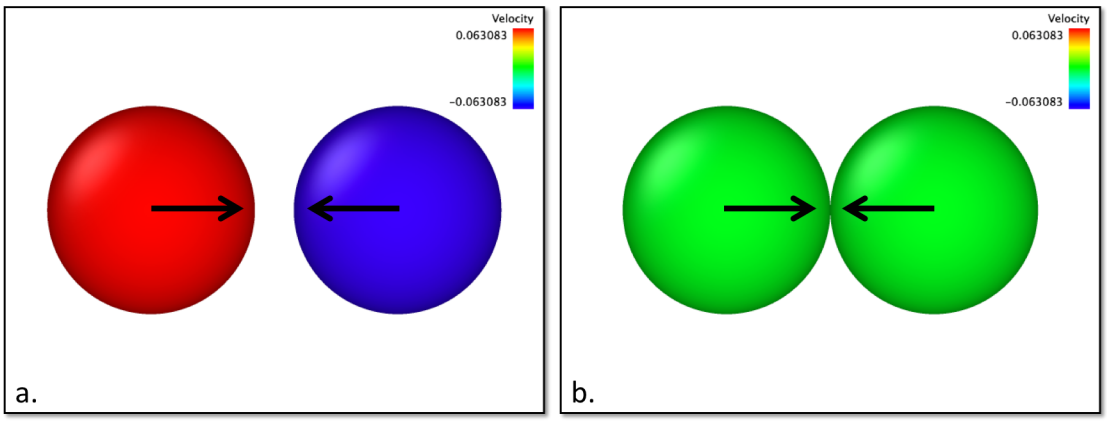

Figure 3.3: Two hard spherical particles, with no-slip surfaces, of equal size (diameter $= 1$) are being pushed together. a.) The starting positions of the particles. Their initial velocities in the horizontal direction is shown by their color. b.) At the end of the simulation, with constant external force pushing equally in opposite directions, the particles will approach very close to each other but should not touch in finite time.

The leading term for the squeezing flow between hard spheres with no-slip surfaces is $1/h$, and for bubbles it is $\log 1/h$. To look at the effects of this difference, we consider two particles being pushed together by applying an external force in equal and opposite directions to each particle. According to the lubrication theory (Kim and Karrila, 2005), hard spherical particles with no slip surfaces should not touch in finite time. In this squeezing flow, only the squeeze term is involved in the interaction, as the velocities of the particles are acting normal to the surface of the particles. The gap as a function of time with an external force of $f_x = 1$, we define by:

$$\frac{dh}{dt} = \frac{1}{-a_{sq}} \tag{3.4.2.8}$$

We define the total time by the integral, $I_{a_{sq}} := \int dt = -\int a_{sq} dh$. For hard spheres with no-slip boundary conditions:

$$I_{a_{sq}} = \frac{27h\pi}{40} + \frac{9h^2\pi}{224} + \frac{27}{40}h\pi \log\frac{1}{2h} + \frac{9}{112}h^2 \log\frac{1}{2h} + \frac{3}{8}\pi \log h \tag{3.4.2.9}$$

For a bubble with slip boundary conditions:

$$I_{a_{sq}}^{Bubble} = 2\pi h + 4\gamma_{Euler}\pi h + 2\pi h \log 4 + 2\pi h \log \frac{1}{h} \tag{3.4.2.10}$$

Define $h_0 = h(t = 0)$. This gives:

$$t = I_{a_{sq}}(h_0) - I_{a_{sq}}(h) \tag{3.4.2.11}$$

The gap as a function of time using Equation (3.4.2.11) compares the lubrication interactions of two hard sphere particles with no-slip surfaces and two spherical bubbles with slip surfaces approaching each other due to equal and opposite forces ($f_x = \pm 1$) acting on each particle/bubble (Figure 3.4). The diameter, d, was set to 1 for both particles/bubbles.

Figure 3.3 shows the velocity at the beginning and end of the simulations for hard spheres. The hard spheres with no-slip surfaces should not touch in finite time. Figure 3.3 also shows the particle positions relative to each other and the arrows indicate the motion of the particles approaching each other. The velocity of the particles at the beginning and end of the short simulation are indicated by the color of the particles. Initially, the particle velocities are equal and opposite due to the linear relationship with the forces on the particles. At the end of the simulation, the external force remains the same on each particle but the velocity approaches zero as the particles approach very close to each other and the gap becomes nearly zero. But, due to the high lubrication forces, the particle surfaces will not touch in finite time.

Figure 3.4 shows the gap from Figure 3.3 as a function of time. The hard spherical particles will come very close to each other but the high force due to the fluid between them will prevent them from touching in finite time. For bubbles, however, the force is weaker and the bubbles will overlap in finite time. In implementing this into simulations, for hard spheres with no slip boundaries, a cutoff distance is used for the interactions. If the particle gap is less than the cutoff, the cutoff

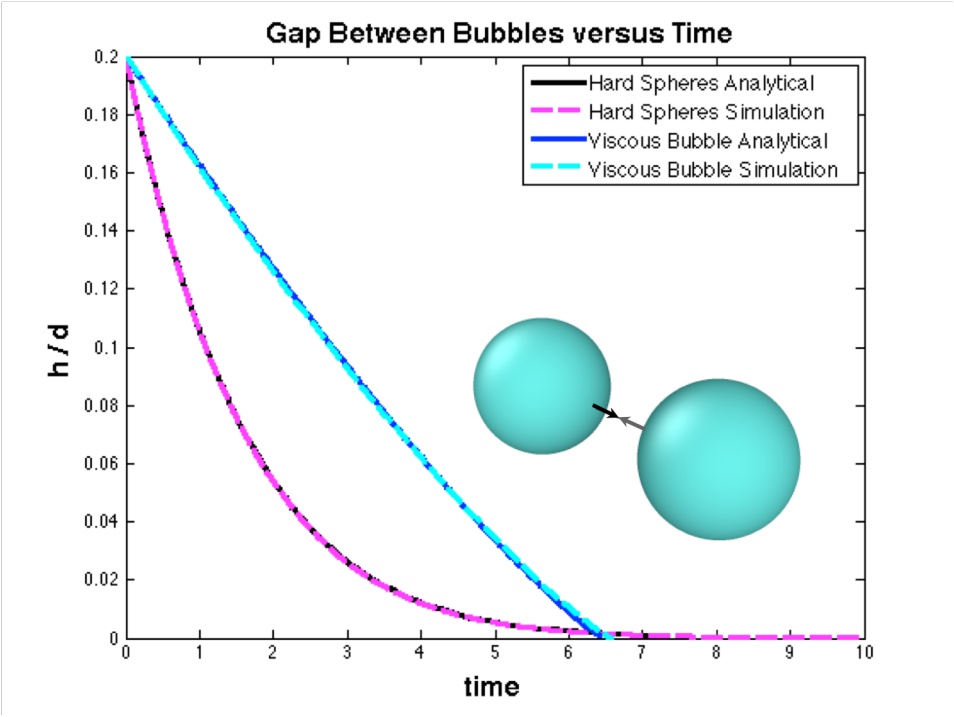

Figure 3.4: Gap between the approaching particles/bubbles as a function of dimensionless time. Comparison between hard spheres with no-slip on the surfaces (black $-$, magenta $--$) with bubbles with slip on the surfaces (viscous bubble, blue $-$, cyan $--$).

is used in place of the actual gap to calculate the forces and torques. Otherwise, the particles could overlap during the simulation. Another approach would be to make the timestep smaller and smaller to avoid overlaps (Ball and Melrose, 1997). For bubbles, especially at higher volume fractions where the bubbles interact more, as the suspension is sheared, the bubbles can overlap in an unphysical way. To keep the bubbles from overlapping completely, a direct force, $\boldsymbol{F}^{Direct}$, is also necessary. A real bubble surface is also not rigid so to account for this property, an elastic-like force, $\boldsymbol{F}^{Elastic}$, is also included. The total normal force on the bubble surface between interacting pairs is therefore described by:

$$\boldsymbol{F}^{Total} = \boldsymbol{F}^{Bubble} + \boldsymbol{F}^{Elastic} + \boldsymbol{F}^{Direct} \tag{3.4.2.12}$$

$\boldsymbol{F}^{Bubble}$ is defined by Equation (4.5.1.6). We next describe the elastic and direct forces, $\boldsymbol{F}^{Elastic}$ and $\boldsymbol{F}^{Direct}$, respectively.

3.4.3 Near-Field Bubble Interactions: Elastic Force

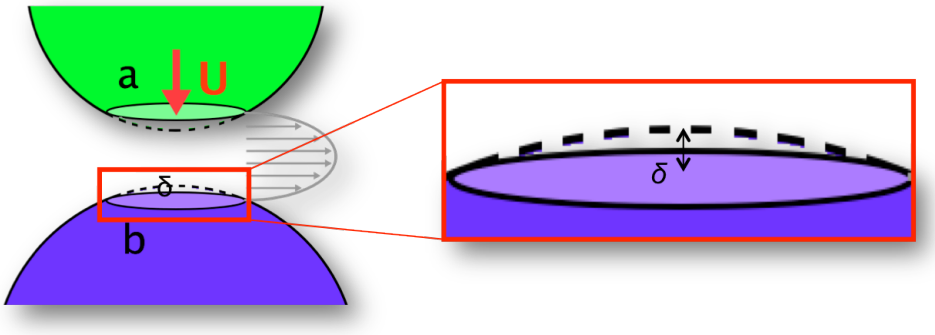

Figure 3.5: The bubble surface can deflect by an amount, δ.

As noted above, an elastic force is required to model the distortions away from spherical of the bubble due to the impingement of another bubble. The elastic force derivation follows (Rognon et al., 2010):

$$\boldsymbol{F}^{Elastic} = a_{Elas} E \delta \tag{3.4.3.1a}$$

$$a_{Elas} = \sqrt{a(2h + |\delta|)} \tag{3.4.3.1b}$$

$$\delta = \frac{(2a + h - r)}{2} \tag{3.4.3.1c}$$

Here, δ is the deflection of the bubble surface(Figure 3.5), a_{Elas} is the region of the bubble surface that is interacting in the lubrication force after deflection has caused the surface to become flattened, and E represents an *effective* modulus to deform the interface and bubble. In the simulations shown here, E was set to 10^2; this could in principle be calibrated to experiment. To limit the amount that the bubble surface can deflect, a maximum deflection value was set.

3.4.4 Near-Field Bubble Interactions: Direct Force

The direct force is necessary to keep the bubbles from overlapping during the simulation. It represents the force due to the surfactant, which can be attractive and repulsive (Tabakova and Danov, 2009) depending on the properties of the surfactant and the separation of the bubbles. The surfactant forces can include van der Waals and hydrostatic attraction, electrostatic repulsion, steric repulsion, etc. (Tabakova and Danov, 2009), however, the properties of the surfactant are not the focus of this research and are not generally known as they are proprietary. Therefore, no specific surfactant will be considered. Herein, the direct force is represented by a Lennard-Jones potential force that acts normal to the bubble surface along the line between the center of interacting bubble pairs. Rognon and Gay (Rognon and Gay, 2008, 2009) developed soft dynamics to simulate dense collections of elastic particles. Soft dynamics can only simulate closely interacting particles and a confining stress is used to keep the suspension in a dense configuration. Rognon, Einav, and Gay (Rognon et al., 2010, 2011) include a direct force that represents the steric repulsion between elastic particles. It increases steeply when the particles come in close contact and prevents the particles from overlapping. In the simulations shown here, a direct force is deployed in a similar way. The Lennard-Jones potential included with LAMMPS (LAM, 2003) was used as the direct force.

The Lennard-Jones potential is based on van der Waals interactions (Rognon et al., 2010, 2011) and includes both repulsive and attractive forces. A Lennard-Jones potential that was less repulsive than the standard Lennard-Jones potential was used here and is given by (LAM, 2003):

$$\phi_{LJ} = 4\epsilon \left[\left(\frac{\sigma}{r}\right)^9 - \left(\frac{\sigma}{r}\right)^6 \right] \tag{3.4.4.1}$$

ϵ is the energy scale and σ is the length scale. The influence of the values of ϵ and σ on systems dynamics are described below. $\left(\frac{\sigma}{r}\right)^9$ is the repulsive part[2] and $\left(\frac{\sigma}{r}\right)^6$ is the attractive portion. The direct force, F^{Direct}, between bubbles is then the derivative of Equation (3.4.4.1). Here, this force

[2]The standard Lennard-Jones potential is $\phi_{LJ} = 4\epsilon \left[\left(\frac{\sigma}{r}\right)^{12} - \left(\frac{\sigma}{r}\right)^6 \right]$

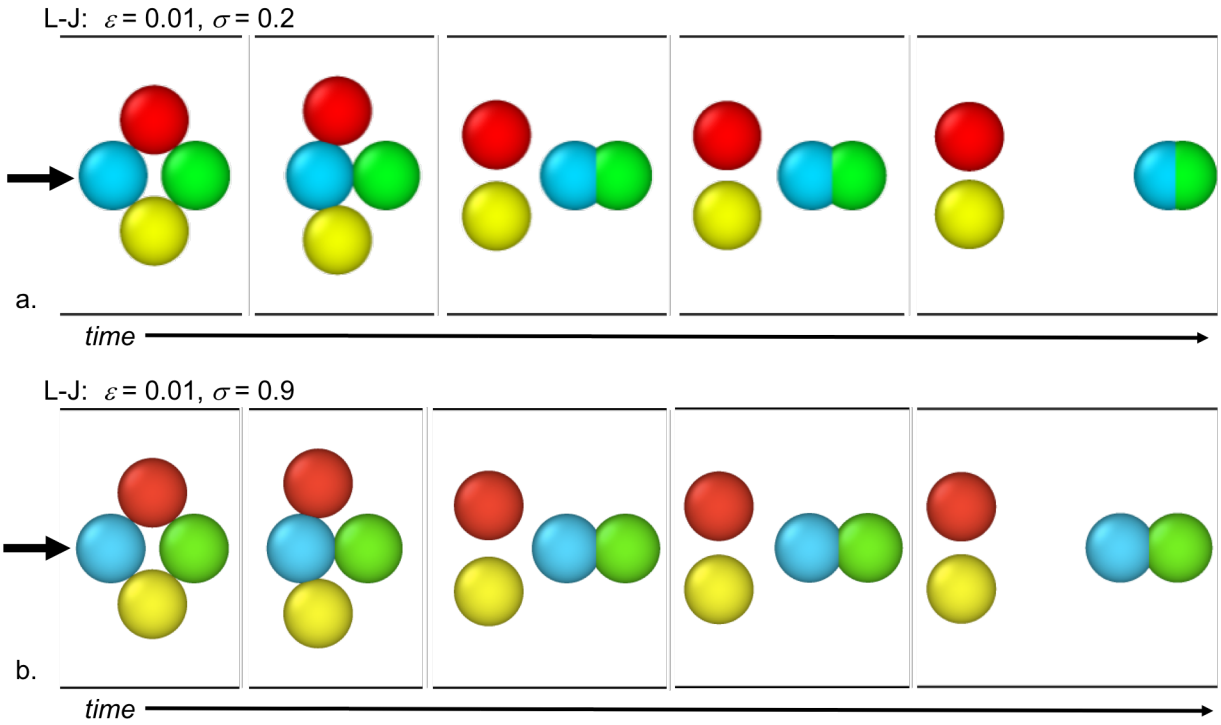

Figure 3.6: Simple four-bubble configurations were used to explore the influence of the ϵ and σ values of the Lennard-Jones potential. The force is applied to the bubble indicated by the arrow in the first time frame. The configuration changes of the bubbles are displayed over a several time steps. The left most frame is the starting configuration and the right most frame shows the center bubbles at their limit of deflection due to the force applied. The combination of the ϵ and σ values dictate the level that bubbles are allowed to deflect and the level of attraction of the bubbles. The bubble force and the elastic force are also included in the interaction.

keeps the bubbles from overlapping completely but also allows for the elastic interaction.

3.4.5 The Lennard-Jones Parameters for the Direct Force

The values for ϵ and σ can be varied to adjust: (1) the amount that the bubbles' surface can deflect, and (2) the level of attraction between the bubbles. To test the influence of ϵ and σ, four bubble configurations were used. A constant force of 1 was applied to the left most bubble and the images shown in Figure 3.7 show a snapshot in time of the simulation after the left-most bubble has started interacting with the other bubbles. Periodic boundary conditions were used so that once the center

bubbles passed through the top and bottom bubbles, they were remapped into the simulation box on the left side. As the simulations progressed, the amount of deflection and attraction between the bubbles was observed.

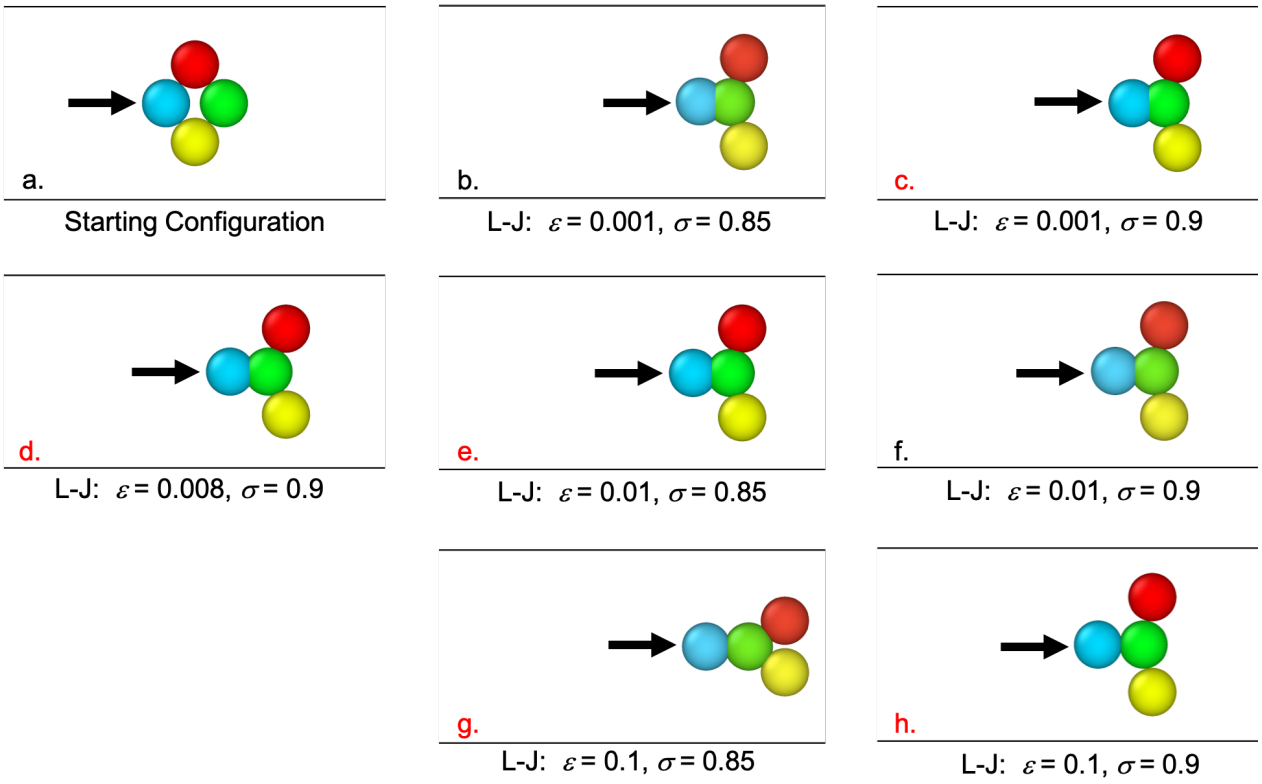

Figure 3.7: Simple four-bubble configurations were used to explore the influence of the ϵ and σ values of the Lennard-Jones potential. The bubble direct force and the elastic force are included in the interaction. a.) Shows the starting configuration of the bubbles. The arrow shows where the force is applied. A force was only applied to the bubble indicated. b.), c.), d.), e.), f.), g.) and h.) show the influence of changing the values of ϵ and σ.

Figure 3.6 shows the progression of the bubble configurations over several time steps. If the values of ϵ and σ are not chosen correctly, then the bubbles can overlap too much and do not represent the system dynamics properly. Values of $\epsilon = 0.01$ and $\sigma = 0.2$ allow too much overlap (deflection) of the bubbles in an unrealistic manner. Another observation is that the top and the bottom bubbles move close to each other and almost touch. The combination of ϵ and σ also dictate the amount of attraction between the bubbles. The lower the value of σ – which sets the length scale of the interaction – the greater the overlap, for a given value of ϵ. Figure 3.7 shows the influence of several

parameter combinations. Figure 3.7a. shows the initial configuration of the bubbles. The lower the value of ϵ, the greater the overlap, but the slightly lower value of σ causes the bubbles to be more attractive and have a "softening" effect. In Figure 3.7g, as the force continues to push the left most bubble, the bubbles in the middle were also pushed because they were attracted to each other similar to what is observed in Figure 3.6a. The combination of the higher energy and length scale, are shown in Figure 3.7h. The combination of the Lennard-Jones potential $\epsilon = 0.1$ and $\sigma = 0.9$ values, result in a direct force that does not allow the bubble surface to deflect. Effectively, the bubbles then act like hard spheres.

The Lennard-Jones potential is being utilized as the direct force representing the surfactant properties, which means that it must have the proper level of repulsion to keep the bubbles from completely overlapping but also some attraction to represent the surfactant. Five combinations of ϵ and σ were considered to determine the values that best represent the physical properties of the bubbles. Figures 3.7c., d., e., g., and h. show the combinations that were simulated with full system sizes.

Figure 3.7c. corresponds to $\epsilon = 0.001$ and $\sigma = 0.9$, which allows the bubbles to deflect sufficiently but the attraction, though not pictured here, is high enough that the top and bottom bubbles approach close to each other when the center bubbles pass through. Lennard-Jones values of $\epsilon = 0.01$ and $\sigma = 0.85$ (Figure 3.7e.) resulted in similar results as the combination of $\epsilon = 0.001$ and $\sigma = 0.9$. For the values of $\epsilon = 0.1$ and $\sigma = 0.85$ (Figure 3.7g.), the top and bottom bubbles touch after the center bubbles pass through. Figure 3.8a. shows the time progression of the bubbles' motion from Figure 3.7g. As the left-most bubble is pushing on the other bubbles, the deflection of the surface appears to be reasonable but when the center bubbles are pushed through the top and bottom bubbles, the top and bottom bubbles are excessively attracted to each other. For values of $\epsilon = 0.1$ and $\sigma = 0.9$ (Figure 3.7h. and Figure 3.8b.), the physics of the problem are similar to hard spheres. The bubbles can still slip by each other with no resistance tangent to the bubble surface but the higher σ value did not allow deflection of the bubbles' surface so the results mimic those of hard spheres. So even without a shearing resistance in the interaction, the behavior of the bubbles is similar to hard

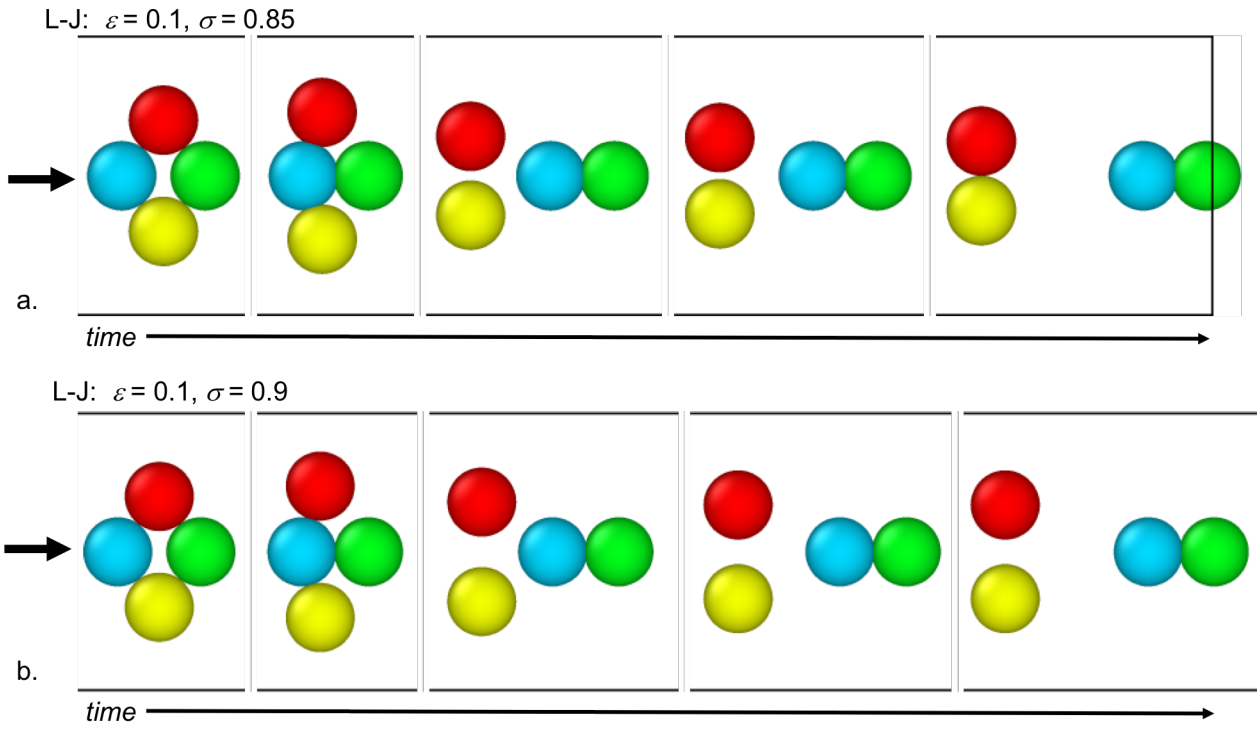

Figure 3.8: The configuration changes of the bubbles are displayed over a several time steps. a.) Corresponds to Figure 3.11e. and b.) Corresponds to Figure 3.11f. The force is applied to the bubble shown by the arrow in the first time frame. The left most frame is the starting configuration and the right most frame shows the center bubbles at their limit of deflection due to the force applied. The combination of the ϵ and σ values dictate the level that bubbles are allowed to deflect and the level of attraction of the bubbles. The bubble force and elastic force are also included in the interaction.

spherical particles. The best combination of values was $\epsilon = 0.008$ and $\sigma = 0.9$ (Figure 3.7d.), which allowed some deflection of the bubble surface and some attraction.

3.5 Molecular Dynamics Simulation Method

LAMMPS[3] – the Large-scale Atomic/Molecular Massively Parallel Simulator – is an open-source classical (non-quantum) molecular dynamics code developed and maintained at Sandia National

[3] `lammps.sandia.gov`

Labs (Plimpton, 1995). We use LAMMPS with the FLD method[4] combined with bubble surface properties.

3.5.1 Generation of Initial Configurations of Bubbles

Bubble systems were generated by first creating smaller sets in a $10 \times 10 \times 10$ box. The bubbles with a diameter of 1 were randomly placed to create different volume fractions (10%, 20%, 30%, 40%, 45%, and 50%) of bubbles all having the same system volume. Once the bubbles are randomly placed, a soft potential is used with an energy minimization to remove overlaps in the initial configuration that are unphysical[5]. The energy of the soft potential is (LAM, 2003):

$$E = A\left(1 + \cos\left(\frac{\pi r}{r_{cut}}\right)\right), \quad r < r_{cut} \tag{3.5.1.1}$$

where r is the distance between bubbles, A is the pre-factor in energy units that was initially set low and ramped up, and r_{cut} is the cut off distance.

To avoid effects from the system size, testing was done to determine the appropriate system size that shows no further size dependence. The system sizes were progressively doubled in all coordinate directions until an appropriate size, where the system size did not impact the calculation of the relative viscosity, was achieved. It was determined that replicating the original system size of $10 \times 10 \times 10$ four times in each direction eliminated system size effects. Once this configuration was replicated, the bubbles were then moved around using the random Brownian pair interaction in LAMMPS to make the bubble arrangements random again. This step was not part of the dynamics but was simply to create a random placement of the bubbles after replicating the same arrangement of bubbles, for input into the simulations.

[4] As noted previously, we have extended LAMMPS to include bubble-like surface properties in the resistance terms.

[5] We emphasize that the soft potential is used only in generating a physical initial configuration, and plays no role once the simulation begins.

3.5.2 Implementation of the Shearing Flow

The shearing flow was implemented as described in (Rosenbaum et al., 2019). Three dimensional simulations were performed using Lees-Edwards boundary conditions (Lees and Edwards, 1972). For Lees-Edwards boundary conditions and strains imposed in the xy-direction, the velocity of each bubble is then a function of its position in the y-direction as shown in Figure 3.9. When a bubble crosses the simulation boundary in any direction, the velocity of the bubble is remapped to correspond to the new position in the simulation box[6]. The suspensions of different volume fractions were all sheared as shown in Figure 3.9 until the stress reached a constant value and the value of $\dot{\gamma} \times t_{total}$ reached 200. t_{total} is the length of time that the simulation was run and $\dot{\gamma} \times t_{total}$ was used so that all simulations results were comparable. Basically, all simulations were run till the box was sheared the same amount as opposed to being run for the same length of time. Testing different time steps revealed that the dimensionless time step should be kept below a value of 0.002 for the FLD simulations, however, a timestep of $\Delta t = 0.001$ was used for all simulations shown here. An explicit time-integration scheme was used.

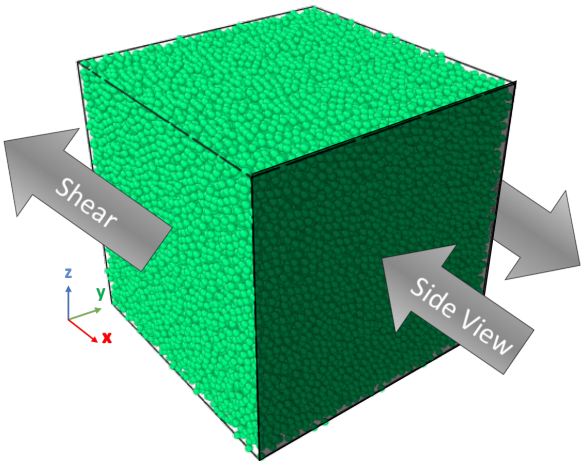

Figure 3.9: The bubble suspensions are sheared in the direction shown and when the side view is shown, it is a view through the whole system of bubbles.

The total strain on the simulation box is defined as $\dot{\gamma} \times \Delta t$, the product of the strain rate $\dot{\gamma}$ and

[6]See e.g. (Dayal and James, 2010) for a discussion of this and (LAM, 2003) for the implementation, which uses a function called "fix deform" to apply a strain rate to the simulation box in the specified orthogonal box directions.

timestep Δt. For the quasi-static setting, given $\dot{\gamma} \times \Delta t$, the time-history of the stress and viscosity should be the same when time is appropriately re-scaled.

The stress in the system is calculated by summing the stresses computed for each bubble. Ignoring the kinetic energy contributions that are negligible here, the stress on a bubble is defined by (LAM, 2003; Tadmor and Miller, 2011):

$$\sigma_{i,\alpha\theta} = \frac{1}{V_i}[-\frac{1}{2}\sum_{n=1}^{N_p}(r_{1_\alpha}F_{1_\theta} + r_{2_\alpha}F_{2_\theta})] \tag{3.5.2.1}$$

where, α and θ run over the coordinate directions to compute the 6 components of the symmetric stress tensor. The sum runs over the N_p neighbors of the bubble under consideration. $\boldsymbol{r}_1$ and $\boldsymbol{r}_2$ are the positions of every bubble pair that has pairwise interactions, and $\boldsymbol{F}_1$ and $\boldsymbol{F}_2$ are the corresponding forces.

For a simulation box with volume, V, the stress from each bubble is summed to determine the total stress of the system of bubbles and is used to calculate the viscosity. With Lees-Edwards boundary conditions imposed, the relative viscosity (i.e., the viscosity ratio) is calculated from the average total stress once the system has reached steady state:

$$\mu_{\text{relative}} = \frac{\mu_{\text{effective}}}{\mu} = \frac{\sum_i \sigma_{xy}}{\dot{\gamma}\mu V} \tag{3.5.2.2}$$

3.6 Viscosity Ratio of the Bubble Suspension

An important reason to add bubbles to a fluid is to increase the effective viscosity. In this section, we examine the effect of the bubble volume fraction on the viscosity based on the molecular dynamics calculations.

Recall the definition of the viscosity ratio in Equation (3.5.2.2). The viscosity ratio as a function

of bubble volume fraction is shown in Figure 4.12. The initial configurations were all the same for comparison of the effects of the Lennard-Jones parameters ϵ and σ values on the viscosity. As described above, the choice of $\epsilon = 0.1$ and $\sigma = 0.85$ did not display proper system dynamics and the relative viscosity calculated was significantly higher than the other simulations, which is also unrealistic. The choice of $\epsilon = 0.1$ and $\sigma = 0.9$ produced physics that were not characteristic of bubbles, as described above, and the relative viscosity values are also unrealistic.

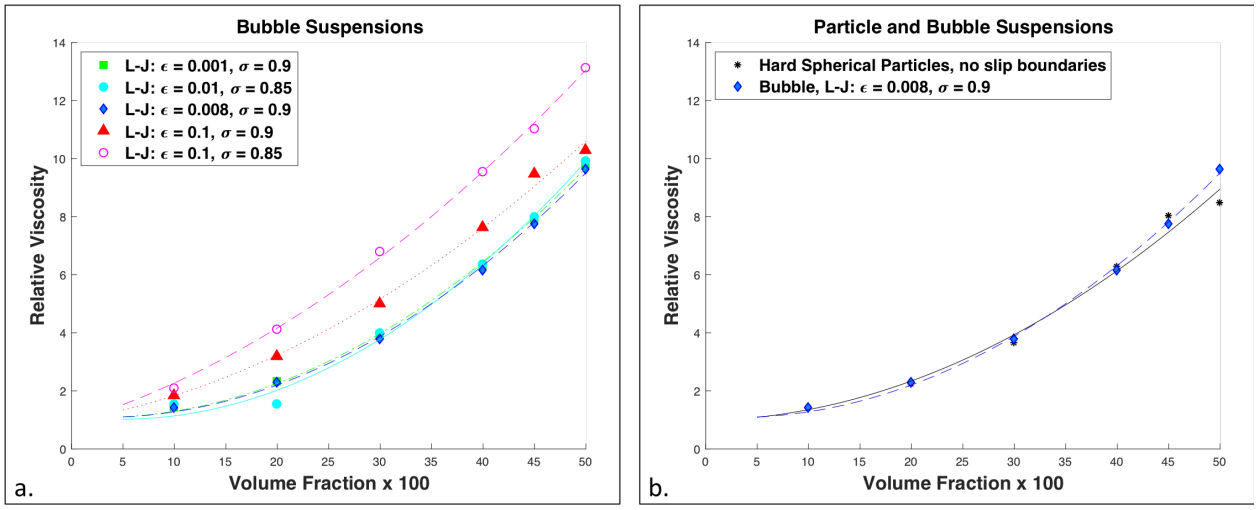

Figure 3.10: The relative viscosity or viscosity ratio is shown as a function of the volume fraction of bubbles in the suspension. The lines in the figures are second order polynomial fits through the calculated relative viscosity points shown and including the point $(0, 1)$ a.) The influence of ϵ and σ of the Lennard-Jones direct force in the bubble interaction are shown. b.) Hard sphere suspension results (Rosenbaum et al., 2019) are compared with the results of bubble suspensions.

The combination of the ϵ and σ values influence the level of bubble deflection and the level of attraction. The level of deflection and the level of attraction between the bubbles ultimately influences the distance between bubbles and the force between bubble pairs, which is used to compute the stress on each bubble. The effect of ϵ and σ are shown in Figure 3.7c., d., e., g., and h. for the relative viscosity values displayed in Figure 4.12a. The relative viscosity is dependent on the stress in the system, which is a summation of the stresses on each bubble. Figure 3.11 shows the value of stress in the xy-direction, $\sigma_{i,xy}$, for each bubble at the final configuration of the simulation. Figure 3.11a shows the stress per bubble at the beginning of the simulation. The results are only

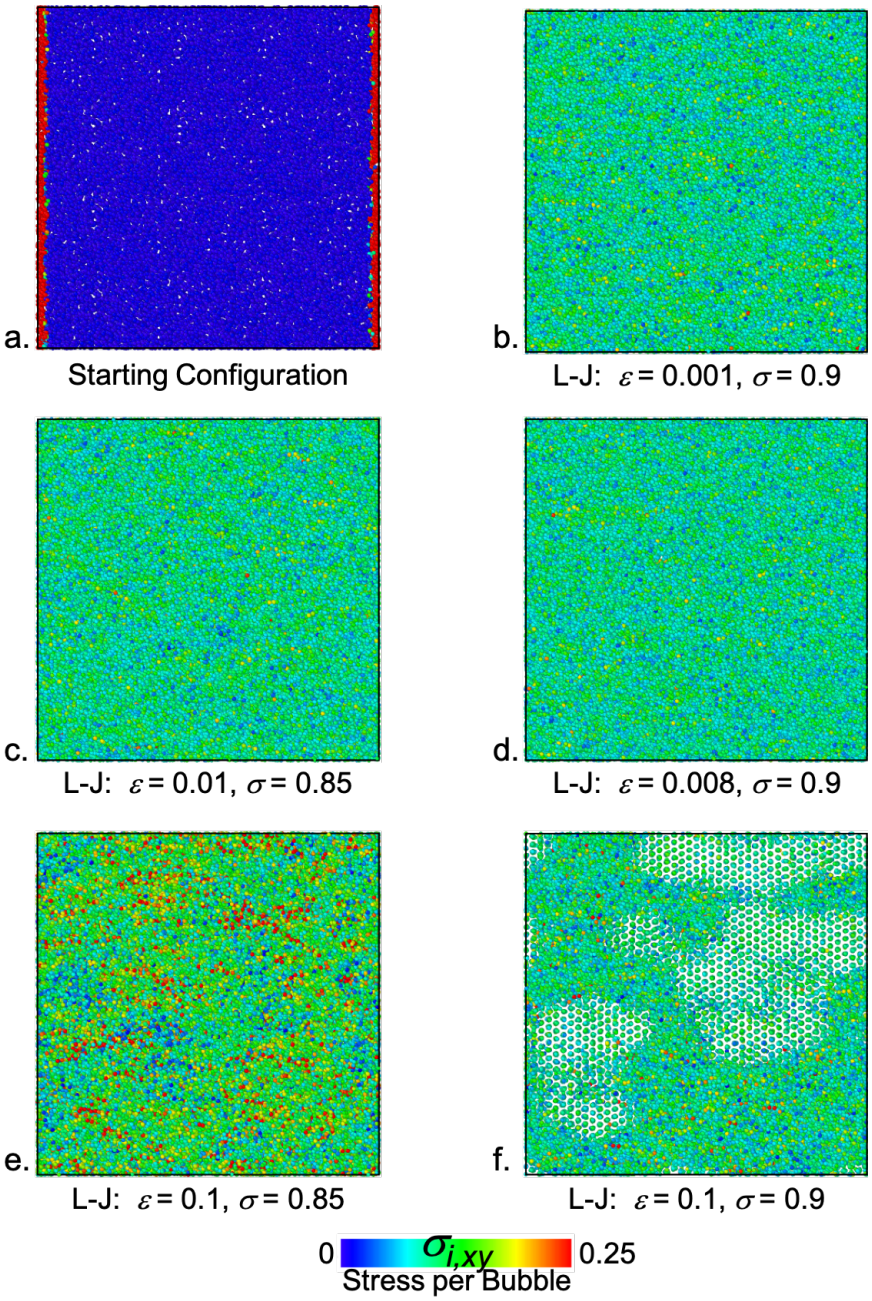

Figure 3.11: The final configuration of the 0.50 volume fraction of bubbles is shown in b.), c.), d.), e.), f.) and the initial configuration of the bubbles and stress per bubble is shown in a.). The color of each bubble corresponds to the value of the stress per bubble (from Equation (3.5.2.1)). The bubbles are shown at half size and form the view shown in Figure 3.9.

shown for the 0.50 bubble volume fraction suspensions because the close-range interactions that were developed here are the most dominant in dense suspensions. Figure 3.11e., corresponding to

the choice of $\epsilon = 0.1$ and $\sigma = 0.85$, shows an overall higher stress on each bubble – when compared to the other simulation results shown – which results in higher viscosity values than when the other Lennard-Jones parameters are used. The choice of $\epsilon = 0.1$ and $\sigma = 0.85$ does not produce reasonable relative viscosity results and the problem dynamics are not physically realistic either as shown in 3.7g.

The final choice of $\epsilon = 0.008$ and $\sigma = 0.9$ of the Lennard-Jones parameters were chosen based on allowing the bubbles to overlap slightly but also have only a small amount of attraction to represent the effects of the surfactant. The bubble properties described from this point further will assume to have $\epsilon = 0.008$ and $\sigma = 0.9$ values for the Lennard-Jones potential. The bubble configurations used as inputs for the simulation results shown here are the same as those used for monodisperse hard spheres with no slip boundary conditions (Rosenbaum et al., 2019). The viscosity ratio of monodisperse hard spheres with no-slip boundaries are shown in Figure 4.12b, for comparison to the viscosity calculated for bubbles with slip boundaries and the ability to deform elastically in the manner described in Section 3.4. With the parameters chosen for these simulations, the viscosity ratio of bubble suspensions – as modeled here – does not vary an appreciable amount from the viscosity ratio of monodisperse hard sphere suspensions.

3.7 Structuring of Suspensions of Bubbles v. Particles

As discussed above, the structuring or clustering of bubbles in suspension can lead to weak mechanical regions for crack propagation or pathways for gas migration. In this section, we compare monodisperse bubble suspensions to monodisperse particle suspensions using molecular dynamics calculations.

Using parameters in the simulations that maintain proper system dynamics, the numerical simulations show that the relative viscosity calculated is not influenced a significant amount by the properties of the bubble surface compared to hard sphere particle suspensions. Figure 3.12 com-

pares monodisperse particles to monodisperse bubbles. The stress per particle/bubble is indicated by color. The input configurations are the same for comparison and only the 0.50 volume fraction is compared because it is the higher volume fraction where detrimental clustering or ordering could occur (Rosenbaum et al., 2019). The resulting relative viscosity is the same for both particles and bubbles but the per particle stress varies more in the hard sphere particles. Because the summation of the stress results in similar total average stress, the relative viscosity is also similar for both particles and bubbles.

The difference in the surface properties of particles versus bubbles affects the spatial arrangement. The monodisperse particles have a lubrication squeezing force that prevents them from touching. The particles also have shearing resistance. The properties of monodisperse particle suspensions was explored previously (Rosenbaum et al., 2019), and it was shown that volume fractions of 0.47 and higher show rearrangement and ordering. Monodisperse hard spherical particles, with no-slip boundary conditions, in a suspension will go from a random placement to an ordered placement that locally resembles a crystalline packing. Figure 3.13 compares the qualitative results of monodisperse particles to monodisperse bubbles. In Figure 3.13b, the re-arrangement and structuring of the particles can be observed. In Figure 3.13a, the alignment of the particles can also be seen in the form of chains of particles. However, the influence of the bubble surface properties keep the bubbles relatively well dispersed throughout the simulation. Figures 3.13c and d show the results of the bubble suspensions described here. Unlike the hard spheres, the bubbles have a softer force between them, no shearing resistance due to the slip surface, and a surface that is able to deflect. The effects of the bubble surface properties help to keep the bubbles dispersed and the same ordering of particles seen in Figure 3.13b is not observed in Figure 3.13d.

In Figure 3.13, the correlation refers to the pair correlation function of each bubble. The pair correlation quantifies the number of neighboring bubbles in volumetric shells (of equal thickness)

around each bubble. The pair correlation of each bubble was calculated using the expression:

$$g(\eta) = \frac{N_S}{\frac{N}{V} V_S} \tag{3.7.0.1}$$

N_S is the number of bubbles in the current shell, S. V_S is the volume of the current shell and $\frac{N}{V}$ is the number density of bubbles in the whole simulation box. The pair correlation values of the particles/bubbles, shown in Figure 3.13, is the probability of finding neighboring particles/bubbles within a spherical radius, η, of 1.5 away from each particle/bubble. The pair correlation relates to the ordering of the particles/bubbles. The hard sphere suspensions that show ordering of the particles have a higher correlation value for the particles in those regions. The bubble suspensions maintain an overall lower level of correlation. The level of correlation of the bubbles is consistent throughout the whole simulation box.

3.8 Discussion

Due to the slip on the bubble surface, lack of shearing resistance, and by allowing the bubble surface to deflect a small amount, interacting bubble pairs can pass by each other with less restriction. This results in less jamming of the bubbles, which is what causes bubbles to start forming linear structures (Figure 3.12b.). With application to foamed cements, it is desired to keep the bubbles dispersed throughout the cement slurry, during placement in the well and once placed. As shown in (Rosenbaum et al., 2019), the effect of the particle polydispersity is to reduce clustering. Also, monodisperse bubbles structure and cluster less when compared to monodisperse particles.

One of the benefits of foaming the cement is the increase in the viscosity. The increased viscosity with the amount of added bubbles enhances the drilling mud removal (Frisch et al., 1999), especially in the type of mud used in geothermal wells (Bour and Rickard, 2000). Our numerical calculations show that in both particle and bubble suspensions, the viscosity increases with the

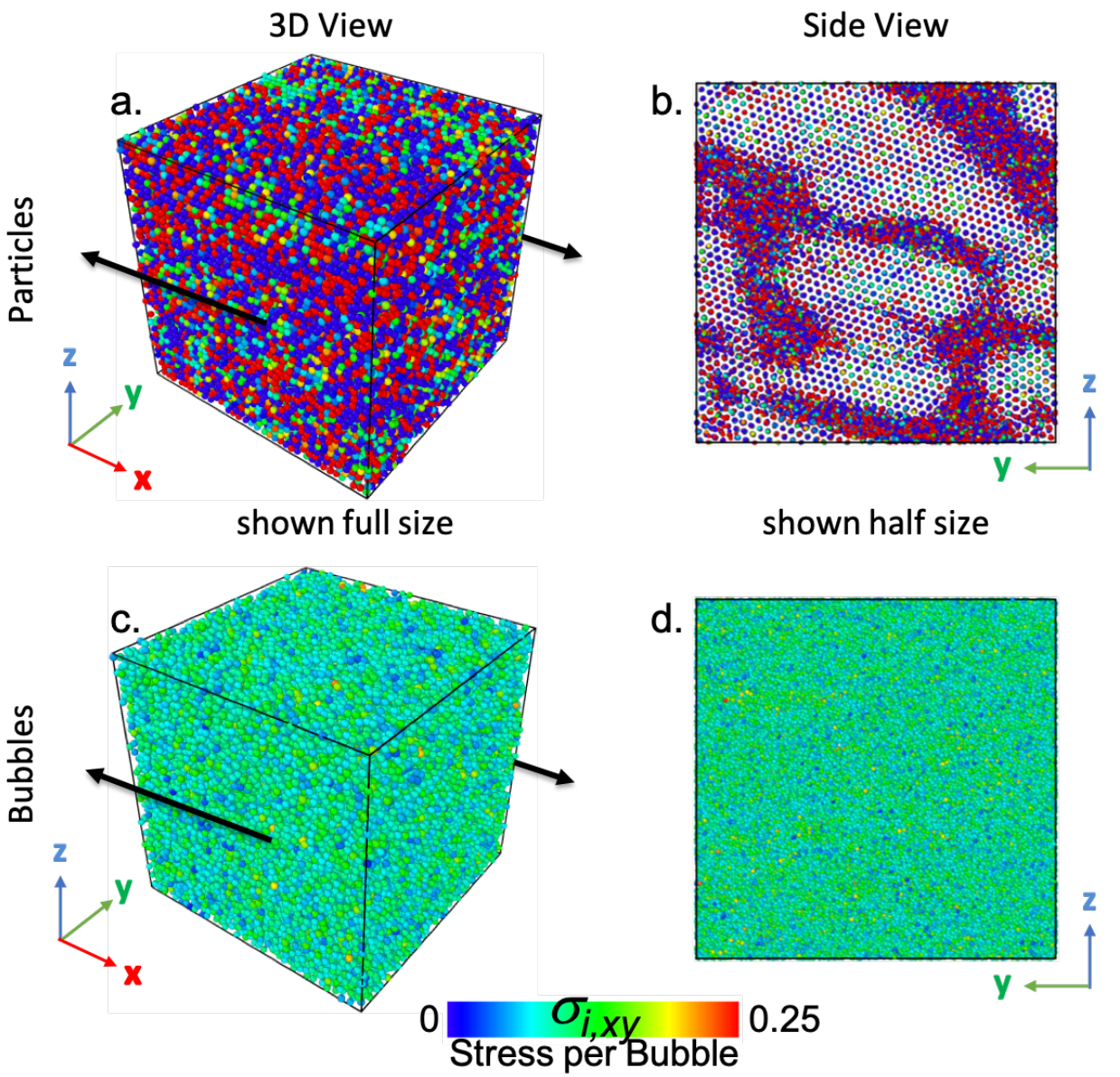

Figure 3.12: The stress on each particle/bubble is shown at the final configuration of 0.50 volume fraction of particles/bubbles simulations is shown. Particles are compared to the bubbles. For the bubble results shown, the values of the Lennard-Jones potential are $\epsilon = 0.008$ and $\sigma = 0.9$.

increase in volume fraction of spherical suspending objects (Batchelor and Green, 1972).

It is expected – and will be explored in the future – that the combination of bubble surface properties with polydispersity in the bubbles sizes would further reduce the propensity for bubble clustering to occur. In application, it is difficult to create bubble dispersions of exactly equal bubbles so in actual

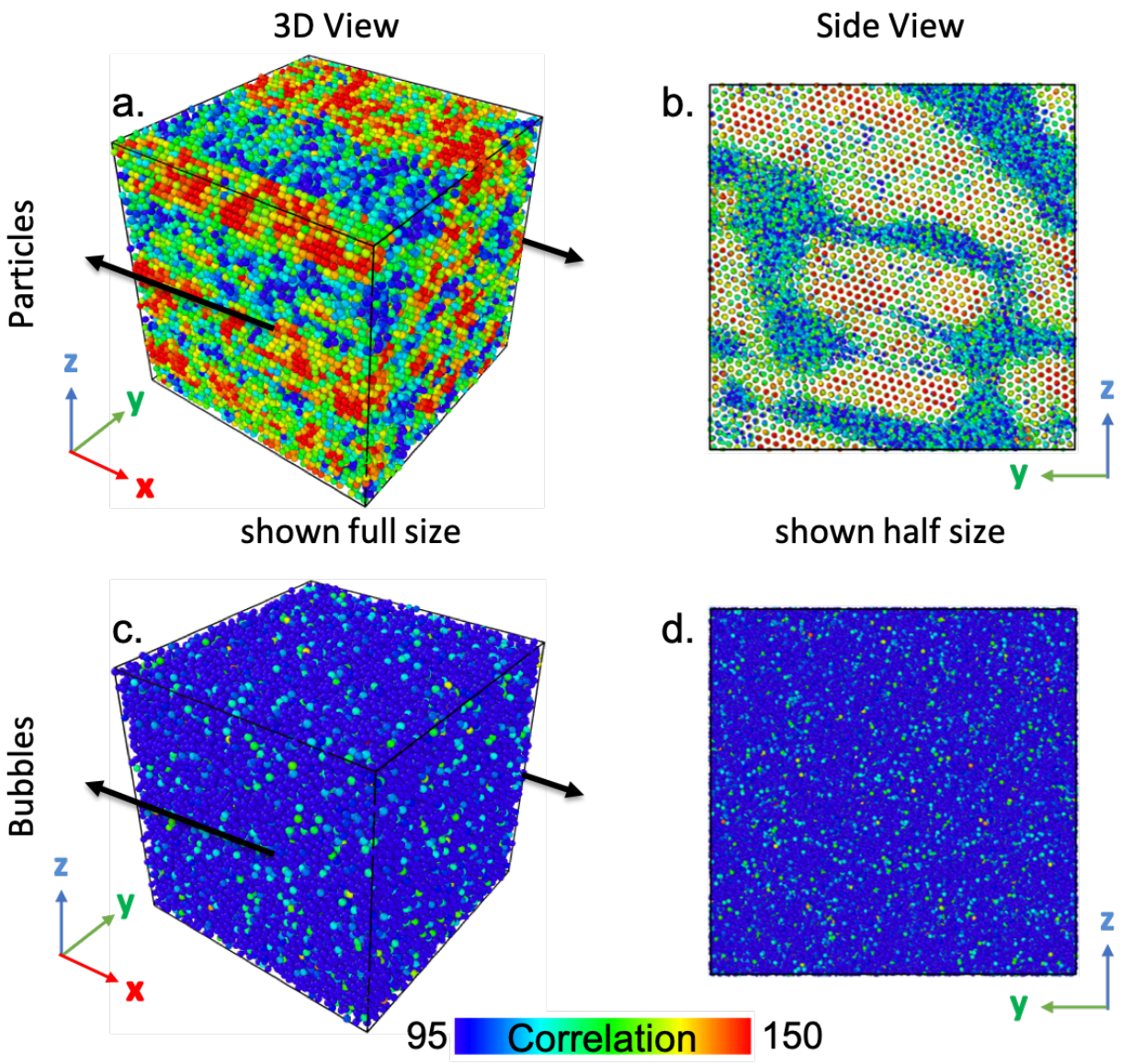

Figure 3.13: The correlation at the final configuration of 0.50 volume fraction of particles/bubbles simulations is shown. Particles are compared to bubbles. For the bubble results shown, the values of the Lennard-Jones potential are $\epsilon = 0.008$ and $\sigma = 0.9$.

foamed cement, the polydispersity of the bubbles in the foamed cement help to keep the bubbles dispersed. However, simulations with polydisperse bubble sizes is a significant step beyond the monodisperse modeling presented here, and is an important goal for the future.

The calculations here assume Newtonian suspending fluids, which is a limitation of the overall

Stokesian Dynamics framework. Homogenization or mixture-theory based approaches, e.g. based on (Avazmohammadi and Castañeda, 2016; Christoffersen et al., 1981; Gao et al., 2011, 2012; Lipton and Avellaneda, 1990; Lipton and Vernescu, 1994; Massoudi, 2002, 2003, 2008, 2010), may enable the formulation of continuum models that can provide insight into particle structuring while also accounting for the complex rheology of cement paste.

3.9 Chapter 3 References

Bibliography

(2003). *LAMMPS Users Manual*. Sandia National Laboratories.

American Petroleum Institute (2010). Isolating Potential Flow Zones During Well Construction - API Standard 65 Part 2.

Avazmohammadi, R. and Castañeda, P. P. (2016). Macroscopic rheological behavior of suspensions of soft solid particles in yield stress fluids. *Journal of Non-Newtonian Fluid Mechanics*, 234:139–161.

Ball, R. C. and Melrose, J. R. (1997). A simulation technique for many spheres in quasi-static motion under frame-invariant pair drag and Brownian forces. *Physica A: Statistical Mechanics and its Applications*, 247(1-4):444–472.

Batchelor, G. and Green, J. (1972). The determination of the bulk stress in a suspension of spherical particles to order c 2. *Journal of Fluid Mechanics*, 56(3):401–427.

Bechinger, C., Sciortino, F., and Ziherl, P. (2013). *Physics of Complex Colloids*. IOS Press.

Beltempo, A., Zingales, M., Bursi, O. S., and Deseri, L. (2018). A fractional-order model for aging materials: An application to concrete. *International Journal of Solids and Structures*, 138:13–23.

Bossis, G. and Brady, J. F. (1984). Dynamic simulations of sheared suspensions. {I.} General method. *J. Chem. Phys.*, 80(10):5141–5154.

Bour, D. and Rickard, B. (2000). Application of Foamed Cement on Hawaiian Geothermal Well. *Geothermal Resources Council Transactions*, 24.

Brady, J. (1988). Stokesian Dynamics. *Annual Review of Fluid Mechanics*, 20(1):111–157.

Bybee, M. D. (2009). *HYDRODYNAMIC SIMULATIONS OF COLLOIDAL GELS: MICROSTRUCTURE, DYNAMICS, AND RHEOLOGY*. PhD thesis, University of Illinois at Urbana-Champaign.

Christoffersen, J., Mehrabadi, M., and Nemat-Nasser, S. (1981). A micromechanical description of granular material behavior. *Journal of applied mechanics*, 48(2):339–344.

Dalton, L. E., Brown, S., Moore, J., Crandall, D., and Gill, M. (2018). Evolution Using CT Scanning : Insights From Elevated-Pressure Generation. (January):1–11.

Davis, R. H., Schonberg, J. a., and Rallison, J. M. (1989). The lubrication force between two viscous drops. 77(1989).

Dayal, K. and James, R. D. (2010). Nonequilibrium molecular dynamics for bulk materials and nanostructures. *Journal of the Mechanics and Physics of Solids*, 58(2):145–163.

de Rozières, J. and Ferrière, R. (1991). Foamed-Cement Characterization Under Downhole Conditions and Its Impact on Job Design. *SPE Production Engineering*, (August):297–304.

de Rozieres, J. and Griffin, T. J. (1990). Chapter 14 Foamed Cements. In Nelson, E. B., editor, *Well Cementing*, pages 14.1 – 14.19. Schlumberger Educational Services, 300 Schlumberger Drive, Sugar Land, Texas 77478.

Frisch, G. J., Services, H. E., and Graham, W. L. (1999). SPE 55649 Assessment of Foamed - Cement Slurries Using Conventional Cement Evaluation Logs and Improved Interpretation Methods. *SPE Rocky Mountain Regional Meeting*.

Gao, T., Hu, H. H., and Castañeda, P. P. (2011). Rheology of a suspension of elastic particles in a viscous shear flow. *Journal of Fluid Mechanics*, 687:209–237.

Gao, T., Hu, H. H., and Castañeda, P. P. (2012). Shape dynamics and rheology of soft elastic particles in a shear flow. *Physical review letters*, 108(5):058302.

Gaudron, R., Warnez, M., and Johnsen, E. (2015). Bubble dynamics in a viscoelastic medium with nonlinear elasticity. *Journal of Fluid Mechanics*, 766:54–75.

Guillot, D. (1990). Rheology of Well Cement Slurries. *Developments in Petroleum Science*, 28(C):4–1–4–37.

James, R. D. and Müller, S. (1994). Internal variables and fine-scale oscillations in micromagnetics. *Continuum Mechanics and Thermodynamics*, 6(4):291–336.

Jeffrey, D. J. and Onishi, Y. (1984). Calculation of the resistance and mobility functions for two unequal rigid spheres in low-Reynolds-number flow. *Journal of Fluid Mechanics*, 139(-1):261.

Kim, S. and Karrila, S. J. (2005). *Microhydrodynamics: Principles and Selected Applications*. Dover Publications, Inc., Mineola, NY, 2nd editio edition.

Kumar, A. (2010). *Microscale Dynamics in Suspensions of Non-Spherical Particles*. Doctor of philosophy, University of Illinois at Urbana-Champaign.

Kumar, A. and Higdon, J. J. L. (2010). Origins of the anomalous stress behavior in charged colloidal suspensions under shear. *Physical Review E - Statistical, Nonlinear, and Soft Matter Physics*, 82(September):1–7.

Kutchko, B., Crandall, D., Gill, M., McIntyre, D., Spaulding, R., Strazisar, B., Rosenbaum, E., Haljasmaa, I., Benge, G., Cunningham, E., DeBruijn, G., and Gardner, C. (2013). Computed Tomography and Statistical Analysis of Bubble Size Distributions in Atmospheric-Generated Foamed Cement. Technical Report August.

Kutchko, B., Crandall, D., Moore, J., Gill, M., McIntyre, D., Rosenbaum, E., Haljasmaa, I., Strazisar, B., Spaulding, R., Harbert, W., Benge, G., Cunningham, E., Lawrence, D. W., DeBruijn, G., and Gardner, C. (2015). Field-Generated Foamed Cement : Initial Collection , Computed Tomography , and Analysis. Technical Report July, U.S. Department of Energy, National Energy Technology Laboratory.

Lees, A. and Edwards, S. (1972). The computer study of transport processes under extreme conditions. *Journal of Physics C: Solid State Physics*, 5(15):1921.

Lipton, R. and Avellaneda, M. (1990). Darcy's law for slow viscous flow past a stationary array of bubbles. *Proceedings of the Royal Society of Edinburgh Section A: Mathematics*, 114(1-2):71–79.

Lipton, R. and Vernescu, B. (1994). Homogenisation of two-phase emulsions. *Proceedings of the Royal Society of Edinburgh Section A: Mathematics*, 124(6):1119–1134.

Loeffler, N. (1984). Foamed Cement: A Second Generation. In *Permian Basin Oil and Gas Recovery Conference*.

Marshall, J. and Dayal, K. (2014). Atomistic-to-continuum multiscale modeling with long-range electrostatic interactions in ionic solids. *Journal of the Mechanics and Physics of Solids*, 62:137–162.

Massoudi, M. (2002). On the importance of material frame-indifference and lift forces in multiphase flows. *Chemical Engineering Science*, 57(17):3687–3701.

Massoudi, M. (2003). Constitutive relations for the interaction force in multicomponent particulate flows. *International Journal of Non-Linear Mechanics*, 38(3):313–336.

Massoudi, M. (2008). A note on the meaning of mixture viscosity using the classical continuum theories of mixtures. *International Journal of Engineering Science*, 46(7):677–689.

Massoudi, M. (2010). A mixture theory formulation for hydraulic or pneumatic transport of solid particles. *International Journal of Engineering Science*, 48(11):1440–1461.

Plimpton, S. (1995). Fast Parallel Algorithms for Short Range Molecular Dynamics. *Journal of Computational Physics*, 117(June 1994):1–19.

Pugh, R. J. (1996). Foaming, foam films, antifoaming and defoaming. *Advances in Colloid and Interface Science*, 64(95):67–142.

Rognon, P. G., Einav, I., and Gay, C. (2010). Internal relaxation time in immersed particulate materials. *Physical Review E - Statistical, Nonlinear, and Soft Matter Physics*, 81(6):1–9.

Rognon, P. G., Einav, I., and Gay, C. (2011). Flowing resistance and dilatancy of dense suspensions: lubrication and repulsion. *Journal of Fluid Mechanics*, 689:75–96.

Rognon, P. G. and Gay, C. (2008). Soft Dynamics simulation. 1. Normal approach of two deformable particles in a viscous fluid and optimal-approach strategy. *European Physical Journal E*, 27:253–260.

Rognon, P. G. and Gay, C. (2009). Soft dynamics simulation. 2. Elastic spheres undergoing a T 1 process in a viscous fluid. *European Physical Journal E*, 30:291–301.

Rosenbaum, E., Massoudi, M., and Dayal, K. (2019). Effects of polydispersity on structuring and rheology in flowing suspensions. *Journal of Applied Mechanics*.

Roussel, N. (2005). Steady and transient flow behaviour of fresh cement pastes. *Cement and Concrete Research*, 35:1656–1664.

Sangani, A. and Acrivos, A. (1983). The effective conductivity of a periodic array of spheres. *Proc. R. Soc. Lond. A*, 386(1791):263–275.

Tabakova, S. S. and Danov, K. D. (2009). Effect of disjoining pressure on the drainage and relaxation dynamics of liquid films with mobile interfaces. *Journal of Colloid and Interface Science*, 336(1):273–284.

Tadmor, E. B. and Miller, R. E. (2011). *Modeling materials: continuum, atomistic and multiscale techniques*. Cambridge University Press.

Tan, L., Ye, G., Schlangen, E., and Van Breugel, K. (2007a). Coupling of hydration and fracture models: Failure mechanisms in hydrating cement particle systems. *Particle and Continuum Aspects of Mesomechanics*, pages 563–571.

Tan, L. K., Schlangen, E., and Ye, G. (2007b). Simulation of failure in hydrating cement particles systems. 348:737–740.

Taylor, G. I. (1932). The viscosity of a fluid containing small drops of another fluid. *Proceedings of the Royal Society of London. Series A, Containing Papers of a Mathematical and Physical Character*, 138(834):41–48.

Xiao, Y. (2005). *The influence of oxygen vacancies on domain patterns in ferroelectric perovskites*. PhD thesis, California Institute of Technology.

Chapter 4

Suspensions of Bubbles with a Lognormal Size Distribution

4.1 Abstract

Foamed cement is created by injecting gas into a cement slurry to create a dispersion of bubbles in the cement. The cement is foamed to reduce the density of the cement when a lightweight cement is needed. The size distribution of bubbles from a real foamed cement sample can be determined from analysis of computer tomography images. A pair interaction to simulate bubbles, which accounts for the nature of bubbles by allowing for slip on the bubble surface, the deflection on the bubble surface, and a bubble-bubble pairwise interaction that represents the surfactant physics, was used to simulate the size distribution matching the real foamed cement. It was possible to simulate a realistic bubble size distribution using the bubble interaction. This method can be used to simulate relevant volume fractions of bubbles that represent real foams.

4.2 Introduction

In drilling and completing a well, cement is placed in the annulus between the well casing and the formation to prevent fluid migration and to support the casing. A successful cement job will provide complete zonal isolation (Dusterhoft, 2003; Economides, 1990; Nelson, 1990). Foamed cements are light-weight (low density) cements that have been foamed with an inert gas to form stable slurries with bubbles dispersed throughout. These lower density cements provide the unique properties needed for specific wellbore environments (Benge et al., 1996; Bour and Rickard, 2000; Frisch et al., 1999; O'Rourke and Crombie, 1999; White et al., 2000). The conditions under which foamed cements are produced and pumped into the well make them difficult to study experimentally, especially when establishing the effects of flow on the physical properties of the set cement. During flow, the bubbles will re-arrange and can cluster or structure relative to the direction of flow. An increased propensity of the bubbles to structure could cause channels to form in the set cement, allowing fluid migration, or crack initiation in the cured cement sheath that provides support to the well casing.

One of the primary purposes of well cement is to provide zonal isolation. Foamed cement permeability is affected by the amount of gas dispersed in the cement and the configuration of the bubbles. If the permeability is too high, the cement will not be able to provide zonal isolation. One way to study the expected ability of the foamed cement to prevent fluid migration is to predict whether the configuration of bubbles is expected to form any structuring where the bubbles could become connected after curing and allow pathways for fluids to migrate.

Laboratory tests designed to determine the foamed cement slurry stability and other physical benchmarks are done at bench scale and produced by foaming the cement in a blender (API 10B-4, 2004) under atmospheric conditions. The gas added to the cement is the air remaining in the blender container and the stacked blade configuration disperses the air and shears it to diperse the air as bubbles in the cement. In field applications, the cement is typically foamed by high-pressure ni-

trogen gas injection through an atomizer at much higher shearing rates. The bubbles produced by these two processes are quite different in terms of size, the size distribution, and bubble configurations. Blender made cements produce bubbles that are significantly larger in size [when compared to field cements] and increase in size with foam "quality" (cementing industry term for volume fraction of bubbles added to the cement) (Kutchko et al., 2013). While field cements have similar sized bubbles across all qualities, they contain more bubbles as quality increases (Kutchko et al., 2015). The differences in the size and quantity of the bubbles between the laboratory prepared test cements and the field applications is due to their two different production methods.

To study the influence of flow on the bubble arrangements, simulations can be used instead of deploying elaborate experimental setups. To avoid system size effects on the results, simulations can contain a very large number of bubbles (60,000 or more). To analyze the effects of flow with these simulations therefore becomes difficult because you can no longer visually observe bubble structuring due to flow. Additionally, the data from the samples that have been collected with computer tomography (CT) scanner imaging can contain similar numbers of bubbles or magnitudes more. We use an analysis to identify the clusters or structures of bubbles in more quantitative manner.

4.3 Real Foamed Cement Samples and Analysis

Foamed cement samples produced with three different methods has been done previously and the analysis of these foamed cement samples is shown in (Dalton et al., 2018; Kutchko et al., 2013, 2015).

The laboratory testing method used by the American Petroleum Institute (API) in the recommended testing practices (API 10B-4, 2004) uses a laboratory blender that is specially designed for mixing cement. The blender has a stacked blade configuration to shear the air into the cement. The foamed cement is made by mixing the cement, water, surfactants, and additives as described in the API

recommended practices. The cement is made in batches and the amount of air added is determined by the amount of empty space in the blender above the cement mixture. The size of the entrained bubbles is a function of the amount of gas added. So the higher the volume fraction of added air, the larger the bubbles.

Foamed cement samples were also collected in several yard tests as part of a collaborative industry project. The equipment used in field applications was used to collect samples under pressure and cured undisturbed under pressure. Once cured the samples were then transported to the National Energy Technology Laboratory in Morgantown, WV for further analysis. The field cements captured with the industry equipment in the yard test represents the foamed cement before being pumped into a well. The yard tests were performed by three different service companies. Foamed cement in field applications is made by first batch mixing the cement, water, surfactants, and additives. As the cement is flowing, nitrogen is injected by an atomizer to create bubbles that are 100s of microns in size.

Another method for creating a representative field foamed cement in the lab can be done with a specially designed foamed cement generator (de Rozières and Ferrière, 1991). The laboratory generator consists of a pressure vessel and tubing with a special vessel that can be closed off from the rest of the flow loop to capture the pressurized foamed cement sample. The pressure vessel has two chambers and an air actuated piston. The top chamber contains the air to move the piston and the bottom chamber is where the cement is place and subsequently foamed. The cement, surfactants, and other additives are first mixed in a blender and then placed in the bottom chamber. During a cycle, cement is drawn into the lower chamber when the piston is pushed down and then is forced through an orifice, with a flapper to increase foaming, as the piston is pushed up. The foamed cement is cycled through the tubing and the collection vessel. The foaming occurs when the cement is forced through the orifice.

Because the samples collected during the industry yard tests best represents a foamed cement used in a wellbore application, the focus here will be on the samples collected in the field.

4.3.1 Foamed Cement Field Sample Computer Tomography Scanning and Segmentation

Computer tomography (CT) scanning was performed on the field samples that were collected from the industry yard tests and the tests are described in (Kutchko et al., 2015). The CT images were then analyzed for quantitative information about the bubbles' sizes and is described in an internal report (Mathis, 2016). To quantify the bubbles, first a threshold is performed on the grayscale images to specify what pixels are bubbles and what constitutes cement. Thresholding is an important step and must be done properly or the bubbles can be over estimated or underestimated. A single threshold value used on all areas of the CT images can produce errors in the overall analysis, especially when the bubbles vary significantly in size and the small bubbles approach the pixel size. A Phansalkar (Phansalkar et al., 2011) auto local threshold included in ImageJ Fiji (Schindelin et al., 2012) produced realistic thresholding of the images and captured the correct size of both the large and very small bubbles. The Phansalkar method uses a local threshold value in a spherical shaped region. After the images have been thresholded, the images consist of pixels that are assigned to be either part of a bubble or the cement background. The result is binary images. During the thresholding process, due to the proximity of some bubbles and the limits of the scan resolution, the bubbles can appear to be connected so they needed to be separated with a segmentation process. A 3 dimensional watershed segmentation plugin in ImageJ (Ollion et al., 2013), a Euclidean Distance Transform, was used to separate the bubbles. Then the bubbles can be quantified with a volume and a position (in the x, y, and z directions). The volume of each bubble can be determined by the volume of the total number of voxels (a pixel volume). The accuracy of the volume is a function of the resolution of the CT image scan. An ImageJ 3D object counter plugin (Bolte and Cordelieres, 2006) was used to catalog the volume and position of each bubble in the image. With this data, the bubbles can be analyzed quantitatively.

The bubbles in the CT images were qualitatively spherical and were assumed to be perfectly spherical to convert the volumes to a radius for each bubble. The bubbles' sizes fit a lognormal size

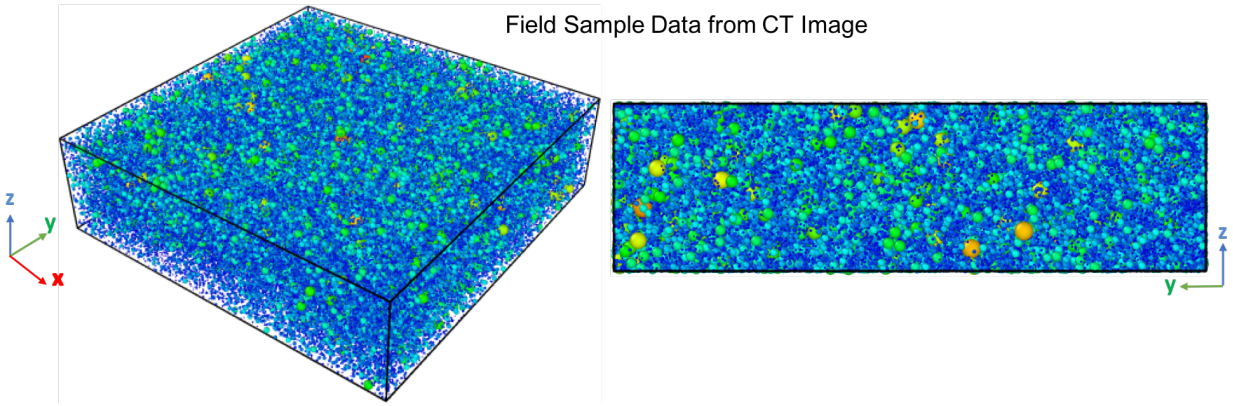

Figure 4.1: The idealized spherical bubbles are determined from the CT images of the field sample.

distribution. The data from all three yard tests fit a lognormal size distribution. Because the third yard test was performed based on lessons learned from the first two, the sample from this test was chosen for creating the simulation inputs. The spherical bubbles' sizes and positions determined from the CT images is shown in Figure 4.1. The histogram of the bubble sizes from Figure 4.1 is shown in Figure 4.2. The data was fit to a lognormal size distribution to determine the mean, $\mu_{lognormal}$, and standard deviation, $\sigma_{lognormal}$, of the fit. The same mean and standard deviation can then be used to create simulation inputs.

4.4 Simulation Inputs with a Lognormal Size Distribution

The size distribution of the bubbles in real foamed cement samples have a lognormal size distribution but the volume fraction of the samples that can be collected from real foamed cement equipment is limited. There are also many complications and a huge expense in collecting foamed cement samples with field equipment. To obtain samples at different volume fractions we can create inputs of bubble configurations at different volume fractions for simulations. The distribution of the bubble sizes is the same as the field samples but the inputs can be made at different volume fractions. The volume fraction of bubbles in the field sample shown in Figure 4.1 is around 11%, which is lower than an average foamed cement target value.

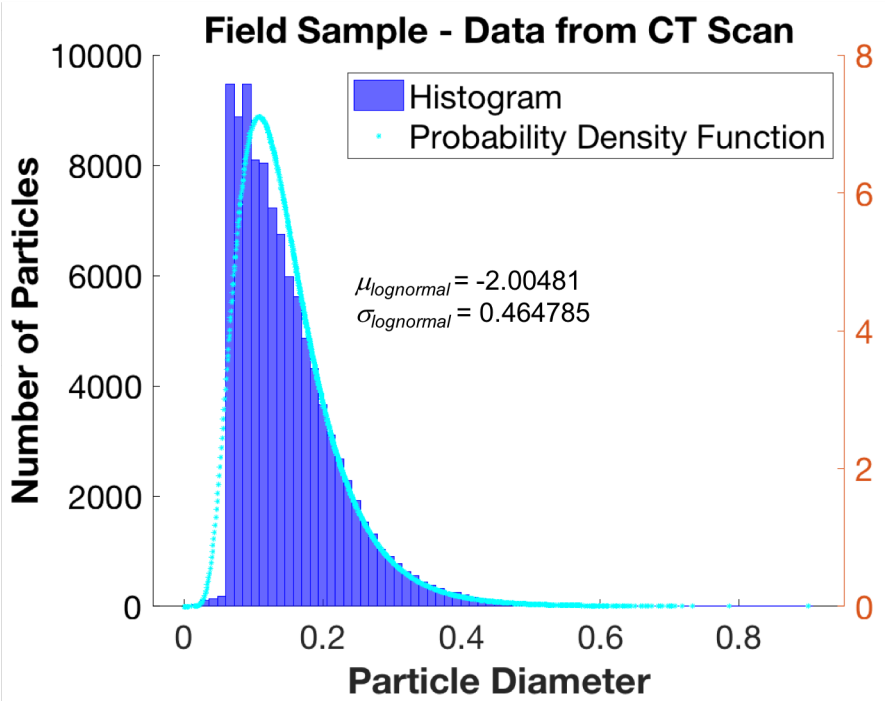

Figure 4.2: The bubble size distribution of one of the yard tests is shown along with the probability density function for a lognormal distribution. The values of $\mu_{lognormal}$ and $\sigma_{lognormal}$ for a lognormal distribution were found for the fit of the data to the probability function.

To create the simulation inputs, first the bubble sizes from the lognormal size distribution were re-scaled to be within a range of 0 to 1 so that simulation inputs could be created at reasonable overall sizes. The mean value and standard deviation used to create the lognormal size distribution is from the real size distribution of the foamed cement shown in Figure 4.2. The bubble sizes are re-scaled but the mean and standard deviation is the same as the real sample.

To produce a 27% volume fraction of bubbles as an input, the distribution of the sizes was determined first and assuming a simulation box size of $5 \times 5 \times 5$, the bubbles were then placed in the simulation box. A Monte Carlo method was used to randomly place the bubbles in the box. To make the process faster and to make sure that a volume fraction of 27% bubble volume fill could be achieved, a smaller simulation box size was used. Other methods must be employed to create higher volume fractions or larger simulation box sizes. A Monte Carlo method is an efficient method for placing particles in random arrangements and the majority of the particles can be placed

quickly and easily but as the space in the simulation box is used up by the bubbles, it becomes more and more difficult to place the bubbles in the box. For this reason, the smaller initial simulation box size was chosen. To eliminate the effects due to the limited simulation input size, the $5 \times 5 \times 5$ simulation box was replicated 8 times in the x, y, and z-directions. The input simulation box size is then $40 \times 40 \times 40$.

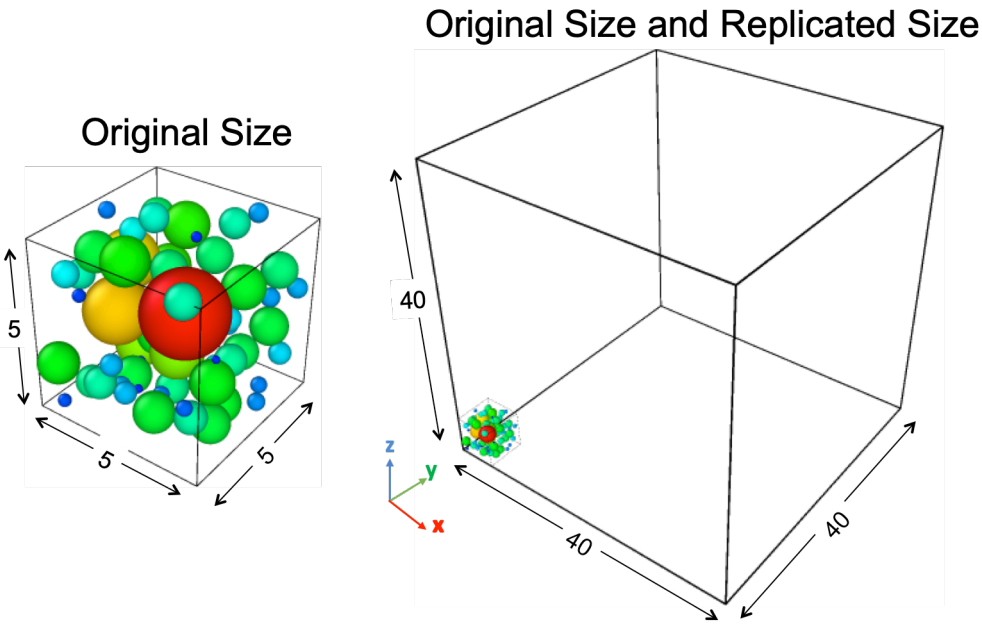

Figure 4.3: The lognormal size distribution of bubbles was first determined and then placed randomly in the $5 \times 5 \times 5$ simulation box. To reduce the effects of the simulation size, the original $5 \times 5 \times 5$ simulation box was replicated 8 times in each direction.

4.5 Methods: Simulating Bubbles in Suspension

Simulations of monodisperse bubbles was described in Chapter 3. Similar same pair interaction and the same methods were used to simulate polydisperse bubble size configurations with realistic lognormal bubble size distributions. The pair interaction was modified so that bubbles with different sizes could be simulated. The force between the bubbles is a combination of the squeezing flow force, the elastic quality of the bubble surface that allows the surface to deflect locally, and a

direct force to represent the surfactants added. It is assumed that the bubble surface has sufficient slip so that there is no shearing resistance. The total normal force on the bubble surface between interacting pairs is therefore described by:

$$\boldsymbol{F}^{Total} = \boldsymbol{F}^{Bubble} + \boldsymbol{F}^{Elastic} + \boldsymbol{F}^{Direct} \tag{4.5.0.1}$$

4.5.1 Near-Field Bubble Interactions: Bubble Squeeze Force

The velocity profile of a Newtonian fluid being squeezed from between the hard spheres has a parabolic shape. However, a bubble surface boundary has an extra slip velocity as depicted in Figure 3.2. The velocity profile of the fluid between the interacting drops and bubbles is the sum of the parabolic velocity, u_p, and the additional slip velocity, u_t, due to the drop surface (Davis et al., 1989; Kim and Karrila, 2005):

$$v(x,z) = u_t(x) + u_p(x,z) \tag{4.5.1.1}$$

The parabolic velocity profile of the fluid that is squeezed out from between hard spheres with no-slip boundaries is given by the expression (Kim and Karrila, 2005):

$$u_p(x,z) = \frac{1}{2\mu}\frac{\partial p}{\partial x}(z - z_a)(z - z_b) \tag{4.5.1.2}$$

Where z_a and z_b are the surfaces of the two spheres a and b, respectively, μ is the viscosity of the base fluid, and $\frac{\partial p}{\partial x}$ is the pressure gradient in the x direction. When the distance between the bubble surfaces is small compared to the bubble radii, the surfaces can be approximated as flat disks and the surface traction is then given by (Kim and Karrila, 2005):

$$f_t = -(z_a - z_b)\frac{\partial p}{\partial x} \tag{4.5.1.3}$$

If μ is the viscosity of the base fluid, then by convention $\lambda\mu$ is defined as the viscosity of the drop

or bubble. For very viscous drops λ is $\gg 1$, for drops with a low viscosity λ is $\ll 1$, and for a bubble, $\lambda = 0$. The traction boundary condition at the base fluid - bubble interface is (Kim and Karrila, 2005):

$$\mu \frac{\partial u_p}{\partial z} = \lambda \mu \frac{\partial v}{\partial z} \tag{4.5.1.4}$$

The relationship between the force and velocity for approaching bubbles and squeezing flow is (Kim and Karrila, 2005):

$$\frac{F_i}{6\pi\mu\alpha U_i} = \frac{1}{3}\log\frac{\alpha}{h} + \frac{2}{3}(\gamma_{Euler} + \log 2) + O(1) \tag{4.5.1.5}$$

where γ_{Euler} is Eulers constant (γ_{Euler} = 0.577216), here we define the relationship between the bubble sizes as $\alpha = \frac{ab}{a+b}$ (Davis et al., 1989; Kim and Karrila, 2005), and h is the gap between the bubbles. This can then be rearranged to solve for the force, F_i, as a function of velocity, U_i, so that the remaining terms on the right become the resistance "squeeze" coefficient for a bubble, which is similar to the a_{sq} coefficient derived by Ball and Melrose (Ball and Melrose, 1997). The force of bubble i is then:

$$F_i^{Bubble} = 6\pi\mu\alpha U_i \left(\frac{1}{3}\log\frac{\alpha}{h} + \frac{2}{3}\left(\gamma_{Euler} + \log 2\right)\right) \tag{4.5.1.6}$$

Equation (4.5.1.6) describes the normal force acting on bubble i, and therefore a_{sq}^{Bubble} is given by:

$$a_{sq}^{Bubble} = \pi\mu\alpha \left(2\log\frac{\alpha}{h} + 4\left(\gamma_{Euler} + \log 2\right)\right) \tag{4.5.1.7}$$

A more accurate approach to deriving the force between bubble pairs could be solved using the equations derived in (Davis et al., 1989; Kim and Karrila, 2005) but to decrease the computation time, the simple relationship between the bubble sizes was used. The more polydispersity in the bubble input sizes, the greater the computation time.

4.5.2 Near-Field Bubble Interactions: Elastic Force

As noted previously in Chapter 3, an elastic force is used to model the deflection of the bubble surface due to the impingement of another bubble. The elastic force derivation follows (Rognon et al., 2010):

$$\boldsymbol{F}^{Elastic} = a_{Elas} E \delta \tag{4.5.2.1a}$$

$$a_{Elas} = \sqrt{\alpha(2h + |\delta|)} \tag{4.5.2.1b}$$

$$\delta = \frac{(a + b + h - r)}{2} \tag{4.5.2.1c}$$

Here, δ is the deflection of the bubble surface (Figure 3.5), a_{Elas} is the region of the bubble surface that is interacting in the lubrication force after deflection has caused the surface to become flattened, and E represents an *effective* modulus to deform the interface and bubble. In the simulations shown here, E was set to 10^2; this could in principle be calibrated to experiment. To limit the amount that the bubble surface can deflect, a maximum deflection value was set.

4.5.3 Near-Field Bubble Interactions: Direct Force

The direct force is necessary to keep the bubbles from overlapping completely during the simulation. It represents the force due to the surfactant, which can be attractive and repulsive (Tabakova and Danov, 2009) depending on the properties of the surfactant and the separation of the bubbles. The surfactant forces can include van der Waals and hydrostatic attraction, electrostatic repulsion, steric repulsion, etc. (Tabakova and Danov, 2009), however, the properties of the surfactant are not the focus of this research at this time and are not generally known because it is proprietary information. Therefore, no specific surfactant properties were used. Herein, the direct force is represented by a Lennard-Jones potential force that acts normal to the bubble surface along the line between the center of interacting bubble pairs. Rognon and Gay (Rognon and Gay, 2008, 2009) developed soft

dynamics to simulate dense collections of elastic particles. Soft dynamics can only simulate closely interacting particles and a confining stress is used to keep the suspension in a dense configuration. Rognon, Einav, and Gay (Rognon et al., 2010, 2011) include a direct force that represents the steric repulsion between elastic particles. It increases steeply when the particles come in close contact and prevents the particles from overlapping during the simulation. In the simulations shown here, a direct force is deployed in a similar way. The Lennard-Jones potential included with LAMMPS (LAM, 2003) was used as the direct force.

The Lennard-Jones potential is based on van der Waals interactions (Rognon et al., 2010, 2011) and includes both repulsive and attractive forces. A Lennard-Jones potential that was less repulsive than the standard Lennard-Jones potential was used here and is given by (LAM, 2003):

$$\phi_{LJ} = 4\epsilon \left[\left(\frac{\sigma}{r}\right)^9 - \left(\frac{\sigma}{r}\right)^6 \right] \tag{4.5.3.1}$$

ϵ is the energy scale and σ is the length scale. The influence of the values of ϵ and σ on systems dynamics were described in Chapter 3. The values of ϵ and σ used are 0.008 and 0.9, respectively, and based on the analysis shown in Chapter 3. $\left(\frac{\sigma}{r}\right)^9$ is the repulsive part[1] and $\left(\frac{\sigma}{r}\right)^6$ is the attractive portion. The direct force, F^{Direct}, between bubbles is then the derivative of Equation (4.5.3.1). Here, this force keeps the bubbles from overlapping completely during simulations but also allows for the elastic interaction.

4.5.4 Performing Simulations

The shearing flow was implemented as described in (Rosenbaum et al., 2019). Three dimensional simulations were performed using Lees-Edwards boundary conditions (Lees and Edwards, 1972). For Lees-Edwards boundary conditions and strains imposed in the xy-direction, the velocity of each particle is then a function of its position in the y-direction as shown in Figure 4.4. When a

[1]The standard Lennard-Jones potential is $\phi_{LJ} = 4\epsilon \left[\left(\frac{\sigma}{r}\right)^{12} - \left(\frac{\sigma}{r}\right)^6 \right]$

particle crosses the simulation boundary in any direction, the velocity of the particle is remapped to correspond to the new position in the simulation box[2]. The suspension was sheared until the stress reached a constant value and the value of $\dot{\gamma} \times t_{total}$ reached 200. t_{total} is the length of time that the simulation was run. A timestep of $\Delta t = 0.0001$ was used. For monodisperse bubbles, a $\Delta t = 0.001$ did not produce any errors or loss of bubbles, however, for the dynamics to work properly, the smaller timestep was necessary.

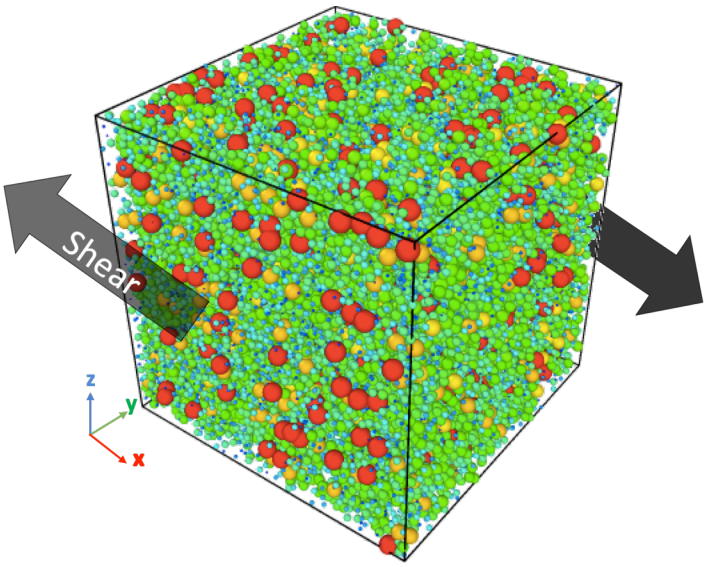

Figure 4.4: The lognormal simulation input created with the same mean and standard deviation from a foamed cement sample were sheared in the direction indicated.

The total strain on the simulation box is defined as $\dot{\gamma} \times \Delta t$, the product of the strain rate $\dot{\gamma}$ and timestep Δt. For the quasi-static setting, given $\dot{\gamma} \times \Delta t$, the time-history of the stress and viscosity should be the same when time is appropriately re-scaled.

[2]See e.g. (Dayal and James, 2010) for a discussion of this and (LAM, 2003) for the implementation, which uses a function called "fix deform" to apply a strain rate to the simulation box in the specified orthogonal box directions.

4.6 Results

Here the results of simulations of polydisperse bubbles are shown. The same slightly polydisperse inputs of size and location from Chapter 2 were used as inputs to simulations using the bubble interaction described in this Chapter. An input of 27.4% of bubbles by volume with a lognormal bubble size distribution, that represents a real foamed cement bubble size distribution, was also simulated with the bubble interaction. The lognormal input, with the same mean and standard deviation from the lognormal bubble size distribution taken from a real foamed cement sample, is described in Section 4.4. Ideally, the bubbles' sizes and locations from the whole foamed cement sample could be used as simulation inputs but with the interactions and methods described here, the real sample is too complex to make this impossible at this time. This is something that is part of current and ongoing research. A simplified input that represents a real foamed cement was used instead to test the bubble interaction. The bubble sizes fit a lognormal distribution but the initial simulation box size is made smaller and then replicated to obtain the larger simulation input.

In Chapters 2 and 3, the results of mono- and polydisperse hard spheres and monodisperse bubbles, respectively, were shown. As was done previously, to obtain the larger system size, the smaller simulation box was replicated in the x, y, and z directions. The particles and bubbles that were simulated previously either did not have different size inputs or the sizes varied only slightly. For the slightly polydisperse particles, only four different particle sizes were used. Because the sizes were so similar and there was little variation in the sizes included, it was possible to push around the particles after replicating the original simulation input. However, when the bubbles vary in more realistic sizes, the same methods to mix the initial configuration and make it fully random did not work to randomize the lognormal bubble size distribution.

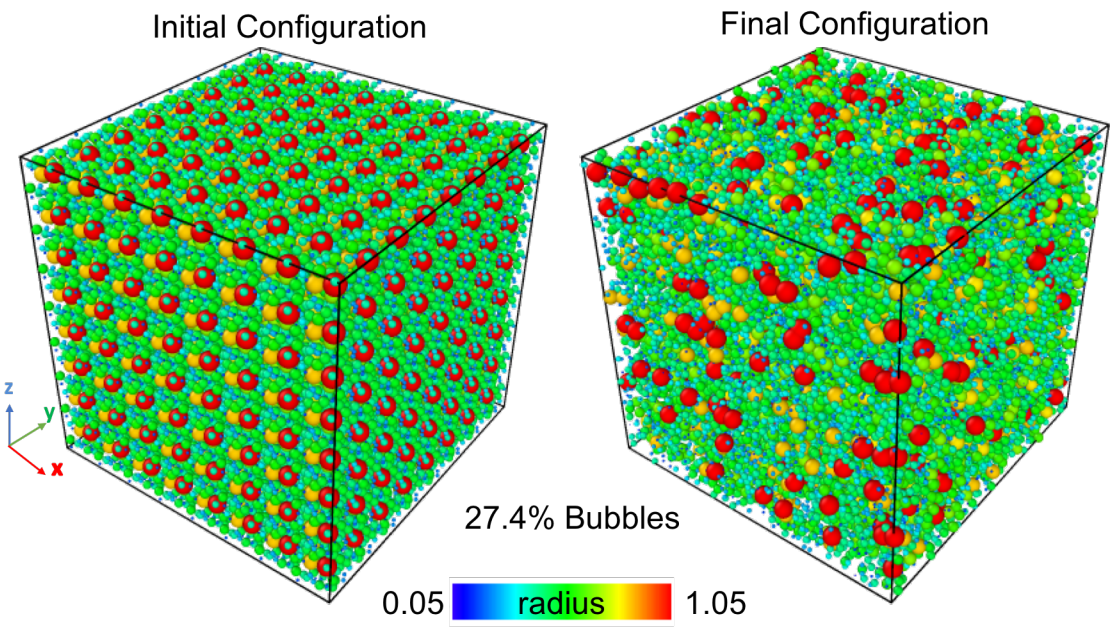

Figure 4.5: The initial configuration of the bubbles is the replicated $5 \times 5 \times 5$ simulation box shown in 4.3. The final configuration shows the configuration of the bubbles after the simulation box was strained to a value of 200. The color corresponds to the size of the bubbles.

4.7 Configurations of Bubbles Due to Flow

Figure 4.5 and Figure 4.6 show the initial and final configurations of the bubbles. The smaller simulation box shown in Figure 4.3 was replicated 8 times in each direction so that the initial simulation box and simulation input was $40 \times 40 \times 40$. The pattern of the bubbles of the initial configuration in Figures 4.5 and 4.6 is due to the replication process and no mechanism to randomize the initial configuration of the bubbles. Figures 4.5 and 4.6 show the final configuration of the bubbles after straining the simulation box to a value of 200. The color of the bubbles corresponds to the bubble size. In the final configuration shown in Figure 4.6, it can be observed that the bubbles are grouped by size along the x-axis after shearing.

An analysis of the neighbors surrounding each bubble can show regions of localized bubble clustering. When a large number of bubbles is simulated, it may be difficult to identify quantitatively when clustering of bubbles has occurred due to shearing. The neighbor analysis considers each

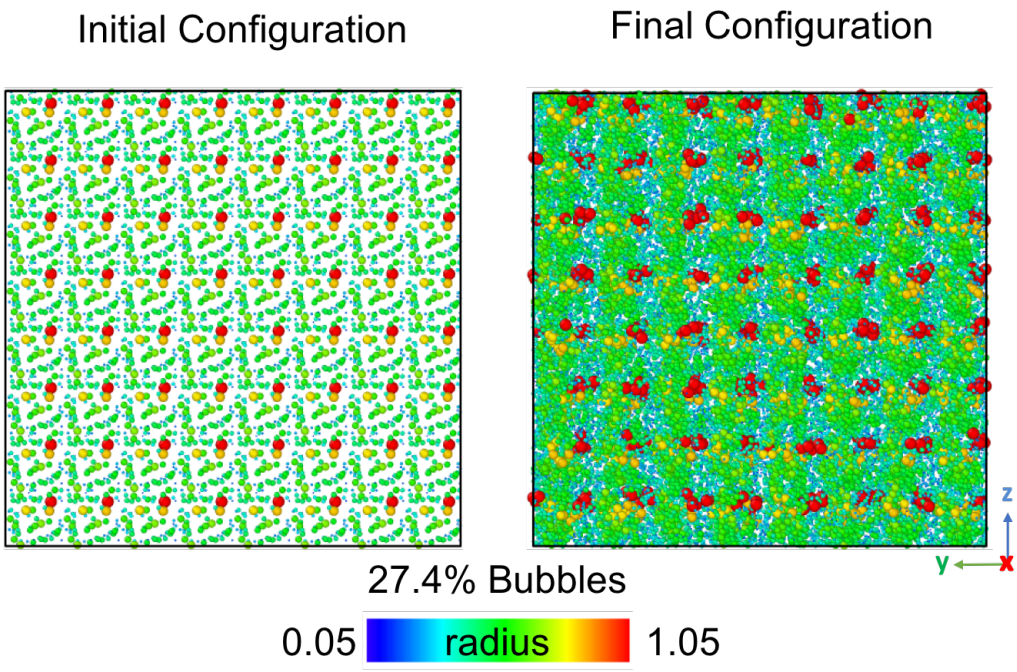

Figure 4.6: The initial configuration of the bubbles is the replicated $5 \times 5 \times 5$ simulation box shown in 4.3. The final configuration shows the configuration of the bubbles after the simulation box was strained to a value of 200. The color corresponds to the size of the bubbles. The bubbles are shown at half their size from the side view, looking through the whole sample.

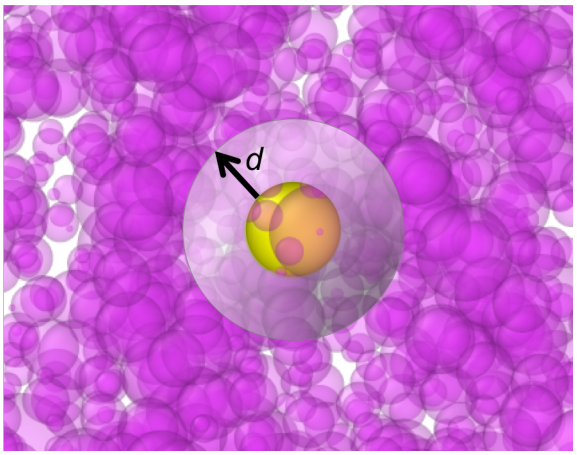

Figure 4.7: The particle highlighted in the center shows the spherical radius, d, around the particle that would be used to count the neighbors.

bubble individually and uses a sphere around each bubble and considers all other bubbles within this sphere as a neighbor (Figure 4.7). The value of the radius, d, around each bubble is used to

count the number of neighbors. The neighbor analysis considers the periodic boundaries of the simulation box and bubbles across the boundaries that are within the radius are also counted. This eliminates errors at the simulation box boundaries. The bubbles are counted as neighbors if $d_{i,j} < d$. The value of $d_{i,j}$ for each bubble i is calculated as follows:

$$d_{i,j} = \sqrt{(x_j - x_i)^2 + (y_j - y_i)^2 + (z_j - z_i)^2} - radius_j - radius_i \tag{4.7.0.1}$$

The neighbor analysis of the slightly polydisperse bubbles is shown in Figures 4.8 and 4.9. The range of color coding of the neighbors corresponds to a range of 0 to 15. As the volume fraction of bubbles increases and the simulation inputs become denser, the number of neighbors of each bubble also increases. In the results shown here, the 47.4% by volume of bubbles has the most neighbors but does not have any evident structuring of the bubbles (Figure 4.9).

The results of the neighbor analysis of the lognormal bubble size simulation are shown in Figures 4.10 and 4.11. In Figure 4.11, the bubbles are shown at half size to observe any structuring. No structuring is observed in the projected view and only several bubbles have neighbors at the high end of the scale, despite the grouping by bubble size that observed in Figure 4.6. The bubbles with the lognormal size distribution do not have a noticeable difference in the number of neighbors compared to the slightly polydisperse bubbles.

4.8 Relative Viscosity

The relative viscosity of the slightly polydisperse particles and bubbles is shown in 4.12. The relative viscosity was calculated with 3.5.2.2. The viscosity of polydisperse bubbles is lower than the viscosity of the same volume fractions of particles. This can be explained by the ability of the bubbles to slide by each other and the localized deflection of the bubbles.

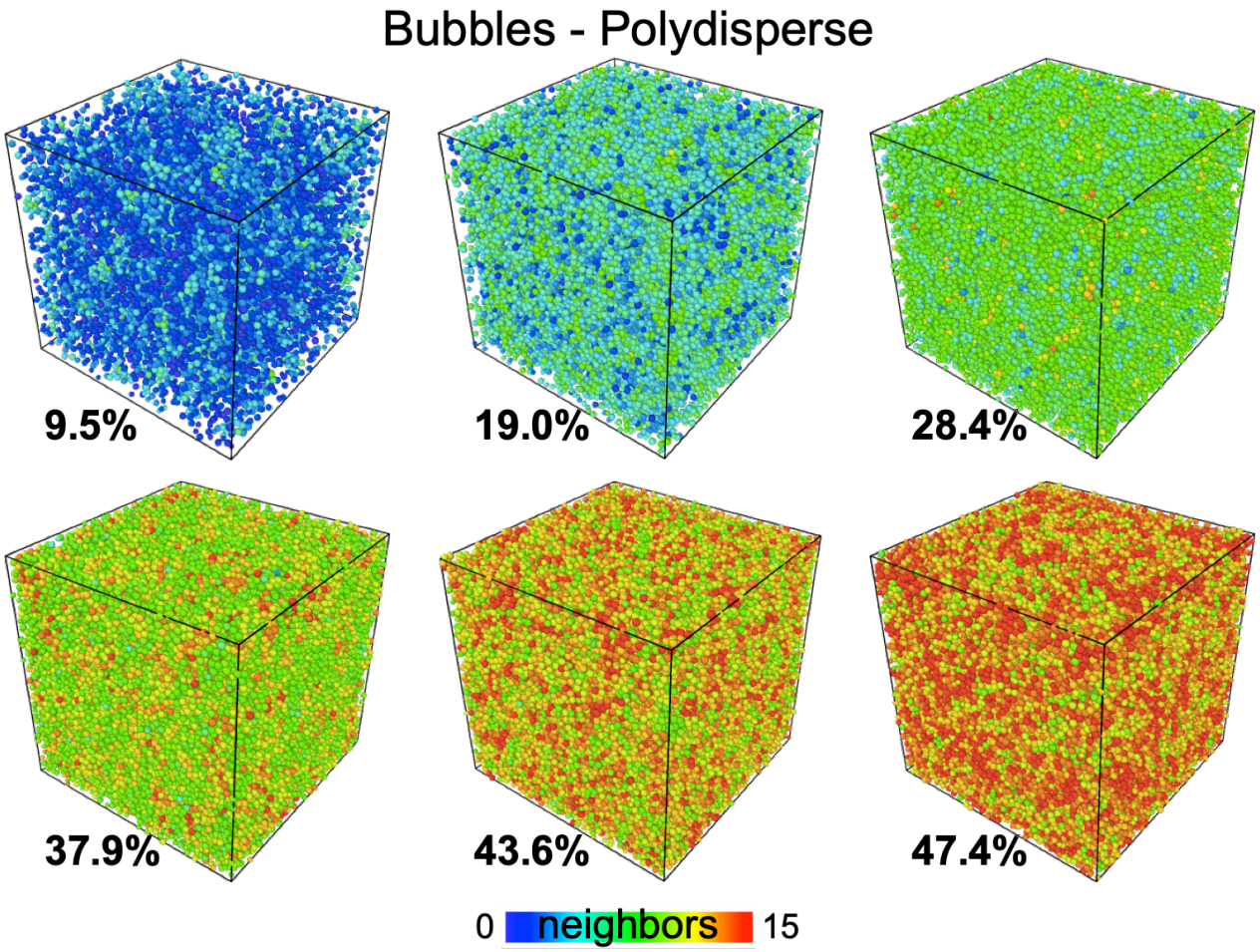

Figure 4.8: Simulation results of slightly polydisperse bubbles with slip surface boundaries simulations at 9.5%, 19.0%, 28.4%, 37.9%, 43.6%, and 47.4% by volume of particles. The size distribution is shown in Figure 2.3. The particles are shown at the final configuration after the box was strained to a value of 200.

4.9 Discussion

It has been shown here that bubble size distributions representing those of a real sample can be simulated. The bubble interaction allows for polydisperse bubbles and accounts for slip on the surface, the lack of shearing resistance, and allows the bubble surface to deflect a small amount. The result is that interacting bubble pairs can pass by each other with less restriction and less jamming of the bubbles. With application to foamed cements, the bubbles should remain dispersed throughout the cement slurry during flow and placement in the well. As shown in (Rosenbaum et al., 2019),

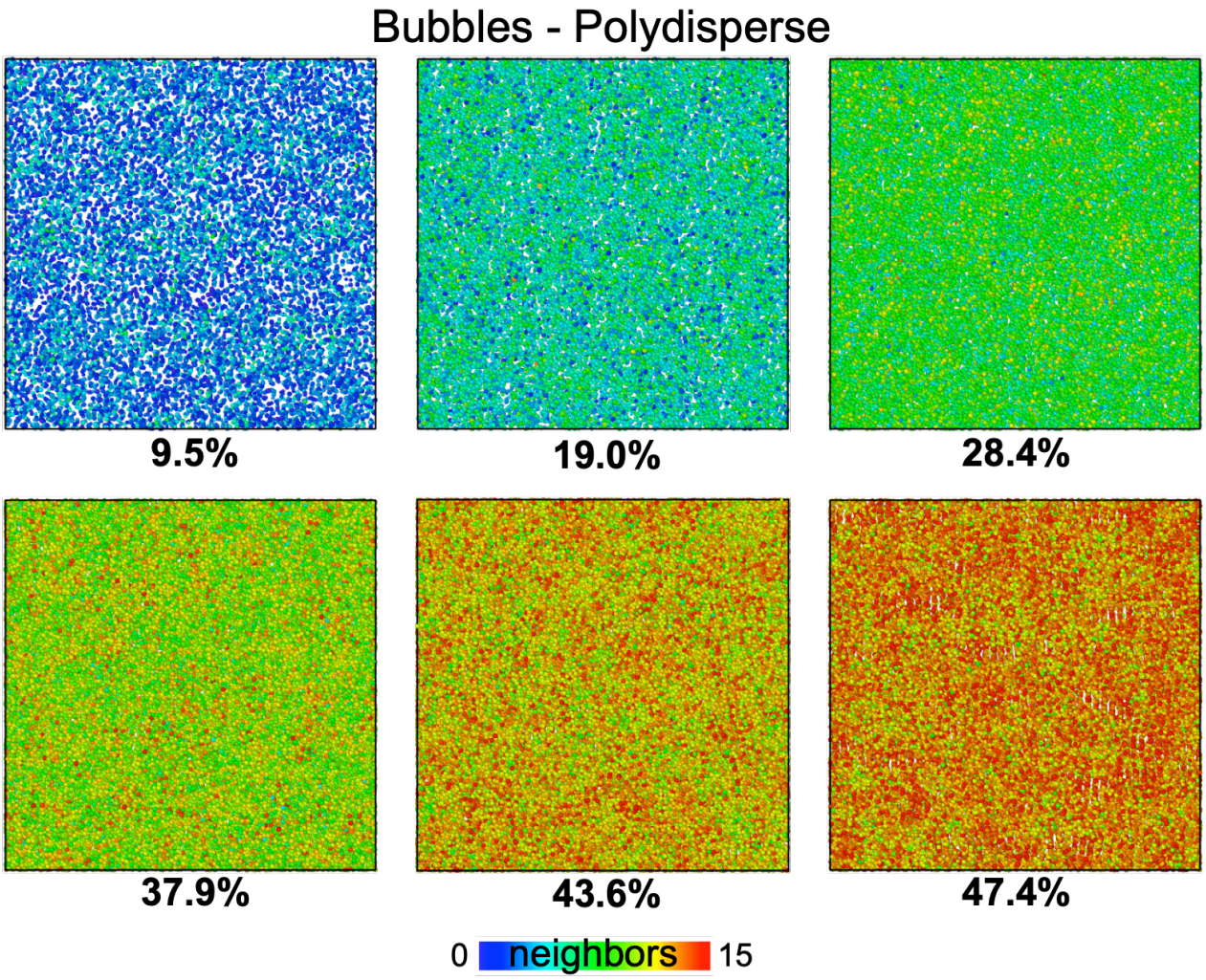

Figure 4.9: Simulation results of slightly polydisperse bubbles with slip boundaries simulations at 9.5%, 19.0%, 28.4%, 37.9%, 43.6%, and 47.4% by volume of particles. The size distribution is shown in Figure 2.3. The particles are shown at the final configuration after the box was strained to a value of 200. The particles are shown at half their size from the side view, looking through the whole sample.

the polydispersity of the particle sizes helped to reduce particle clustering. The use of bubble slip boundary conditions also reduces the particle clustering/structure forming in comparison to particles modeled with no-slip boundary conditions. It was expected that the combination of bubble surface properties with polydispersity in the bubbles sizes would reduce the propensity for bubble clustering to occur. In application, it is difficult to create bubble dispersions of exactly equal bubbles so in actual foamed cement, the polydispersity of the bubbles in the foamed cement help to keep

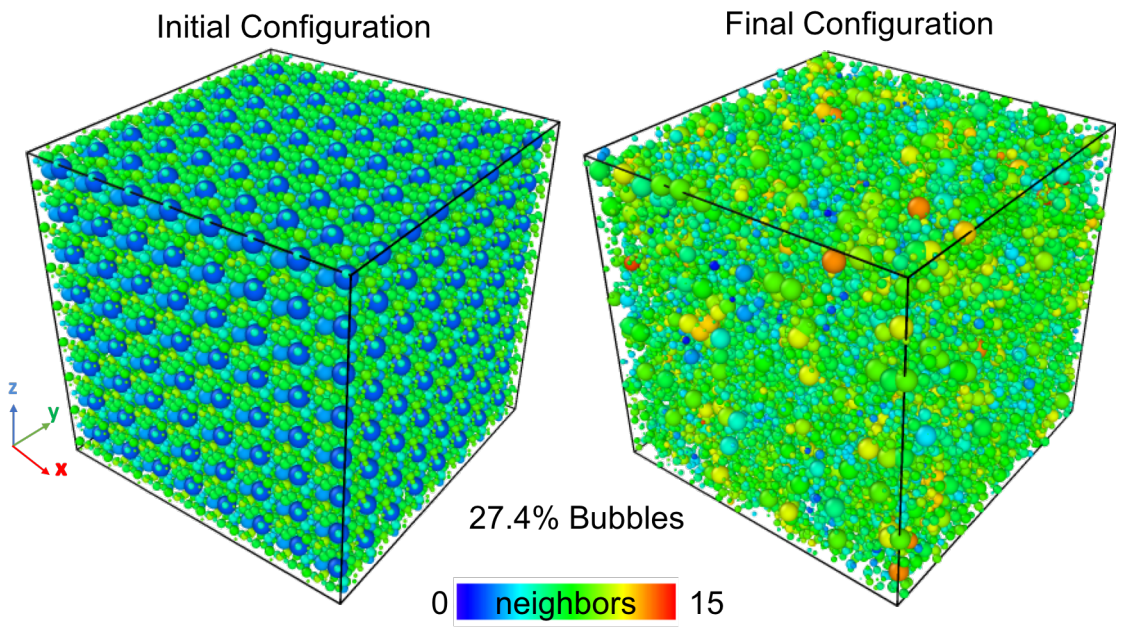

Figure 4.10: Simulation results of lognormal bubble simulations at 27.4% by volume of particles. The particles are shown at the final configuration after the box was strained to a value of 200.

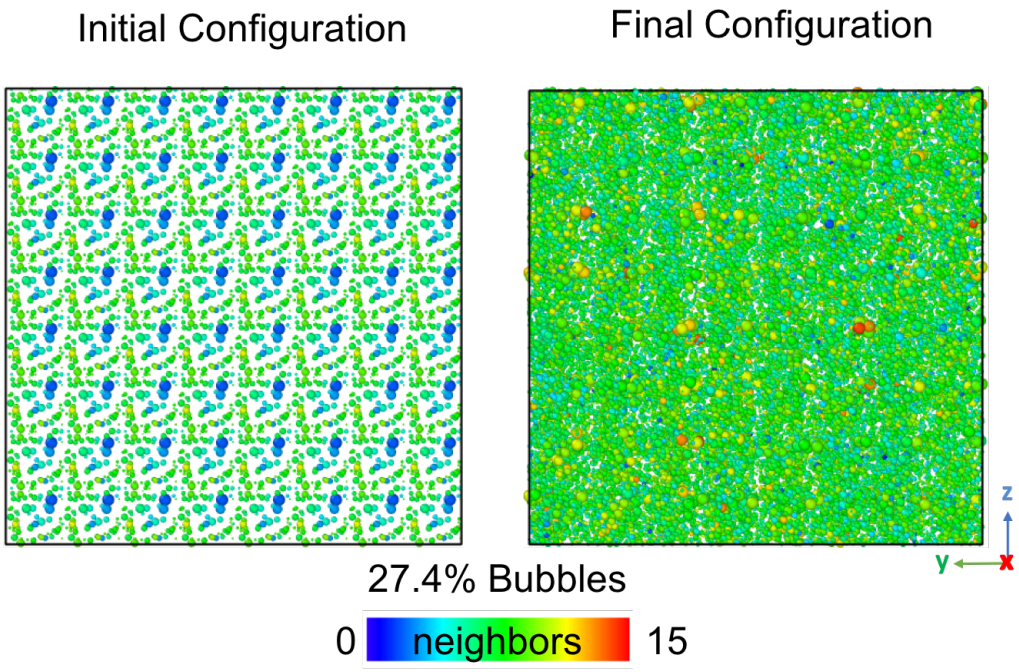

Figure 4.11: Simulation results of lognormal bubble simulations at 27.4% by volume of particles. The particles are shown at the final configuration after the box was strained to a value of 200.

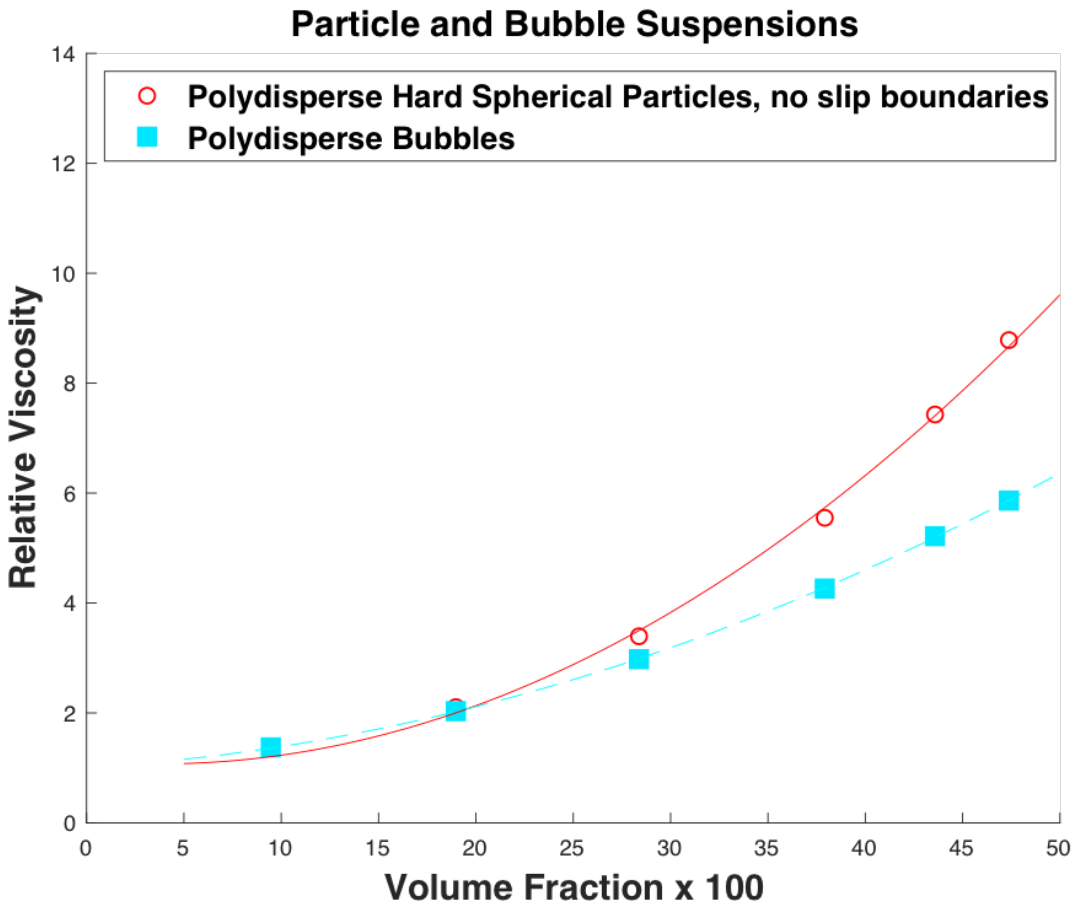

Figure 4.12: The relative viscosity or viscosity ratio is shown as a function of the volume fraction of particles/bubbles in the suspension. The lines in the figures are second order polynomial fits through the calculated relative viscosity points shown and including the point $(0, 1)$.

the bubbles dispersed. The viscosity increases due to the addition of the bubbles, however, the viscosity does not increase as much at volume fractions of 30% and higher. So, the expected increase in viscosity should be based on models that consider the properties of the bubble for the suspended spheres.

4.10 Chapter 4 References

Bibliography

(2003). *LAMMPS Users Manual*. Sandia National Laboratories.

API 10B-4 (2004). Recommended Practice on Preparation and Testing of Foamed Cement Slurries at Atmospheric Pressure ANSI / API Recommended Practice 10B-4. Technical Report July.

Ball, R. C. and Melrose, J. R. (1997). A simulation technique for many spheres in quasi-static motion under frame-invariant pair drag and Brownian forces. *Physica A: Statistical Mechanics and its Applications*, 247(1-4):444–472.

Benge, O. G., McDermott, J. R., Langlinais, J. C., and Griffith, J. E. (1996). Foamed cement job successful in deep HTHP offshore well. *Oil and Gas Journal*, 94.

Bolte, S. and Cordelieres, F. (2006). A guided tour into subcellular colocalization analysis in light microscopy. *Journal of microscopy*, 224(3):213–232.

Bour, D. and Rickard, B. (2000). Application of Foamed Cement on Hawaiian Geothermal Well. *Geothermal Resources Council Transactions*, 24.

Dalton, L. E., Brown, S., Moore, J., Crandall, D., and Gill, M. (2018). Evolution Using CT Scanning : Insights From Elevated-Pressure Generation. (January):1–11.

Davis, R. H., Schonberg, J. a., and Rallison, J. M. (1989). The lubrication force between two viscous drops. 77(1989).

Dayal, K. and James, R. D. (2010). Nonequilibrium molecular dynamics for bulk materials and nanostructures. *Journal of the Mechanics and Physics of Solids*, 58(2):145–163.

de Rozières, J. and Ferrière, R. (1991). Foamed-Cement Characterization Under Downhole Conditions and Its Impact on Job Design. *SPE Production Engineering*, (August):297–304.

Dusterhoft, D. M. (2003). Foamed & Lightweight Cements. pages 1–12.

Economides, M. J. (1990). 1. Implications of Cementing on Well Performance. In Nelson, E. B., editor, *Well Cementing*, chapter 1, pages 1.1 – 1.6. Schlumberger Educational Services, Sugar Land, Texas.

Frisch, G. J., Services, H. E., and Graham, W. L. (1999). SPE 55649 Assessment of Foamed - Cement Slurries Using Conventional Cement Evaluation Logs and Improved Interpretation Methods. *SPE Rocky Mountain Regional Meeting*.

Kim, S. and Karrila, S. J. (2005). *Microhydrodynamics: Principles and Selected Applications*. Dover Publications, Inc., Mineola, NY, 2nd editio edition.

Kutchko, B., Crandall, D., Gill, M., McIntyre, D., Spaulding, R., Strazisar, B., Rosenbaum, E., Haljasmaa, I., Benge, G., Cunningham, E., DeBruijn, G., and Gardner, C. (2013). Computed Tomography and Statistical Analysis of Bubble Size Distributions in Atmospheric-Generated Foamed Cement. Technical Report August.

Kutchko, B., Crandall, D., Moore, J., Gill, M., McIntyre, D., Rosenbaum, E., Haljasmaa, I., Strazisar, B., Spaulding, R., Harbert, W., Benge, G., Cunningham, E., Lawrence, D. W., DeBruijn, G., and Gardner, C. (2015). Field-Generated Foamed Cement : Initial Collection , Computed Tomography , and Analysis. Technical Report July, U.S. Department of Energy, National Energy Technology Laboratory.

Lees, A. and Edwards, S. (1972). The computer study of transport processes under extreme conditions. *Journal of Physics C: Solid State Physics*, 5(15):1921.

Mathis, B. (2016). Foam Cement Bubble Characterization. Technical Report August, National Energy Technology Laboratory.

Nelson, E. B. (1990). *Well cementing*, volume 28. Newnes.

Ollion, J., Cochennec, J., Loll, F., Escudé, C., and Boudier, T. (2013). Tango: a generic tool for high-throughput 3d image analysis for studying nuclear organization. *Bioinformatics*, 29(14):1840–1841.

O'Rourke, T. J. N. S. C. and Crombie, D. N. S. C. (1999). A Unique Solution to Zonal Isolation Utilizing Foam-Cement and Coiled-Tubing Technologies. *Society of Petroleum Engineers*, (SPE 54473).

Phansalkar, N., More, S., Sabale, A., and Joshi, M. (2011). Adaptive local thresholding for detection of nuclei in diversity stained cytology images. In *2011 International Conference on Communications and Signal Processing*, pages 218–220. IEEE.

Rognon, P. G., Einav, I., and Gay, C. (2010). Internal relaxation time in immersed particulate materials. *Physical Review E - Statistical, Nonlinear, and Soft Matter Physics*, 81(6):1–9.

Rognon, P. G., Einav, I., and Gay, C. (2011). Flowing resistance and dilatancy of dense suspensions: lubrication and repulsion. *Journal of Fluid Mechanics*, 689:75–96.

Rognon, P. G. and Gay, C. (2008). Soft Dynamics simulation. 1. Normal approach of two deformable particles in a viscous fluid and optimal-approach strategy. *European Physical Journal E*, 27:253–260.

Rognon, P. G. and Gay, C. (2009). Soft dynamics simulation. 2. Elastic spheres undergoing a T 1 process in a viscous fluid. *European Physical Journal E*, 30:291–301.

Rosenbaum, E., Massoudi, M., and Dayal, K. (2019). Effects of polydispersity on structuring and rheology in flowing suspensions. *Journal of Applied Mechanics*.

Schindelin, J., Arganda-Carreras, I., Frise, E., Kaynig, V., Longair, M., Pietzsch, T., Preibisch, S., Rueden, C., Saalfeld, S., Schmid, B., et al. (2012). Fiji: an open-source platform for biological-image analysis. *Nature methods*, 9(7):676.

Tabakova, S. S. and Danov, K. D. (2009). Effect of disjoining pressure on the drainage and relaxation dynamics of liquid films with mobile interfaces. *Journal of Colloid and Interface Science*, 336(1):273–284.

White, J., Moore, S., Miller, M., Faul, R., and Services, H. E. (2000). IADC / SPE 59136 Foaming Cement as a Deterrent to Compaction Damage in Deepwater Production. *2000 IADC/SPE Drilling Conference*.

Chapter 5

Summary and Discussion[1]

The goal of this work was to determine the conditions that could lead to bubble clustering or structuring in a foamed cement slurry, which could lead to connected bubbles once the foamed cement cures, or which could result in crack formation along a line of bubbles. Either condition would affect the cement's ability to properly isolate the well. In the previous chapters, the development of a bubble interaction was shown in progression. In Chapter 2, simulations of hard spheres with no slip on the particle surface were shown. In Chapter 2, the pair interactions to simulate hard spheres was corrected and used for simulations of monodiperse and polydisperse hard spheres. The polydisperse pair interaction for hard spheres, in particular, required derivation of the linear resistance terms. Particles that are all the same sizes, (i.e. monodisperse particles), were compared to particles with different sizes, (i.e. polydisperse particles). In Chapter 3, the bubble interaction was developed and the results were shown for monodisperse bubbles compared to monodisperse hard spheres. The bubble interaction included: (1.) the slip on the bubble surface, (2.) the local deflection of the surface in the pair interaction region, (3.) a repulsive and attractive force that represents surfactant properties. However, in Chapter 3 the interaction was developed to simulate monodisperse bubbles. In Chapter 4 the interaction was developed for polydisperse bubbles. Also

[1]Invited Paper: Special issue "Recent Advances in Mechanics of Non-Newtonian Fluids", to be published.

in Chapter 4 simulation results are shown for a bubble size distribution that is lognormal and the mean and standard deviation were determined from a foamed cement sample produced in a field yard test.

5.1 Summary Analysis of Particles and Bubbles

The large number of bubbles required in the simulations can make it difficult to qualitatively identify bubble clusters or structures that would lead to loss of well isolation. An analysis of the neighbors of each particle/bubble was used to quantitatively identify clusters of particles/bubbles. The neighbor analysis was done for all volume fractions and can be a way to identify volume fractions or size distributions where clustering or structuring could occur.

The neighbor analysis was used to show regions of localized particle or bubble clustering or where any structuring has occurred due to shearing. The neighbor analysis considers each particle/bubble individually and uses a sphere around each particle/bubble and considers all other particles/bubbles within this sphere as a neighbor (Figure 4.7). The radius of the sphere, d, is the distance from the surface of the particle/bubble to the outside limit of the region considered for counting nearby particles/bubbles. The value of d is 1.5 for the analysis shown. A smaller radius did not identify the regions where structuring occurred in the simulated results (e.g. Figures 5.1 and 5.2, 50% by volume of bubbles). The neighbor analysis considers the periodic boundaries of the simulation box and particles/bubbles across the boundaries that are within the range of d are also counted as neighbors. This eliminates errors at the simulation box boundaries. The particles/bubbles are counted if $d_{i,j} < d$. The value of $d_{i,j}$ for the center particle/bubble i is calculated as follows:

$$d_{i,j} = \sqrt{(x_j - x_i)^2 + (y_j - y_i)^2 + (z_j - z_i)^2} - radius_j - radius_i \tag{5.1.0.1}$$

As the volume of particles or bubble increases, the number of neighbors of individual particles/bub-

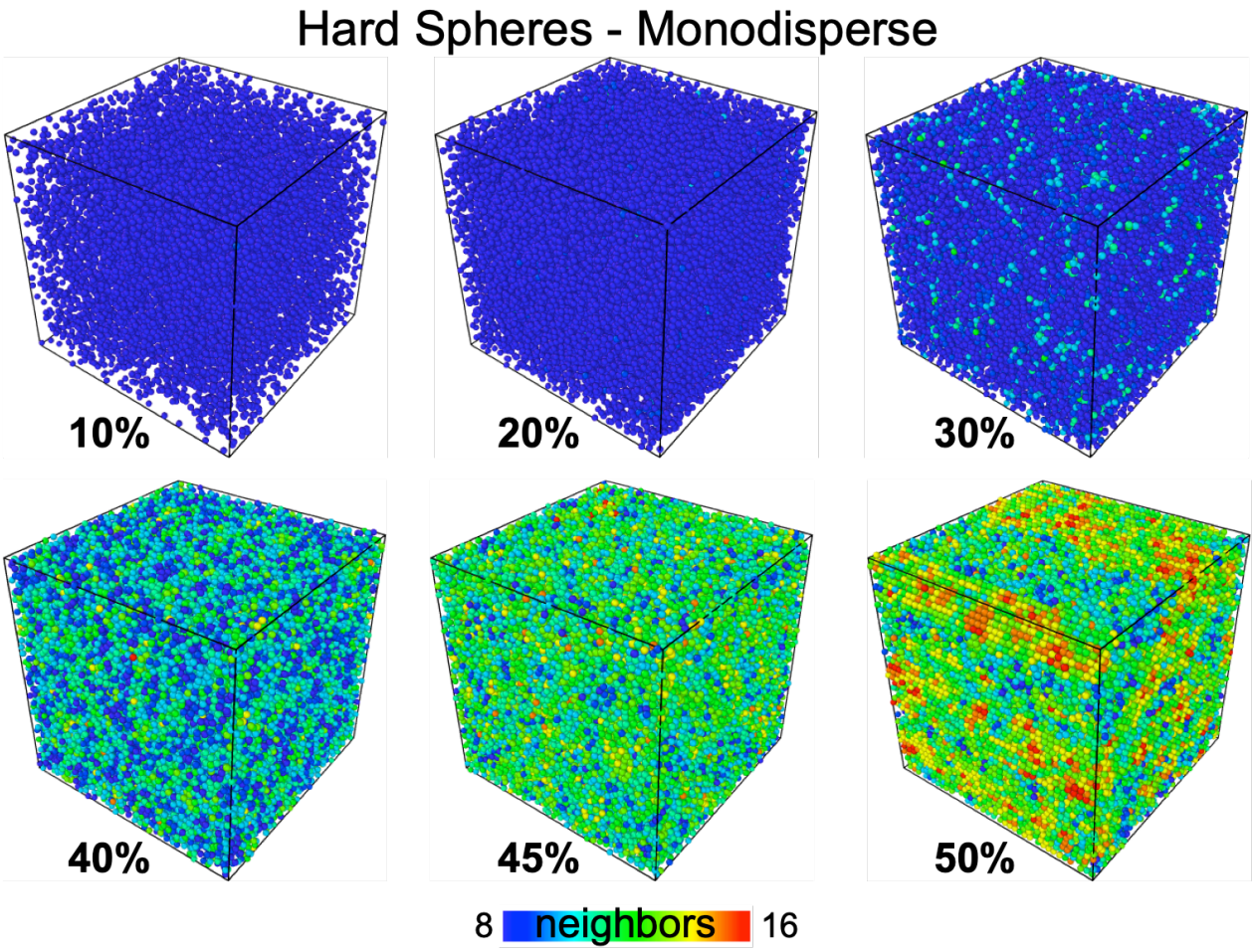

Figure 5.1: Simulation results of monodisperse hard spheres with no slip boundaries simulations at 10%, 20%, 30%, 40%, 45%, and 50% by volume of particles. The particles are shown at the final configuration after the box was strained to a value of 200.

bles also increases. The color key range, of 8 to 16 neighbors is the same for all the results shown so that the volume fractions can be compared. The volume fraction of particles/bubbles are shown at the final simulation configuration where the simulation box has been strained to a value of 200 for a true comparison between the monodisperse and polydisperse particles/bubbles and between the hard sphere particle interaction and the bubble interaction. Hard sphere particle results are show in Figures 5.1 through 5.4. For bubbles, the neighbor analysis results are shown in Figures 5.5 through 5.8. And finally, the neighbor analysis results are shown for the lognormal bubble size distribution taken from a real foamed cement is shown in Figures 5.9 and 5.10.

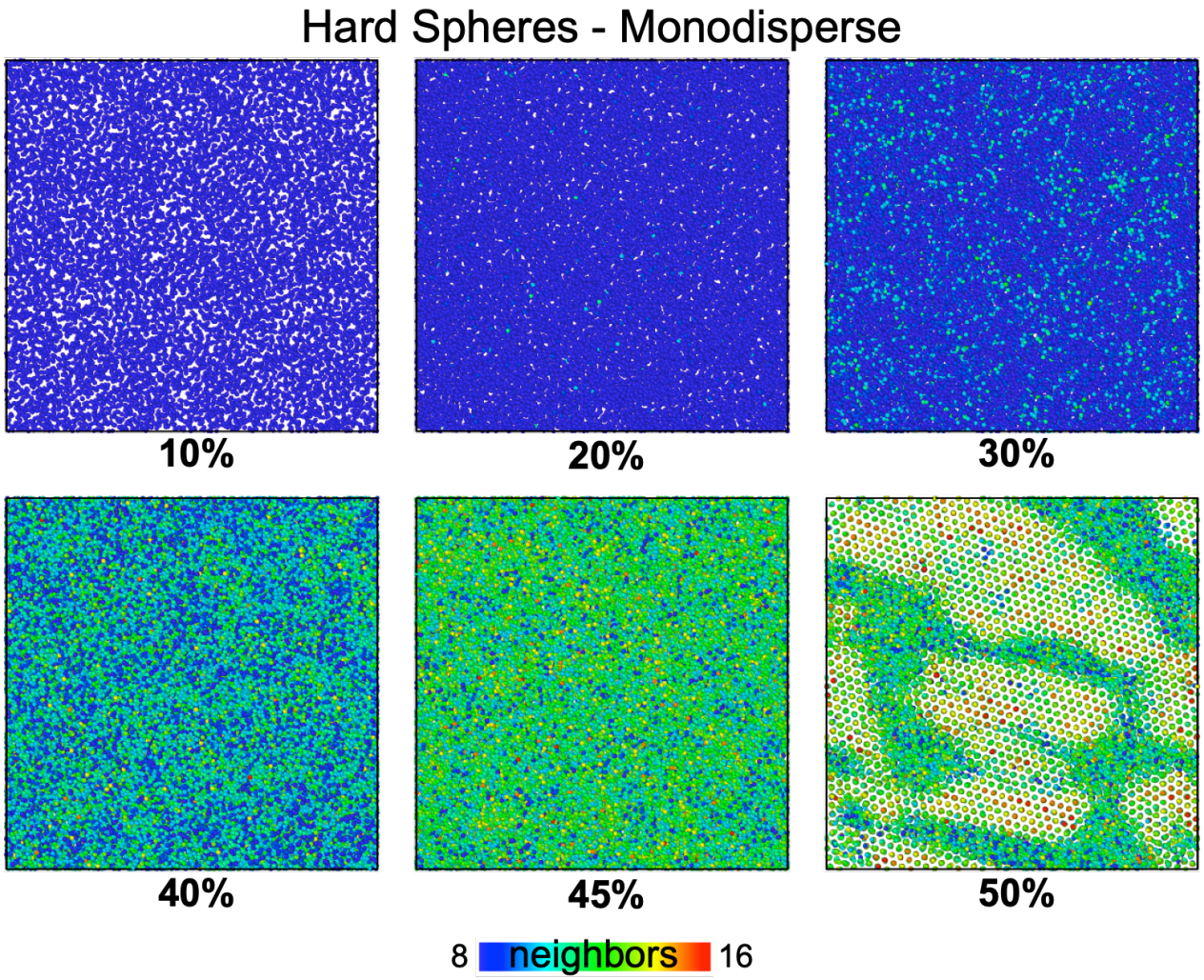

Figure 5.2: Simulation results of monodisperse hard spheres with no slip boundaries simulations at 10%, 20%, 30%, 40%, 45%, and 50% by volume of particles. The particles are shown at the final configuration after the box was strained to a value of 200. The particles are shown at half their size from the side view, looking through the whole sample.

The results of monodisperse hard spheres are shown in Figure 5.1 and Figure 5.2 and is the final configurations of the particles. For the monodisperse hard spheres, the 50% volume of hard sphere particles shows a lot of structuring of the particles. The regions of the most structuring also correspond to the higher number of neighbors of the individual particles. In Figure 5.2, the structuring at 50% of particles is more evident when the particles are viewed at half size. The image is shown from the side and looks through the whole simulation box. In Figure 5.1, the particles have structured into lines and are visible in the figure.

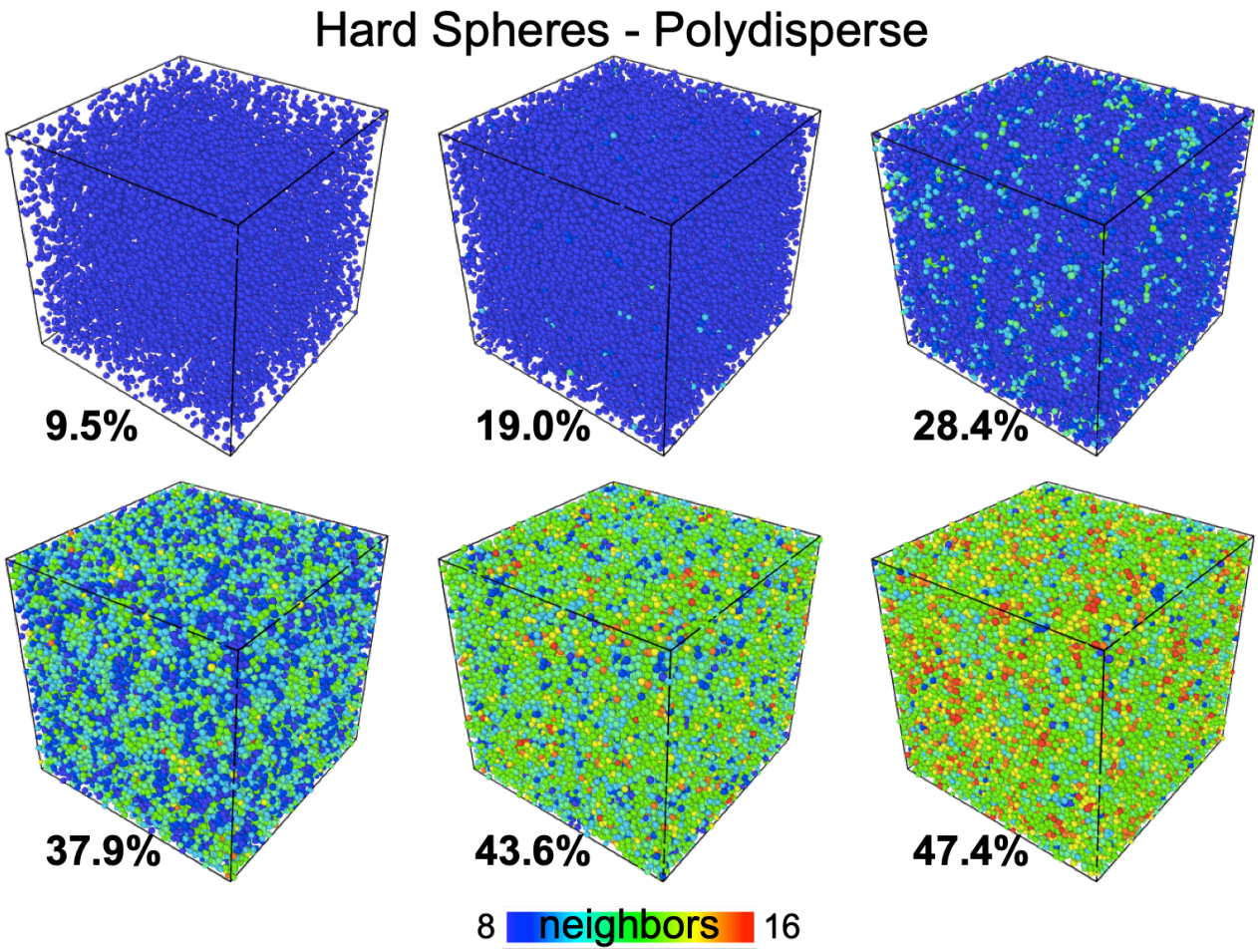

Figure 5.3: Simulation results of slightly polydisperse hard spheres with no slip boundaries simulations at 9.5%, 19.0%, 28.4%, 37.9%, 43.6%, and 47.4% by volume of particles. The size distribution is shown in Figure 2.3. The particles are shown at the final configuration after the box was strained to a value of 200.

The results of the neighbor analysis of polydisperse hard spheres is shown in Figure 5.3 and in Figure 5.4. The volume of particles in each of the simulations of the polydisperse hard spheres is a little below the comparable monodisperse hard spheres because the monodisperse particle systems were used to create the polydisperse inputs by increasing and decreasing the particle sizes. When a small amount of polydispersity is added to the particle sizes, it helps to reduce the structuring and aligning of the particles. The neighbor analysis of the polydisperse particles indicates that some clustering of the particles is occurring but they are only localized clusters.

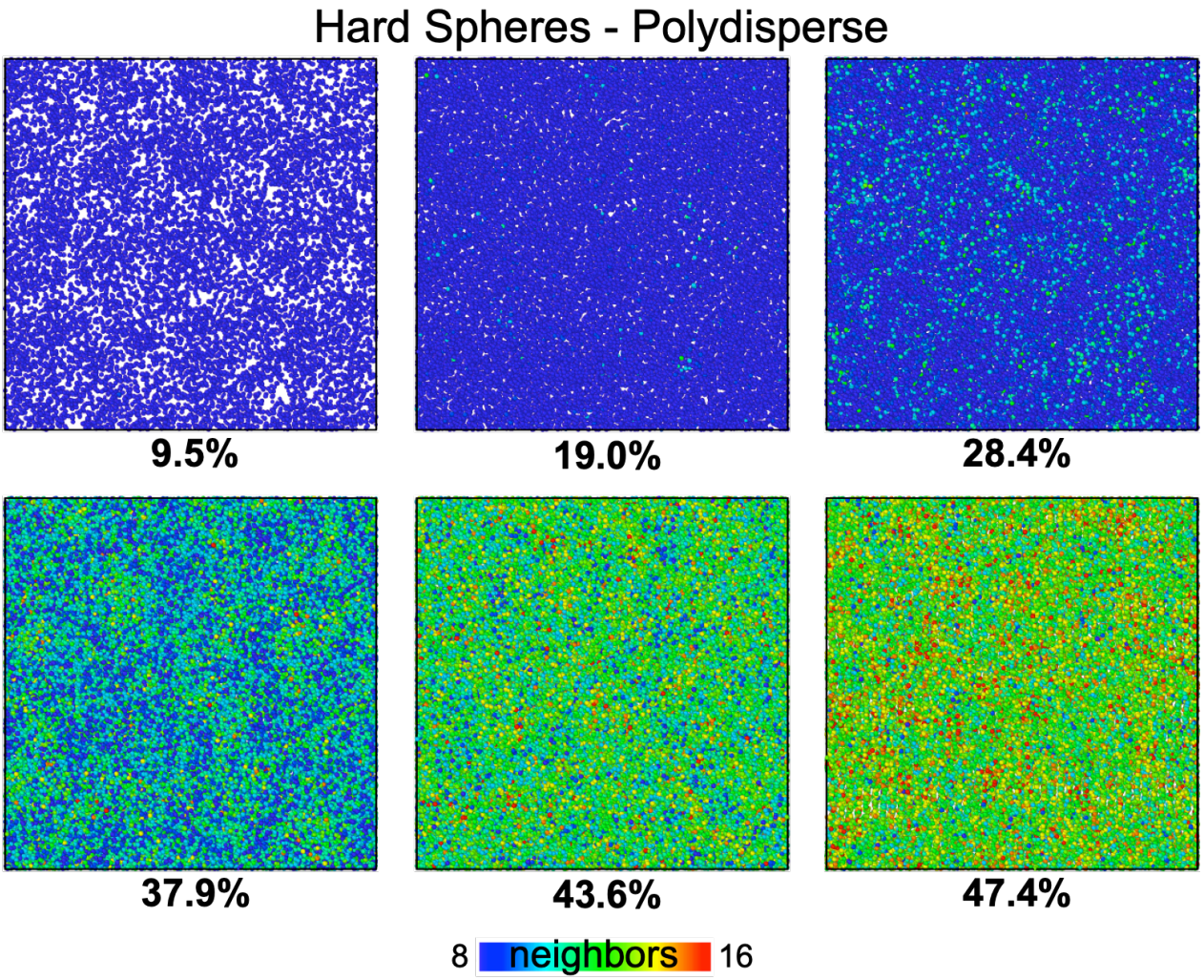

Figure 5.4: Simulation results of slightly polydisperse hard spheres with no slip boundaries simulations at 9.5%, 19.0%, 28.4%, 37.9%, 43.6%, and 47.4% by volume of particles. The size distribution is shown in Figure 2.3. The particles are shown at the final configuration after the box was strained to a value of 200. The particles are shown at half their size from the side view, looking through the whole sample.

The neighbor analysis results of the final configuration of the monodisperse bubbles are shown in Figure 5.5 and in Figure 5.6. The volume fraction of bubbles are directly comparable to the particle volume fractions as the same inputs of sizes and initial configurations were used. The properties of the bubble surface reduces the resistance in the pair interactions and the bubbles are not as subject to jamming. Subsequently, the number of neighbors of each of the bubble systems are slightly lower when compared to the monodisperse hard spheres.

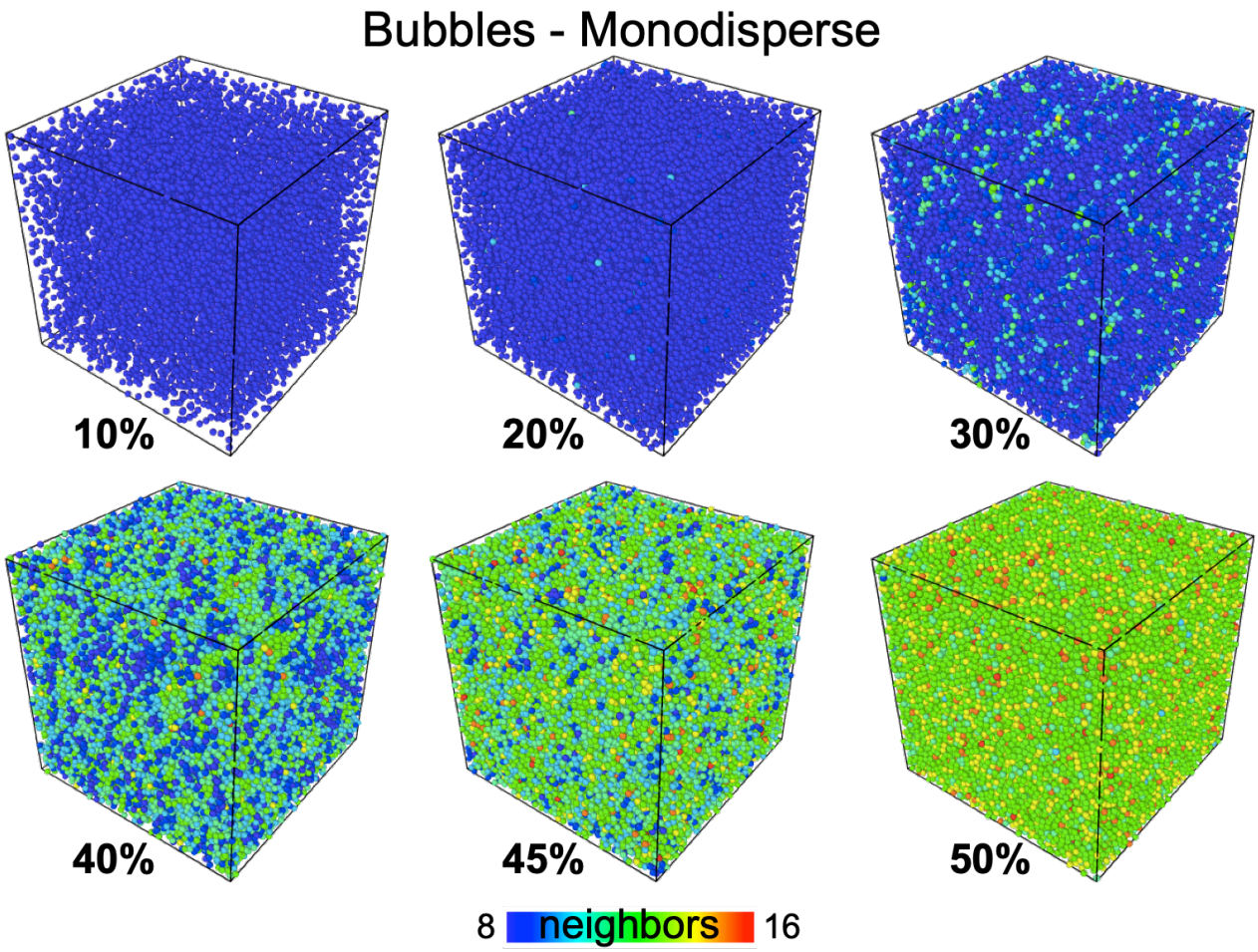

Figure 5.5: Simulation results of monodisperse bubbles with slip surface boundaries are shown for simulations at 10%, 20%, 30%, 40%, 45%, and 50% by volume of bubbles. The bubbles are shown at the final configuration after the box was strained to a value of 200.

The neighbor analysis of the slightly polydisperse bubbles is shown in Figures 5.7 and 5.8. The results are directly comparable to the slightly polydisperse hard spheres. Because of the slip on the bubble surface and the ability of the bubbles to slide by each other by allowing a surface deflection, there is no shearing resistance to the bubble surface. The result is that the bubbles are less subjective to jamming and there are fewer bubbles with close neighbors compared to the slightly polydisperse hard spheres. It is barely discernible but the polydisperse hard sphere particles have a small amount of structuring at a volume fraction of 47.4%.

The simulations that match the bubble size distribution taken from a real foamed cement sample

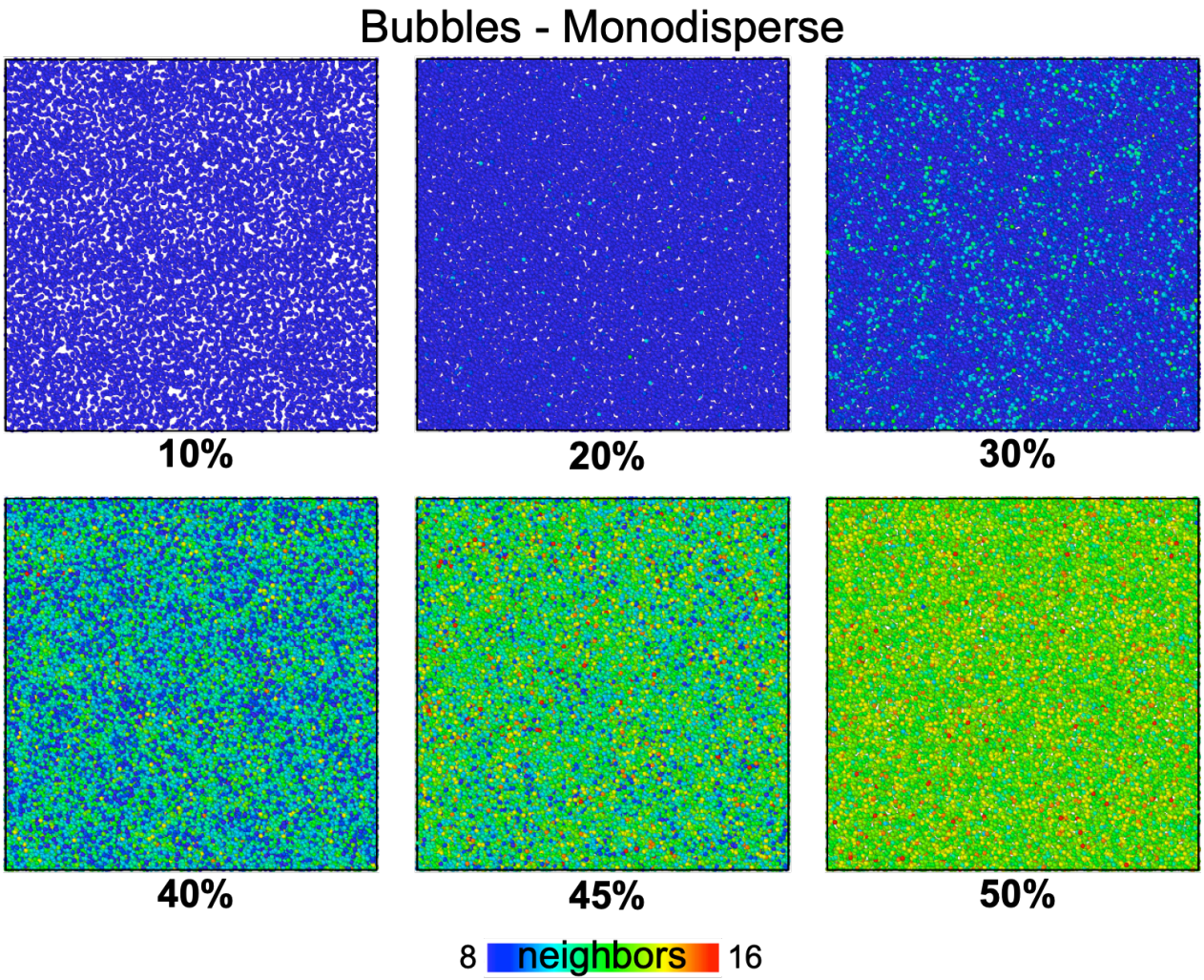

Figure 5.6: Simulation results of monodisperse bubbles with slip surface boundaries are shown for simulations at 10%, 20%, 30%, 40%, 45%, and 50% by volume of bubbles. The bubbles are shown at the final configuration after the box was strained to a value of 200. The bubbles are shown at half their size from the side view, looking through the whole sample.

are shown in Figures 5.9 and 5.10. The results between the lognormal polydispere bubbles and the slightly polydisperse bubbles is not discernible.

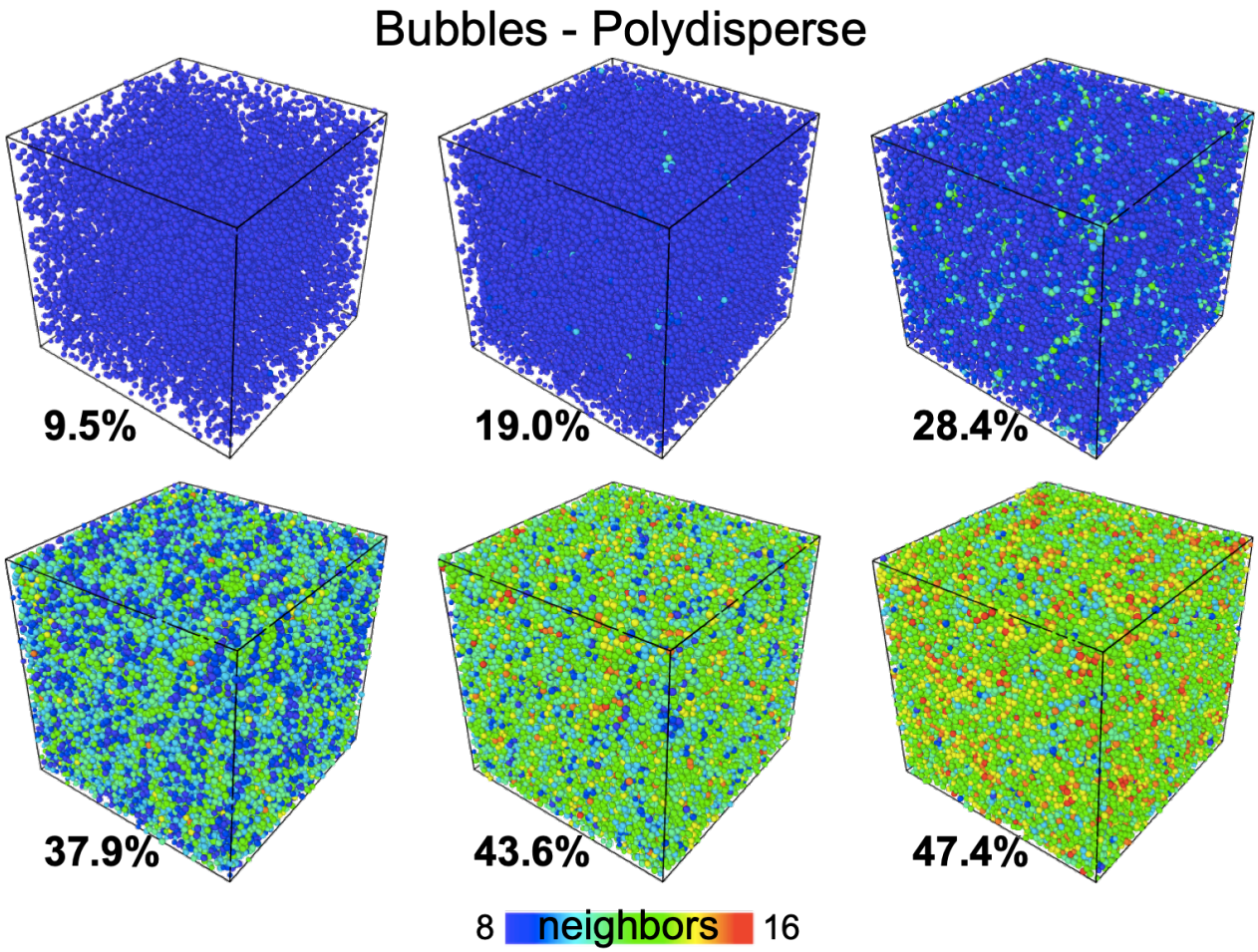

Figure 5.7: Simulation results of slightly polydisperse bubbles with slip surface boundaries simulations at 9.5%, 19.0%, 28.4%, 37.9%, 43.6%, and 47.4% by volume of particles. The size distribution is shown in Figure 2.3. The particles are shown at the final configuration after the box was strained to a value of 200.

5.2 Relative Viscosity/Viscosity Ratio

The relationship between the volume fraction (ϕ) of particles in a Newtonian fluid and the corresponding change in viscosity can be described by several equations with varying levels of complexity. The effects of particle concentration on the suspension viscosity is summarized in Massoudi (Massoudi and Wang, 2013). Einstein's classical equation accounts for the increase in viscosity due to the particle volume fraction and is linear in form.

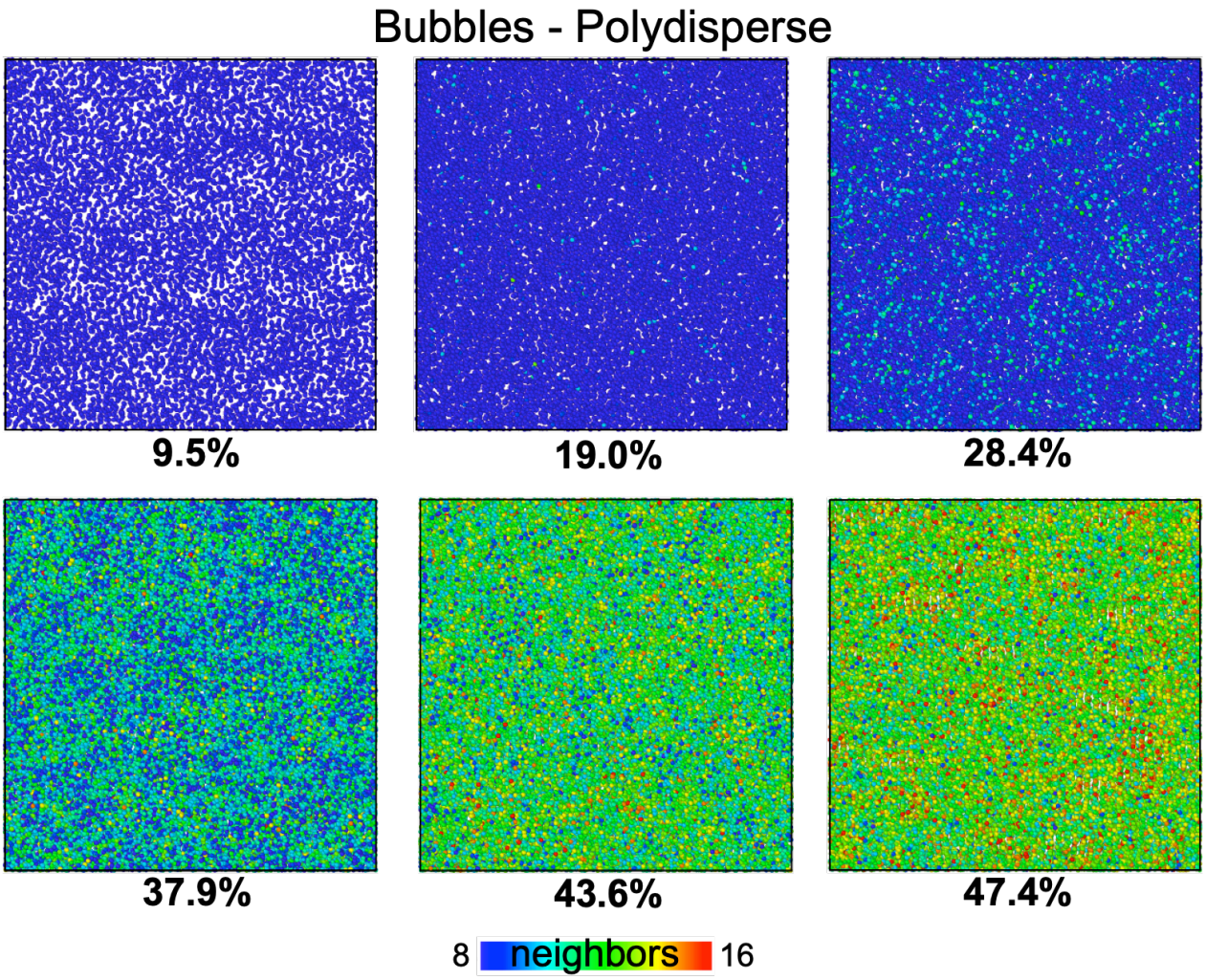

Figure 5.8: Simulation results of slightly polydisperse bubbles with slip boundaries simulations at 9.5%, 19.0%, 28.4%, 37.9%, 43.6%, and 47.4% by volume of particles. The size distribution is shown in Figure 2.3. The particles are shown at the final configuration after the box was strained to a value of 200. The particles are shown at half their size from the side view, looking through the whole sample.

Form of Einstein Equation (Einstein, 1956):

$$\mu = \mu_f(k + l\phi) \tag{5.2.0.1}$$

Krieger and Dougherty account for the limits of amount of particles that can be in the suspension due to the maximum packing fraction (ϕ_{max}).

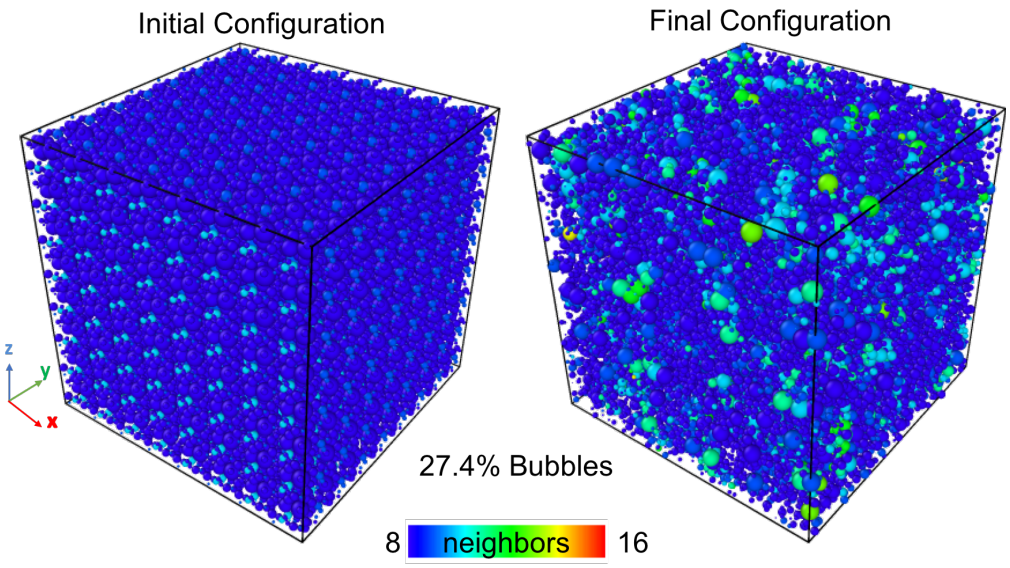

Figure 5.9: Simulation results of slightly polydisperse bubbles with slip surface boundaries simulations at 27.4% by volume of particles. The size distribution is shown in Figure 2.3. The particles are shown at the final configuration after the box was strained to a value of 200.

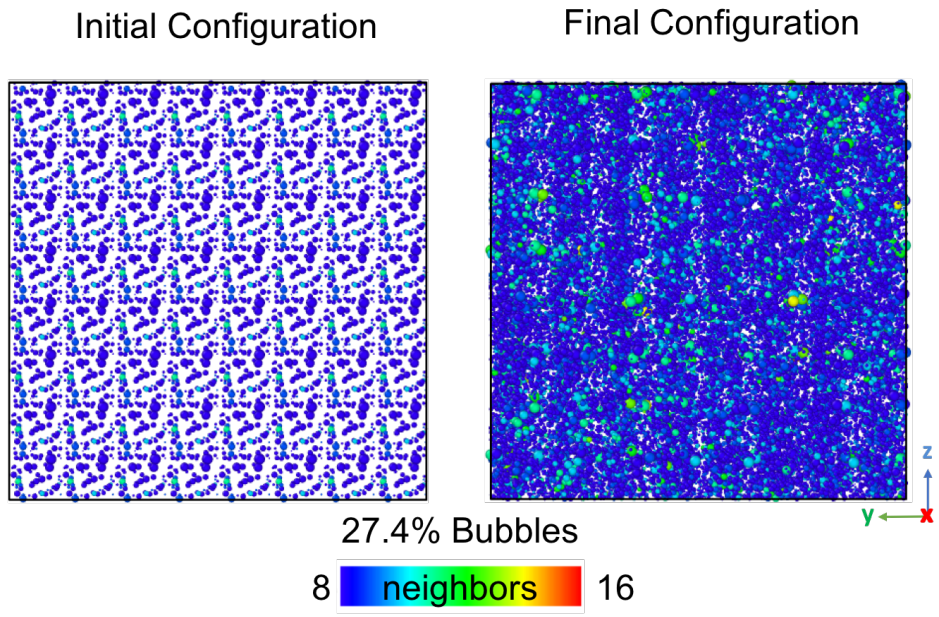

Figure 5.10: Simulation results of slightly polydisperse bubbles with slip boundaries simulations at 27.4% by volume of particles. The size distribution is shown in Figure 2.3. The particles are shown at the final configuration after the box was strained to a value of 200. The particles are shown at half their size from the side view, looking through the whole sample.

Form of Krieger and Dougherty Equation (Krieger and Dougherty, 1959):

$$\mu = \mu_f \left(m - \frac{\phi}{\phi_{max}} \right)^{-n\phi_{max}} \tag{5.2.0.2}$$

Batchelor and Green's equation is a second order polynomial and fits the simulation and experimental data the best of all the model equations.

Form of Batchelor and Green Equation (Batchelor and Green, 1972):

$$\mu = \mu_f(o + p\phi + q\phi^2) \tag{5.2.0.3}$$

Taylor's equation allows for fluid spheres of a different fluid from the base suspending fluid. Here, for bubbles, the fluid is air and is much lower than the suspending fluid.

Form of Taylor Equation (Taylor, 1932):

$$\mu = \mu_f \left[kk + ll\phi \left(\frac{\mu_{bubble} + mm\mu_f}{\mu_{bubble} + \mu_f} \right) \right] \tag{5.2.0.4}$$

The coefficients for the above equations for both particles and bubbles are summarized in Table 5.1.

The fit of Equations 5.2.0.1, 5.2.0.2, and 5.2.0.3 are shown in Figures 5.11 and 5.12. It is obvious that the second order polynomials, including the Batchelor form of the viscosity equation, fit the data the best.

The simulated relative viscosity data can be compared with some of the known experimental data (Figure 5.13). The most comprehensive collection of the viscosity of foamed cement is contained in Al-Mashat's thesis (Al-Mashat, 1977). However, Al-Mashat's method for measuring the viscosity is dependent on the size of the pipe used in the setup. The viscosity measurement should not

Coefficient	Monodisperse Particle	Polydisperse Particle	Monodisperse Bubble	Polydisperse Bubble
k	7.463e-07	3.578e-06	2.479e-08	0.4661
l	0.1605	0.1609	0.1665	0.09995
m	1.057	1.014	1.048	0.9535
n	0.02799	0.02725	0.0281	0.0198
o	0.9777	0.9	0.943	1.006
p	0.007433	1.777e-10	3.793e-14	0.01958
q	0.003042	0.003415	0.003393	0.001581

Table 5.1: Coefficients for fits of Equations (5.2.0.1), (5.2.0.3), (5.2.0.2), and (5.2.0.4) for the simulated results with a 95% confidence interval in the fit. The equation fit was determined with Matlab.

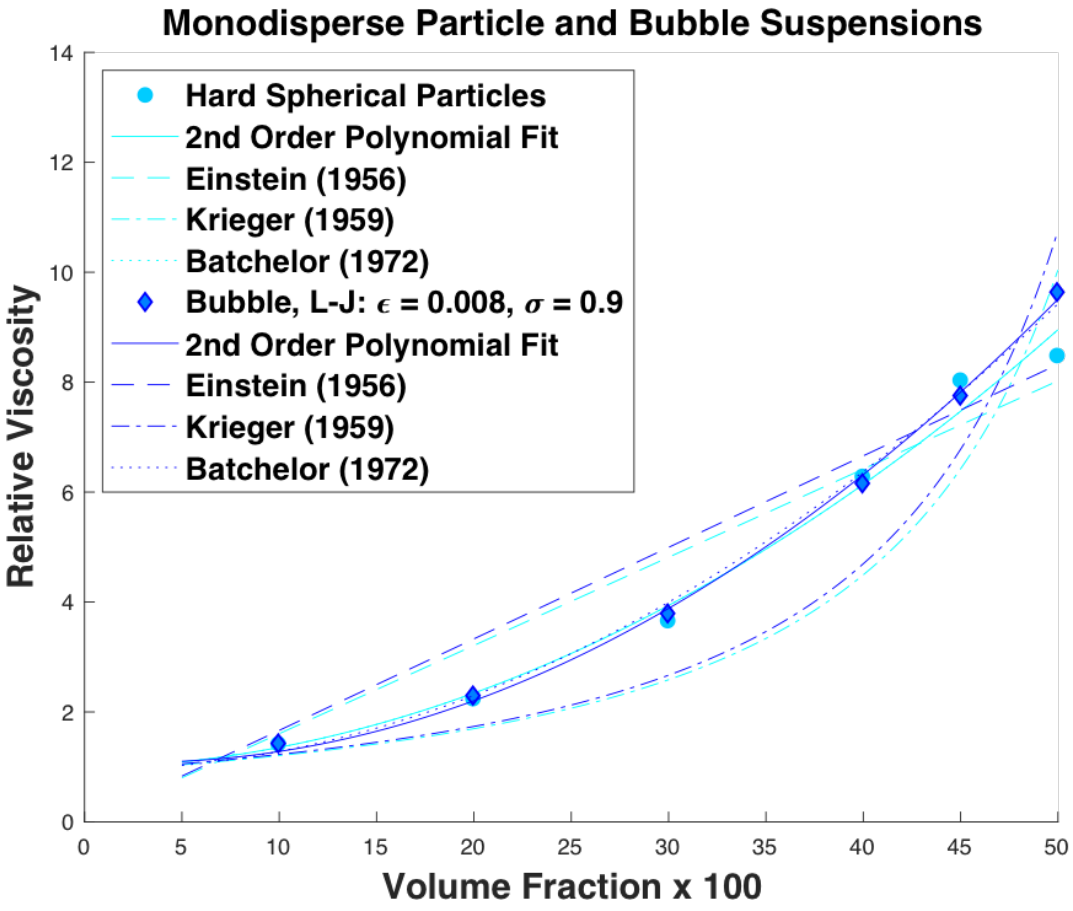

Figure 5.11: The relative viscosity determined from the simulated results is indicated by points and the lines are the equations fit to the data.

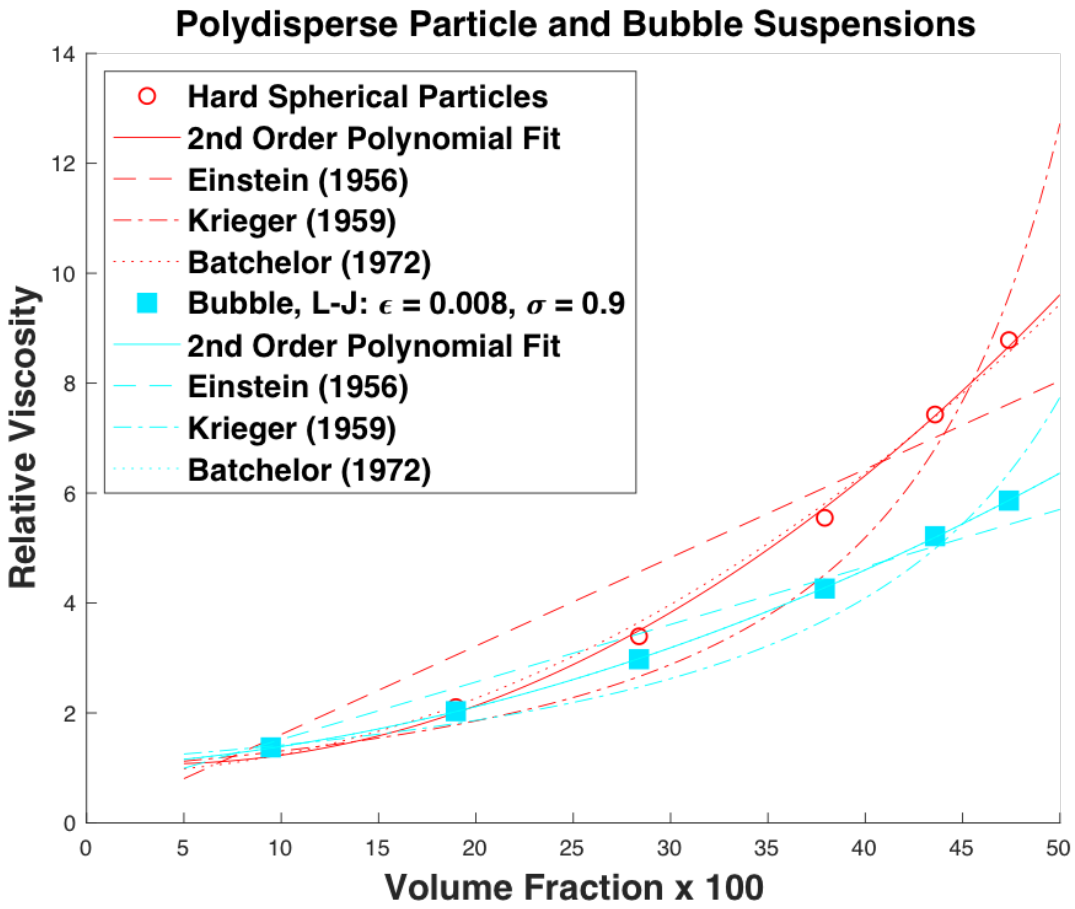

Figure 5.12: The relative viscosity determined from the simulated results is indicated by points and the lines are the equations fit to the data.

depend on the measuring device dimensions so it can be expected that the measurements reported may not be the most correct and would be different with another size of pipe. The data does show the increase in the viscosity due to the addition of bubbles. Olowolagba (Olowolagba et al., 2010) reports more accurate results. The simulated data matches well to the few accurate experimental results.

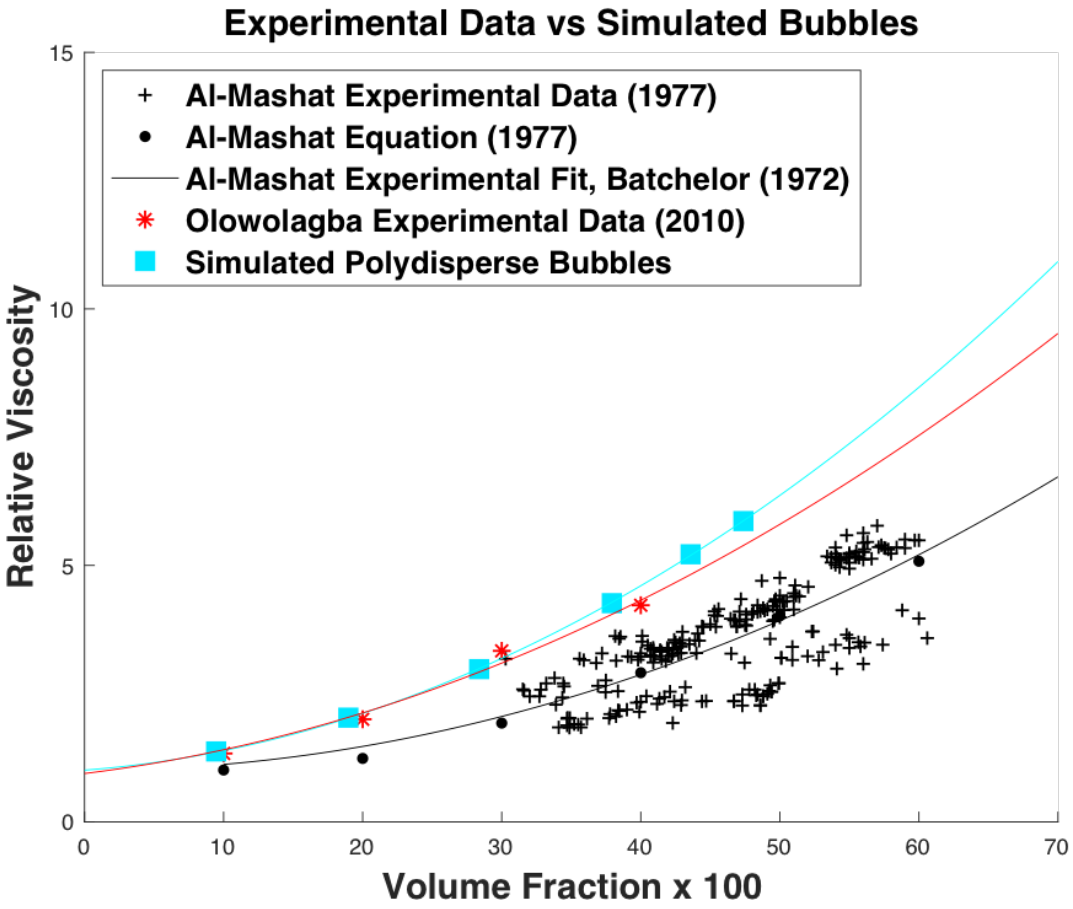

Figure 5.13: The relative viscosity determined from the simulated results is shown with the experimental data of Al-Mashat (Al-Mashat, 1977) and (Olowolagba et al., 2010).

5.3 Conclusions

This research has led to the developed a bubble interaction that can simulate bubbles suspended in a Newtonian fluid to study foamed cement. By including realistic properties to make the suspended particles more like real bubbles (i.e. polydispersity, slip on the surface, no shearing resistance, the ability of the surface to deform locally in the region of the pair interaction, and a force to represent the surfactant), simulations can be performed to study the re-arrangement of the bubbles due to shearing. This relates to flow in the well. During cement placement, the cement is continually flowing and it can be expected that the bubbles will re-arrange and structure due to flow under the right bubble size distribution and a high enough volume fraction of bubbles. The targeted volume fractions of bubbles in the cement ($< 35\%$) should not have any issues or lead to bubble structuring due to flow. However, as the pressure changes in the well, so does the volume fractions of the bubbles. For this reason, a range of volume fractions was studied.

Volume fractions of bubbles up to a value of 50% show that the bubbles are re-arranging due to imposed flow but the bubbles are not structuring or clustering in any significant way. If volume fractions above the maximum packing fraction were to occur, the bubbles would become distorted in shape and could not be considered spherical. If higher volume fractions approaching the maximum packing fraction are shown to cause clustering, a means of re-dispersing the bubbles before the final placement location would alleviate this issue.

The calculations here assume Newtonian suspending fluids, which is a limitation of the overall Stokesian Dynamics framework. It would be expected that these results of bubbles in a Newtonian fluid would vary from experiments of real bubbles in a non-Newtonian fluid. However, there is currently no practical way to keep track of all bubbles without assuming that the suspending fluid is Newtonian. The few experimental measurements of foamed cement are shown to match the simulated results well, despite the assumption that the suspending fluid is Newtonian. The dominant forces are the lubrication forces and at the scales relevant to calculate the lubrication forces, the

fluid between the bubbles would be mostly water, a Newtonian fluid. It is still possible to learn from these simulations and identify possible conditions that could lead to bubbles structuring into strings of bubbles or clustering that could increase permeability beyond acceptable levels. Homogenization or mixture-theory based approaches, e.g. based on (Avazmohammadi and Castañeda, 2016; Christoffersen et al., 1981; Gao et al., 2011, 2012; Lipton and Avellaneda, 1990; Lipton and Vernescu, 1994; Massoudi, 2002, 2003, 2008, 2010), may enable the formulation of continuum models that can provide insight into particle structuring while also accounting for the complex rheology of cement paste.

5.4 Future Work

One of the largest challenges in this research proved to be in creating simulation inputs at high volume fractions of particles that would run without errors in the LAMMPS environment and with the pair interactions developed and used here. One reason is that the inputs are approaching the maximum packing fraction obtainable without having overlapping particles. LAMMPS will not accept particle configurations with overlapping particles and this is not physically relevant to the problem and for studying real systems. This technique is limited in the volume fractions that can be studied because these bubbles are assumed to be spherical and will therefore have a maximum packing fraction. It is difficult to create initial conditions of particle and bubble systems of randomly placed particle inputs above 50% particles by volume. The maximum packing fraction of ordered spheres is roughly $\sim 34\%$ to $\sim 74\%$ – depending on sphere packing pattern (Gauss, 1876) – and these packings are uniform. A random arrangement of sphere packing when compressed has a maximum packing fraction of $\sim 64\%$ (Song et al., 2008). Therefore, an initial condition with not too much polydispersity that approaches these volume fractions would have to be more ordered initially. So the challenge is now in creating the simulation inputs that better represent real foams. To obtain higher volume fractions of polydisperse bubbles some new techniques must be developed.

5.4.1 Simulation Inputs with Many Bubbles' Sizes

It is possible to create higher volume fractions of bubbles and with more variety of the bubbles. To produce a 30% volume fraction of bubbles as an input, the distribution of the sizes was determined first and assuming a simulation box size of $10 \times 10 \times 10$. The lognormal distribution of sizes is done by randomly identifying a bubble size with a mean and standard distribution that matches a real foamed cement sample and creating bubbles until the volume fraction is reached. Then to place the bubbles, a Monte Carlo method was used to randomly place them in the box. To make the process faster and to make sure that all bubbles could be placed, the simulation box where the particles are placed is made much larger. In this case, each side was set to 30 to make a $30 \times 30 \times 30$ box. A Monte Carlo method is good for placing particles in random arrangements and the majority of the particles can be placed quickly and easily. As the space is used up by the bubbles, it becomes more and more difficult to place the bubbles in the box but with the box being three times larger than it needs to be during the placement process, the bubbles can all be placed.

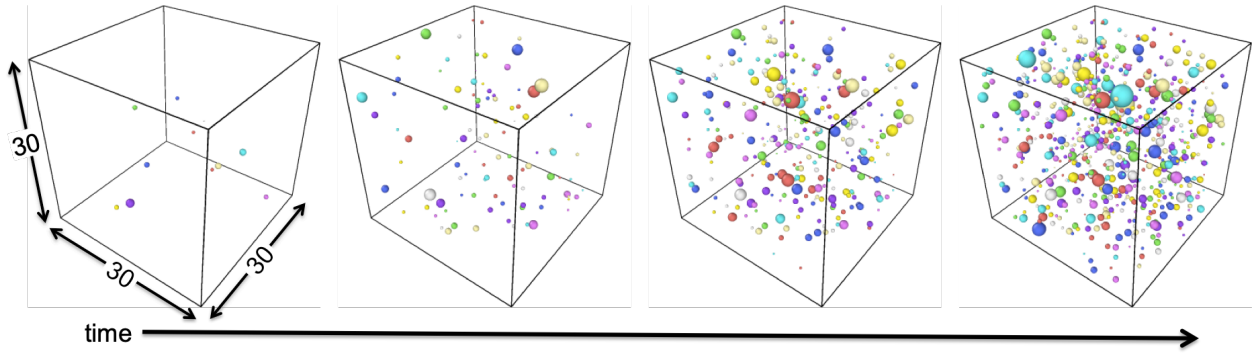

Figure 5.14: A monte carlo method was used to add bubbles with a lognormal size distribution randomly to the box. The mean and standard deviation of the lognormal bubble size distribution are from a real foamed cement sample.

Figure 5.14 shows the placement of a 30% by volume fraction of bubbles with a lognormal size distribution and over time, the placement of the bubbles in a $30 \times 30 \times 30$ simulation box (Figure 5.15). The size distribution has a volume fraction of 30% in a $10 \times 10 \times 10$ box so the bubble configuration will need to be compressed to obtain the volume fraction of 30%. It was determined

and described previously (Rosenbaum et al., 2019) that by replicating a simulation box of size $10 \times 10 \times 10$ four times in each direction, that the system size will not affect the results. So the next step is to **replicate** the $30 \times 30 \times 30$ box. After replicating the $30 \times 30 \times 30$ box, the next step is to **shrink** the simulation box and compress the bubbles to have a volume of 30% and a size of $40 \times 40 \times 40$ to match the predetermined simulation box size required and used in previous work.

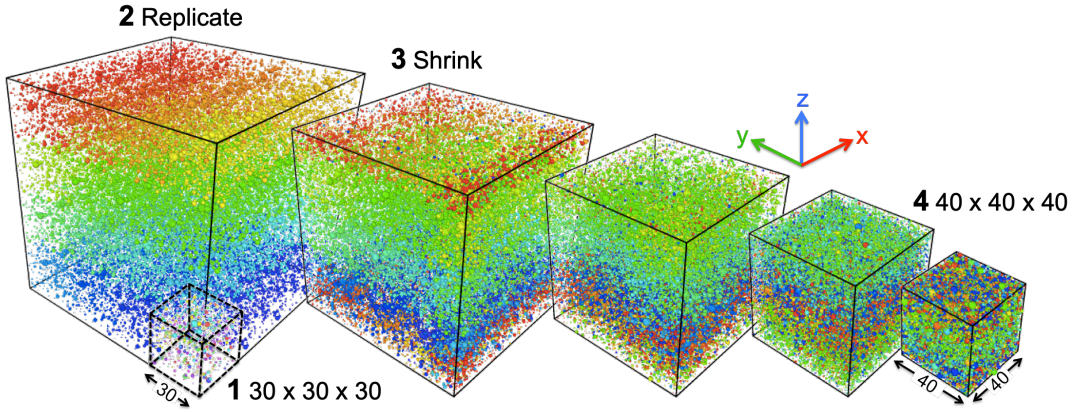

Figure 5.15: The (1) initial $30 \times 30 \times 30$ simulation box is (2) replicated in all directions and then the simlation box is (3) shrunk down in all directions to obtain the minimum system size needed of (4) $40 \times 40 \times 40$.

This process solves several issues with previous methods of producing simulation inputs but still has some issues. First, it makes it possible to place all of the bubbles and to make simulation inputs with a lognormal size distribution to match any real suspension of bubbles and at any volume fraction. The bubbles also start out in random placement because the replicating is done before the shrinking step that serves to mix up the bubbles. An issue that has not been resolved with this process is that a lot of bubbles overlap. If the bubbles in the simulation input overlap at the start of the simulation, errors will be produced and the simulation cannot be run. It is also not physically comparable to the real sample to have overlapping bubbles (they should only be allowed to have a surface that deflects locally in the region of interaction).

5.4.2 Simulations with Real Foamed Cement Bubble Inputs

Real foamed cement bubble sizes and positions can be determined for computer tomography scans of foamed cement samples. However, this produces a large number of bubbles, with a different size and bubble type for each bubble. The bubble simulation code will need additional development to run these more complicated simulation inputs. This is planned for future research.

5.5 Chapter 5 References

Bibliography

Al-Mashat, A. M. (1977). *Rheology of Foam Cement*. Doctor of philosophy, Colorado School of Mines.

Avazmohammadi, R. and Castañeda, P. P. (2016). Macroscopic rheological behavior of suspensions of soft solid particles in yield stress fluids. *Journal of Non-Newtonian Fluid Mechanics*, 234:139–161.

Batchelor, G. and Green, J. (1972). The determination of the bulk stress in a suspension of spherical particles to order c 2. *Journal of Fluid Mechanics*, 56(3):401–427.

Christoffersen, J., Mehrabadi, M., and Nemat-Nasser, S. (1981). A micromechanical description of granular material behavior. *Journal of applied mechanics*, 48(2):339–344.

Einstein, A. (1956). Investigations on the theory of the brownian movement: Doverpublications. com. *New York*, 58.

Gao, T., Hu, H. H., and Castañeda, P. P. (2011). Rheology of a suspension of elastic particles in a viscous shear flow. *Journal of Fluid Mechanics*, 687:209–237.

Gao, T., Hu, H. H., and Castañeda, P. P. (2012). Shape dynamics and rheology of soft elastic particles in a shear flow. *Physical review letters*, 108(5):058302.

Gauss, C. F. (1876). Besprechung des buchs von la seeber: Untersuchungen uber die eigenschaften der positiven ternaren quadratischen formen usw. *Gottingensche Gelehrte Anzeigen*, 2:188–196.

Krieger, I. M. and Dougherty, T. J. (1959). A mechanism for non-newtonian flow in suspensions of rigid spheres. *Transactions of the Society of Rheology*, 3(1):137–152.

Lipton, R. and Avellaneda, M. (1990). Darcy's law for slow viscous flow past a stationary array of bubbles. *Proceedings of the Royal Society of Edinburgh Section A: Mathematics*, 114(1-2):71–79.

Lipton, R. and Vernescu, B. (1994). Homogenisation of two-phase emulsions. *Proceedings of the Royal Society of Edinburgh Section A: Mathematics*, 124(6):1119–1134.

Massoudi, M. (2002). On the importance of material frame-indifference and lift forces in multiphase flows. *Chemical Engineering Science*, 57(17):3687–3701.

Massoudi, M. (2003). Constitutive relations for the interaction force in multicomponent particulate flows. *International Journal of Non-Linear Mechanics*, 38(3):313–336.

Massoudi, M. (2008). A note on the meaning of mixture viscosity using the classical continuum theories of mixtures. *International Journal of Engineering Science*, 46(7):677–689.

Massoudi, M. (2010). A mixture theory formulation for hydraulic or pneumatic transport of solid particles. *International Journal of Engineering Science*, 48(11):1440–1461.

Massoudi, M. and Wang, P. (2013). Slag behavior in gasifiers. part ii: constitutive modeling of slag. *Energies*, 6(2):807–838.

Olowolagba, K. O., Brenneis, C., et al. (2010). Techniques for the study of foamed cement rheology. In *SPE Production and Operations Conference and Exhibition*. Society of Petroleum Engineers.

Rosenbaum, E., Massoudi, M., and Dayal, K. (2019). Effects of polydispersity on structuring and rheology in flowing suspensions. *Journal of Applied Mechanics*.

Song, C., Wang, P., and Makse, H. A. (2008). A phase diagram for jammed matter. *Nature*, 453(7195):629.

Taylor, G. I. (1932). The viscosity of a fluid containing small drops of another fluid. *Proceedings of the Royal Society of London. Series A, Containing Papers of a Mathematical and Physical Character*, 138(834):41–48.

Thesis References

Bibliography

(2003). *LAMMPS Users Manual*. Sandia National Laboratories.

Ahmed, R. M., Takach, N. E., Khan, U. M., Taoutaou, S., James, S., Saasen, a., and Godø y, R. (2009). Rheology of foamed cement. *Cement and Concrete Research*, 39(4):353–361.

Al-Mashat, A. M. (1977). *Rheology of Foam Cement*. Doctor of philosophy, Colorado School of Mines.

American Petroleum Institute (2010). Isolating Potential Flow Zones During Well Construction - API Standard 65 Part 2.

API 10B-4 (2004). Recommended Practice on Preparation and Testing of Foamed Cement Slurries at Atmospheric Pressure ANSI / API Recommended Practice 10B-4. Technical Report July.

Atkin, R. and Craine, R. (1976). Continuum theories of mixtures: basic theory and historical development. *The Quarterly Journal of Mechanics and Applied Mathematics*, 29(2):209–244.

Avazmohammadi, R. and Castañeda, P. P. (2016). Macroscopic rheological behavior of suspensions of soft solid particles in yield stress fluids. *Journal of Non-Newtonian Fluid Mechanics*, 234:139–161.

Ball, R. C. and Melrose, J. R. (1997). A simulation technique for many spheres in quasi-static motion under frame-invariant pair drag and Brownian forces. *Physica A: Statistical Mechanics and its Applications*, 247(1-4):444–472.

Banfill, P. F. G. (2006). Rheology of Fresh Cement and Concrete. *Rheology Reviews 2006*, 2006:61–130.

Batchelor, G. and Green, J. (1972). The determination of the bulk stress in a suspension of spherical particles to order c 2. *Journal of Fluid Mechanics*, 56(3):401–427.

Bechinger, C., Sciortino, F., and Ziherl, P. (2013). *Physics of Complex Colloids*. IOS Press.

Beltempo, A., Zingales, M., Bursi, O. S., and Deseri, L. (2018). A fractional-order model for aging materials: An application to concrete. *International Journal of Solids and Structures*, 138:13–23.

Benge, O. G., McDermott, J. R., Langlinais, J. C., and Griffith, J. E. (1996). Foamed cement job successful in deep HTHP offshore well. *Oil and Gas Journal*, 94.

Bikerman, J. J. (1965). Foams and Emulsions. *Industrial & Engineering Chemistry . . .* , 57(1):56–62.

Bolte, S. and Cordelieres, F. (2006). A guided tour into subcellular colocalization analysis in light microscopy. *Journal of microscopy*, 224(3):213–232.

Bossis, G. and Brady, J. F. (1984). Dynamic simulations of sheared suspensions. {I.} General method. *J. Chem. Phys.*, 80(10):5141–5154.

Bour, D. and Rickard, B. (2000). Application of Foamed Cement on Hawaiian Geothermal Well. *Geothermal Resources Council Transactions*, 24.

Bowen, R. (1976). Theory of mixtures. In Eringen, A., editor, *Continuum physics (Vol. III)*, page 1. Waltham: Academic Press, New York.

Brady, J. (1988). Stokesian Dynamics. *Annual Review of Fluid Mechanics*, 20(1):111–157.

Burdylo, L. and Birch, G. (1990). Primary Cementing Techniques. In Nelson, E. B., editor, *Well Cementing*, chapter 12, pages 12–1–12–27.

Bybee, M. D. (2009). *HYDRODYNAMIC SIMULATIONS OF COLLOIDAL GELS: MICROSTRUCTURE, DYNAMICS, AND RHEOLOGY*. PhD thesis, University of Illinois at Urbana-Champaign.

Christoffersen, J., Mehrabadi, M., and Nemat-Nasser, S. (1981). A micromechanical description of granular material behavior. *Journal of applied mechanics*, 48(2):339–344.

Clift, R. (1978). Bubbles. *Drops and Particles*.

Crowe, C., Sommerfeld, M., Tsuji, Y., et al. (1998). Multiphase flows with.

Dalton, L. E., Brown, S., Moore, J., Crandall, D., and Gill, M. (2018). Evolution Using CT Scanning : Insights From Elevated-Pressure Generation. (January):1–11.

Davis, R. H., Schonberg, J. a., and Rallison, J. M. (1989). The lubrication force between two viscous drops. 77(1989).

Dayal, K. and James, R. D. (2010). Nonequilibrium molecular dynamics for bulk materials and nanostructures. *Journal of the Mechanics and Physics of Solids*, 58(2):145–163.

Dayal, K. and James, R. D. (2012). Design of viscometers corresponding to a universal molecular simulation method. *Journal of Fluid Mechanics*, 691:461–486.

de Rozières, J. and Ferrière, R. (1991). Foamed-Cement Characterization Under Downhole Conditions and Its Impact on Job Design. *SPE Production Engineering*, (August):297–304.

de Rozieres, J. and Griffin, T. J. (1990). Chapter 14 Foamed Cements. In Nelson, E. B., editor, *Well Cementing*, pages 14.1 – 14.19. Schlumberger Educational Services, 300 Schlumberger Drive, Sugar Land, Texas 77478.

Dusterhoft, D. M. (2003). Foamed & Lightweight Cements. pages 1–12.

Economides, M. J. (1990). 1. Implications of Cementing on Well Performance. In Nelson, E. B., editor, *Well Cementing*, chapter 1, pages 1.1 – 1.6. Schlumberger Educational Services, Sugar Land, Texas.

Einstein, A. (1956). Investigations on the theory of the brownian movement: Doverpublications. com. *New York*, 58.

Eringen, A. C. (2007). *Nonlocal Continuum Field Theories*. Springer Science & Business Media.

Frisch, G. J., Services, H. E., and Graham, W. L. (1999). SPE 55649 Assessment of Foamed - Cement Slurries Using Conventional Cement Evaluation Logs and Improved Interpretation Methods. *SPE Rocky Mountain Regional Meeting*.

Gao, T., Hu, H. H., and Castañeda, P. P. (2011). Rheology of a suspension of elastic particles in a viscous shear flow. *Journal of Fluid Mechanics*, 687:209–237.

Gao, T., Hu, H. H., and Castañeda, P. P. (2012). Shape dynamics and rheology of soft elastic particles in a shear flow. *Physical review letters*, 108(5):058302.

Gaudron, R., Warnez, M., and Johnsen, E. (2015). Bubble dynamics in a viscoelastic medium with nonlinear elasticity. *Journal of Fluid Mechanics*, 766:54–75.

Gauss, C. F. (1876). Besprechung des buchs von la seeber: Untersuchungen uber die eigenschaften der positiven ternaren quadratischen formen usw. *Gottingensche Gelehrte Anzeigen*, 2:188–196.

Goldhirsch, I. (2003). Rapid granular flows. *Annual review of fluid mechanics*, 35(1):267–293.

Griffith, J. E., Lende, G., Ravi, K., Saasen, A., Nø dland, N. E., and Jordal, O. H. (2004). Foam Cement Engineering and Implementation for Cement Sheath Integrity at High Temperature and High Pressure. *IADC/SPE Drilling Conference*, (SPE 87194).

Guillot, D. (1990). Rheology of Well Cement Slurries. *Developments in Petroleum Science*, 28(C):4–1–4–37.

Happel, J. and Brenner, H. (1973). Low reynolds number hydrodynamics, noordhoff int. *Publishing, Leyden, Netherland*, 235.

Herrmann, H. (1999). Statistical models for granular materials. *Physica A: Statistical Mechanics and its Applications*, 263(1-4):51–62.

Herrmann, H. and Luding, S. (1998). Modeling granular media on the computer. *Continuum Mechanics and Thermodynamics*, 10(4):189–231.

James, R. D. and Müller, S. (1994). Internal variables and fine-scale oscillations in micromagnetics. *Continuum Mechanics and Thermodynamics*, 6(4):291–336.

Jeffrey, D. J. and Onishi, Y. (1984). Calculation of the resistance and mobility functions for two unequal rigid spheres in low-Reynolds-number flow. *Journal of Fluid Mechanics*, 139(-1):261.

Kim, S. and Karrila, S. J. (2005). *Microhydrodynamics: Principles and Selected Applications*. Dover Publications, Inc., Mineola, NY, 2nd editio edition.

Krieger, I. M. and Dougherty, T. J. (1959). A mechanism for non-newtonian flow in suspensions of rigid spheres. *Transactions of the Society of Rheology*, 3(1):137–152.

Kumar, A. (2010). *Microscale Dynamics in Suspensions of Non-Spherical Particles*. Doctor of philosophy, University of Illinois at Urbana-Champaign.

Kumar, A. and Higdon, J. J. L. (2010). Origins of the anomalous stress behavior in charged colloidal suspensions under shear. *Physical Review E - Statistical, Nonlinear, and Soft Matter Physics*, 82(September):1–7.

Kutchko, B., Crandall, D., Gill, M., McIntyre, D., Spaulding, R., Strazisar, B., Rosenbaum, E., Haljasmaa, I., Benge, G., Cunningham, E., DeBruijn, G., and Gardner, C. (2013). Computed Tomography and Statistical Analysis of Bubble Size Distributions in Atmospheric-Generated Foamed Cement. Technical Report August.

Kutchko, B., Crandall, D., Moore, J., Gill, M., McIntyre, D., Rosenbaum, E., Haljasmaa, I., Strazisar, B., Spaulding, R., Harbert, W., Benge, G., Cunningham, E., Lawrence, D. W., DeBruijn, G., and Gardner, C. (2015). Field-Generated Foamed Cement : Initial Collection , Computed Tomography , and Analysis. Technical Report July, U.S. Department of Energy, National Energy Technology Laboratory.

Langevin, D. (2000). Influence of interfacial rheology on foam and emulsion properties. *Advances in colloid and interface science*, 88(1-2):209–222.

Lees, A. and Edwards, S. (1972). The computer study of transport processes under extreme conditions. *Journal of Physics C: Solid State Physics*, 5(15):1921.

Lipton, R. and Avellaneda, M. (1990). Darcy's law for slow viscous flow past a stationary array of bubbles. *Proceedings of the Royal Society of Edinburgh Section A: Mathematics*, 114(1-2):71–79.

Lipton, R. and Vernescu, B. (1994). Homogenisation of two-phase emulsions. *Proceedings of the Royal Society of Edinburgh Section A: Mathematics*, 124(6):1119–1134.

Loeffler, N. (1984). Foamed Cement: A Second Generation. In *Permian Basin Oil and Gas Recovery Conference*.

Marshall, J. and Dayal, K. (2014). Atomistic-to-continuum multiscale modeling with long-range electrostatic interactions in ionic solids. *Journal of the Mechanics and Physics of Solids*, 62:137–162.

Massoudi, M. (2002). On the importance of material frame-indifference and lift forces in multiphase flows. *Chemical Engineering Science*, 57(17):3687–3701.

Massoudi, M. (2003). Constitutive relations for the interaction force in multicomponent particulate flows. *International Journal of Non-Linear Mechanics*, 38(3):313–336.

Massoudi, M. (2008). A note on the meaning of mixture viscosity using the classical continuum theories of mixtures. *International Journal of Engineering Science*, 46(7):677–689.

Massoudi, M. (2010). A mixture theory formulation for hydraulic or pneumatic transport of solid particles. *International Journal of Engineering Science*, 48(11):1440–1461.

Massoudi, M. and Wang, P. (2013). Slag behavior in gasifiers. part ii: constitutive modeling of slag. *Energies*, 6(2):807–838.

Mathis, B. (2016). Foam Cement Bubble Characterization. Technical Report August, National Energy Technology Laboratory.

Maxey, M. R. and Riley, J. J. (1983). Equation of motion for a small rigid sphere in a nonuniform flow. *The Physics of Fluids*, 26(4):883–889.

Michaux, M., Nelson, E. B., and Vidick, B. (1990). 2. Chemistry and Characterization of Portland Cement. In Nelson, E. B., editor, *Well Cementing*, pages 2.1 – 2.17. Schlumberger Educational Services.

Nelson, E., Baret, J.-F., and Michaux, M. (1990). 3. Cement additives and mechanism of action. In Nelson, E. B., editor, *Well Cementing*, pages 3.1 – 3.37. Schlumberger Educational Services.

Nelson, E. B. (1990). *Well cementing*, volume 28. Newnes.

NETL (2019). Tbd. Internal Research to be published.

Ollion, J., Cochennec, J., Loll, F., Escudé, C., and Boudier, T. (2013). Tango: a generic tool for high-throughput 3d image analysis for studying nuclear organization. *Bioinformatics*, 29(14):1840–1841.

Olowolagba, K. O., Brenneis, C., et al. (2010). Techniques for the study of foamed cement rheology. In *SPE Production and Operations Conference and Exhibition*. Society of Petroleum Engineers.

O'Rourke, T. J. N. S. C. and Crombie, D. N. S. C. (1999). A Unique Solution to Zonal Isolation Utilizing Foam-Cement and Coiled-Tubing Technologies. *Society of Petroleum Engineers*, (SPE 54473).

Phansalkar, N., More, S., Sabale, A., and Joshi, M. (2011). Adaptive local thresholding for detection of nuclei in diversity stained cytology images. In *2011 International Conference on Communications and Signal Processing*, pages 218–220. IEEE.

Plimpton, S. (1995). Fast Parallel Algorithms for Short Range Molecular Dynamics. *Journal of Computational Physics*, 117(June 1994):1–19.

Pugh, R. J. (1996). Foaming, foam films, antifoaming and defoaming. *Advances in Colloid and Interface Science*, 64(95):67–142.

Pugh, R. J. (2005). Experimental techniques for studying the structure of foams and froths. *Advances in colloid and interface science*, 114-115:239–251.

Rae, P. (1990). Cement Job Design. In Nelson, E. B., editor, *Well Cementing*, chapter 11, pages 11.1 – 11.17. Schlumberger Educational Services, Sugar Land, Texas.

Rahimian, A., Veerapaneni, S. K., Zorin, D., and Biros, G. (2015). Boundary integral method for the flow of vesicles with viscosity contrast in three dimensions. *Journal of Computational Physics*, 298:766–786.

Rajagopal, K. R. and Tao, L. (1995). *Mechanics of mixtures*, volume 35. World scientific.

Rognon, P. G., Einav, I., and Gay, C. (2010). Internal relaxation time in immersed particulate materials. *Physical Review E - Statistical, Nonlinear, and Soft Matter Physics*, 81(6):1–9.

Rognon, P. G., Einav, I., and Gay, C. (2011). Flowing resistance and dilatancy of dense suspensions: lubrication and repulsion. *Journal of Fluid Mechanics*, 689:75–96.

Rognon, P. G. and Gay, C. (2008). Soft Dynamics simulation. 1. Normal approach of two deformable particles in a viscous fluid and optimal-approach strategy. *European Physical Journal E*, 27:253–260.

Rognon, P. G. and Gay, C. (2009). Soft dynamics simulation. 2. Elastic spheres undergoing a T 1 process in a viscous fluid. *European Physical Journal E*, 30:291–301.

Rosenbaum, E., Massoudi, M., and Dayal, K. (2019). Effects of polydispersity on structuring and rheology in flowing suspensions. *Journal of Applied Mechanics*.

Roussel, N. (2005). Steady and transient flow behaviour of fresh cement pastes. *Cement and Concrete Research*, 35:1656–1664.

Sadhal, S., Ayyaswamy, P., and Chung, J. (1997). Transport phenomena with bubbles and drops.

Sangani, A. and Acrivos, A. (1983). The effective conductivity of a periodic array of spheres. *Proc. R. Soc. Lond. A*, 386(1791):263–275.

Schindelin, J., Arganda-Carreras, I., Frise, E., Kaynig, V., Longair, M., Pietzsch, T., Preibisch, S., Rueden, C., Saalfeld, S., Schmid, B., et al. (2012). Fiji: an open-source platform for biological-image analysis. *Nature methods*, 9(7):676.

Song, C., Wang, P., and Makse, H. A. (2008). A phase diagram for jammed matter. *Nature*, 453(7195):629.

Soo, S.-l. (1967). Fluid dynamics of multiphase systems. *WALTHAM, MASS, BLAISDELL PUBLISHING CO, 1967. 524 P, 206 FIG, 8 TAB, 886 REF.*

Stukowski, A. (2010). Visualization and analysis of atomistic simulation data with OVITOthe Open Visualization Tool. *Modelling and Simulation in Materials Science and Engineering*, 18(1):15012.

Tabakova, S. S. and Danov, K. D. (2009). Effect of disjoining pressure on the drainage and relaxation dynamics of liquid films with mobile interfaces. *Journal of Colloid and Interface Science*, 336(1):273–284.

Tadmor, E. B. and Miller, R. E. (2011). *Modeling materials: continuum, atomistic and multiscale techniques*. Cambridge University Press.

Tan, L., Ye, G., Schlangen, E., and Van Breugel, K. (2007a). Coupling of hydration and fracture models: Failure mechanisms in hydrating cement particle systems. *Particle and Continuum Aspects of Mesomechanics*, pages 563–571.

Tan, L. K., Schlangen, E., and Ye, G. (2007b). Simulation of failure in hydrating cement particles systems. 348:737–740.

Taylor, G. I. (1932). The viscosity of a fluid containing small drops of another fluid. *Proceedings of the Royal Society of London. Series A, Containing Papers of a Mathematical and Physical Character*, 138(834):41–48.

Tchen, C. (1947). Mean value and correlation problems connected with the motion of small particles suspended in a turbulent fluid.

Truesdell, C. (1984). Rational thermodynamics.

Wallis, G. B. (1969). One-dimensional two-phase flow.

Walton, i. O. and Braun, R. (1986). Stress calculations for assemblies of inelastic speres in uniform shear. *Acta mechanica*, 63(1-4):73–86.

White, J., Moore, S., Miller, M., Faul, R., and Services, H. E. (2000). IADC / SPE 59136 Foaming Cement as a Deterrent to Compaction Damage in Deepwater Production. *2000 IADC/SPE Drilling Conference*.

Wu, W.-T., Aubry, N., Antaki, J. F., McKoy, M. L., and Massoudi, M. (2017). Heat transfer in a drilling fluid with geothermal applications. *Energies*, 10(9):1349.

Xiao, Y. (2005). *The influence of oxygen vacancies on domain patterns in ferroelectric perovskites*. PhD thesis, California Institute of Technology.